Development of Local Models and their Computational Implementation for Polymer Coated Steel Sheets

J. Rojek
M. Luege
E. Oñate

Publication CIMNE Nº-265, October 2004

Development of Local Models and their Computational Implementation for Polymer Coated Steel Sheets

J. Rojek
M. Luege
E. Oñate

Publication CIMNE Nº-265, October 2004

International Center for Numerical Methods in Engineering
Gran Capitán s/n, 08034 Barcelona, Spain

Contents

Chapter 1

Introduction

This report presents review of the state of the art of numerical modelling of polymers and polymer coated metal laminates and gives details of selected numerical models including those that will be used in the work in the project POLYCOAT. The first sections of the report contain characteristics of polymers which are important for the application studied in the project. Basic mechanical and thermal properties of the polymers are reviewed. Then constitutive models developed for polymers are reviewed based on literature and own work. Details of selected models are given. Deformation behaviour of polymer coated metal laminates is considered with special attention to the phenomena observed at the polymer–metal interface. The numerical models for the interface are presented finally.

Chapter 2

Basic information about polymers

Polymers are material characterized with a structure created by large molecules with long chains formed by the combination of many repeated structural units derived from the polymerizing of a small molecule which is called the monomer.

Polymers can be classified based on:

- origin,
- polymerization reactions,
- polymer topology,
- thermophysical properties.

Based on the origin polymers can be classified into the following groups:

- natural polymers (proteins, polysaccharides),
- synthetic polymers.

There are two fundamental polymerization reactions:

- chain polymerization,
- step polymerization.

Based on the topology polymers can be classified into the following groups (Fig. 2.1):

- linear,
- nonlinear (branched),
- network.

Figure 2.1: Topology of polymers: a) linear, b) nonlinear (branched), c) network

Based on thermophysical properties polymers can be classified into the following groups:

- thermosets — each monomer has three or more links to other units, become infusible and insoluble upon heating, and do not return to their original chemical state upon cooling;
- thermoplastics — each monomer only links to two others to forms chains, soften and flow upon heating and return to original state upon cooling;
- elastomers.

Based on the morphology thermoplastic polymers can be divided into

- amorphous or glassy (natural rubber, polycarbonate, acrylonitrile-butadiene-styrene, polystyrene),
- semi-crystalline solids (polyamide, polyethylene tereplithalate – PET, nylon)
- crystalline solids (linear polyethylene, polypropylene).

Glassy polymers solely consist of an amorphous phase. Semi-crystalline polymers contain an amorphous and a crystalline phase interacting with one another during deformation. The crystalline polymers are characterized with higher tensile strength, higher flexural modulus, hardness and creep resistance. Amorphous polymers have higher impact resistance and less shrinkage.

Chapter 3

Mechanical properties of polymers

3.1 Summary of basic mechanical parameters

Basic mechanical behaviour of polymeric materials can be defined by the following set of properties:

- stress-strain curves
- elastic properties (Young modulus, shear and bulk moduli, Poisson's ratio)
- plastic properties (yield stress, softening/hardening, toughness, tensile strength, maximum elongation, hydrostatic pressure dependency)
- strain rate dependency (viscosity, creep and relaxation parameters)
- temperature dependency

[1, 2, 3]

3.2 Deformation behaviour

Deformation behaviour is usually characterized by the stress-strain curves obtained in short-term mechanical tests (e.g. tension, compression, bending) in which the response (strain) of a sample subjected to a loading that increases with time, at constant rate, is measured. The deformation behaviour of polymer materials vary greatly. Figure 3.1 illustrates a great variation of deformation behaviour of polymers. Figure 3.1a shows the stress-strain curves for hard, brittle materials, the curve in Fig. 3.1b represents a ductile polymer and the curves in Fig. 3.1c are characteristic of elastomers.

The brittle behaviour shown in Fig. 3.1a is characteristic of amorphous polymers at temperatures well below the glass transition temperatures. These materials fail

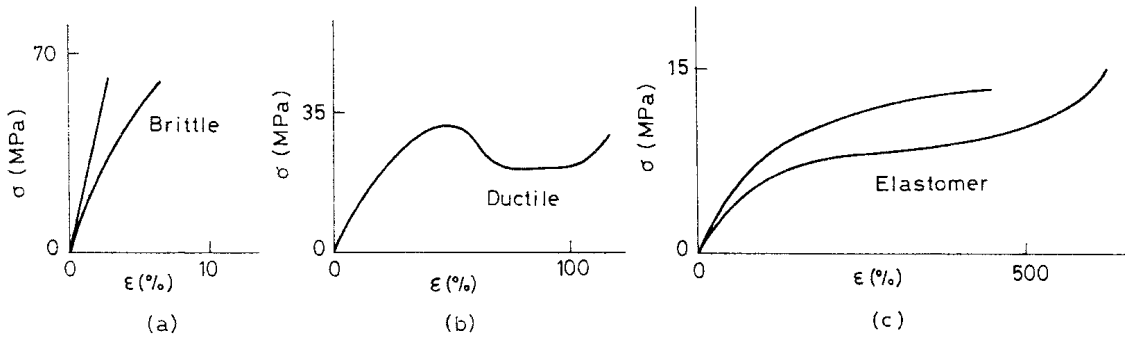

Figure 3.1: Typical stress–strains curves for polymers (according [1])

at low strains with brittle fracture. Semicrystalline polymers and thermoset resins in temperatures much lower than the glass transition temperatures also exhibit the pattern shown in Fig. 3.1a.

Ductile polymer materials represented by the curve in Fig. 3.1b undergo yielding before failure. The most ductile polymers undergo necking and cold drawing. Semicrystalline polymers at temperatures intermediate between melting and glass transition and glass transition (e.g., polyethylene at room temperature) are typical examples that display this behaviour. Although very ductile plastics, like polyethylene, can reach strains up to 250%, some fail immediately after yielding.

Stress–strain curves for different polymer materials obtained in short-term tensile tests are shown in Fig. 3.2 together with tensile curves for steel and copper. It can be seen that although polymers have much lower tensile strength, they exhibit much higher strains at break. The shape of the stress-strain curves for a given polymer material can be different depending on temperature, strain-rate and hydrostatic pressure. Dependence of polymer deformation on strain rate (viscosity), pressure and temperature will be considered in the following sections.

In polymer materials it is difficult to distinguish between elastic (recoverable) and plastic (nonrecoverable) deformation, since degree to which sample recovers its original dimensions depends on temperature and time. High molecular mass thermoplastics can return to their original dimensions from high strains if they are heated after the load is removed.

The most important mechanisms that can lead to plastic deformation in polymers are shear yielding and crazing.

3.3 Shear yield

During plastic deformation in polymers, zones of localised deformation are often observed in the form of necking or shear bands. For polymers localisation usually spreads

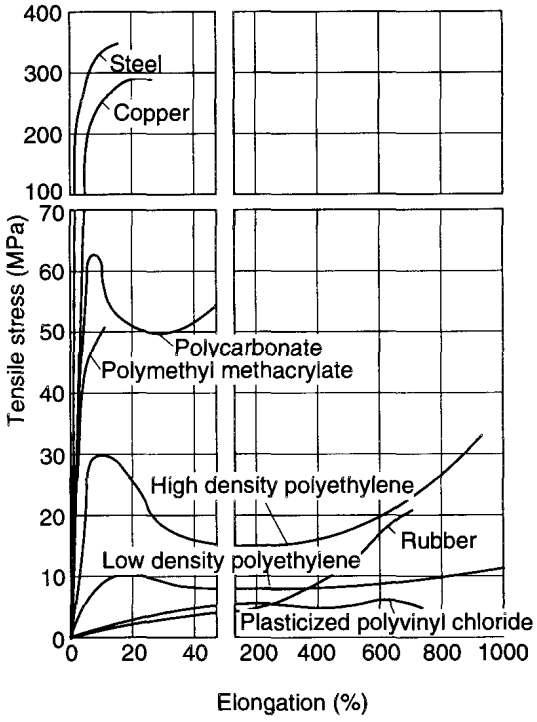

Figure 3.2: Tensile stress–strains curves for several polymer materials and metals (according [4])

out over the specimen, caused by a specific molecular structure. This is called the continuous mode of plastic deformation. It is often referred to as shearing or shear yielding in the literature. Shear yielding takes place at constant volume and leads to a large change in specimen shape.

Shear yielding is involved in a ductile failure of polymers. A typical stress–strain curve for a ductile polymer is shown in Fig. 3.3. The first phase (0-A) represents a linear response. At point A the curve changes slope until it reaches a maximum point, called the yield point which corresponds to the yield initiation. After yielding the softening follows until the point B. In the region BC the material is strained without any apparent change of the stress, giving rise to the phenomenon called cold drawing. At increasing strains from point C strain hardening occurs. Finally fracture of the material occurs at point F.

The changes observed in the stress-strain curve are related to the change of shape of the specimen. In the first region, in the linear range, the deformation occurs uniformly, which is shown in Fig. 3.3a. When the yield point is reached the neck shown in Fig. 3.3b is formed. Once the neck forms, it extends along the sample at a fairly constant stress. This process is called the cold drawing and is shown schematically in Fig. 3.3c. The hardening observed at large strain occurs when the polymer chains are oriented

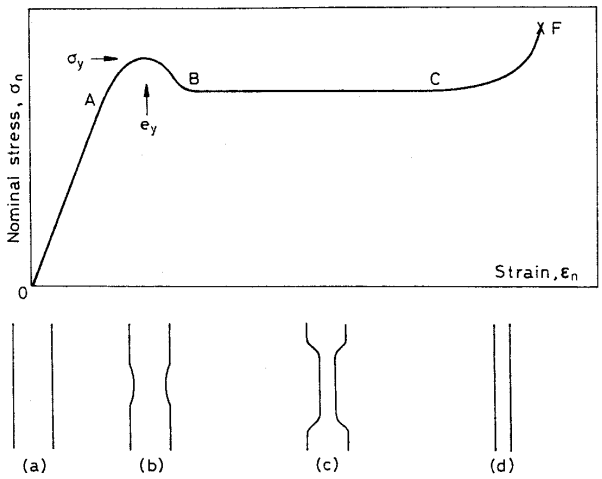

Figure 3.3: Typical stress-strain curve for a ductile polymer (according [1])

along the load direction (Fig. 3.3d). The neck propagates through the length of the specimen until it reaches the fracture point F.

When a glassy (amorphous) polymer undergoes shear yielding, the local shear strains provoke the displacement of the polymer chains to new equilibrium positions, which are stable in the absence of stresses. Above the glass transition temperature amorphous polymers behave approximately as rubbers, without undergoing shear yielding.

Semicrystalline polymers must be considered as two-phase mixtures of amorphous regions between lamellar crystals. The yield stress increases with increasing crystallinity when the deformation occurs at temperature above the glass transition temperature of the amorphous phase and below, but close to, the melting temperature of the crystalline phase.

3.4 Crazing

The discontinuous mode of irreversible deformation is crazing. Crazing is a characteristic of thermoplastic polymers in case of brittle fracture. Crazes are the result of localised yield. Crazes are formed in the plane perpendicular to the maximum principal stress. Crazes appear in the form of adjacent cavities separated by ligaments.

Figure 3.4 [2] explains schematically initiation and development of crazes. When the load is applied small voids existing in weak regions of polymer material nucleate crazes that lead to yielding or failure.

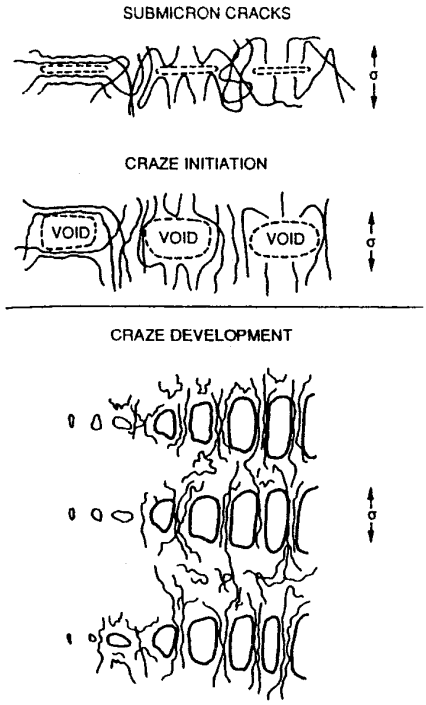

Figure 3.4: Craze initiation and development (according [2])

3.5 Time dependence of polymer properties

Time dependent (viscous) properties are characteristic of long-chain structures. Marked time dependence is found in thermoplastics. Heavily cross-linked polymers show little time dependence at ambient temperatures.

Time dependent mechanical properties may become apparent in various ways, cf. [5, 1]:

- strain rate dependency of short-time load load response – increase of stiffness and strength under impact loading,
- creep and stress relaxation in long term response,
- phase difference between stress and strain in high-frequency dynamic loading.

3.5.1 Strain rate dependency in short term polymer response

Viscous effects are observed clearly in the short term mechanical response of an amorphous polymer material. Constant deformation rate loading tests are frequently used to evaluate the effect of strain rate sensitivity. Figure 3.5 shows tensile stress-strain curves for polystyrene at different strain rates, cf. [5]. A typical strain rate sensitivity

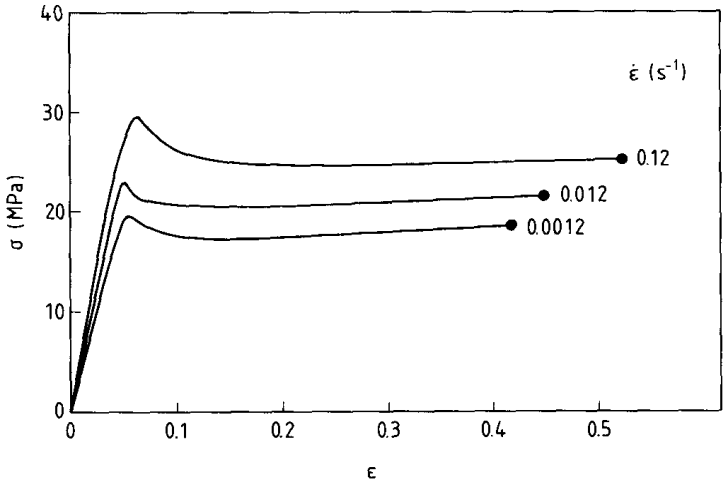

Figure 3.5: Effect of strain rate on stress–strain characteristics of injection moulded HIPS (according [5])

is illustrated. Stresses increase with an increase of strain rate. Viscous effects appear in the elastic (increase of stiffness) as well as in the plastic range (increase of strength). The tendency of brittleness increase with the strain rate increase is also observed.

3.5.2 Creep and stress relaxation

Creep and relaxation phenomena are another effect of viscoelasticity especially important in in long-term polymer response. Creep is a time-dependent strain increase to a constant applied stress.

Figure 3.6 [5] shows response of an elastic and a viscoelastic body to a step constant loading shown at top of the figure that illustrates the creep behaviour of the viscoelastic body. In the response of the viscoelastic body it is convenient to split the deformation into elastic strain, delayed elastic strain and viscous flow, ε_1, ε_2 and ε_3, respectively.

Stress relaxation is a time-dependent stress decay under constant strain conditions. Figure 3.7 [5] shows response of an elastic and a viscoelastic body to a step deformation shown at top of the figure. Response of the viscoelastic body shows the stress relaxation phenomenon. In the response of the viscoelastic body it is convenient to split the stress into the elastic and viscous components, σ_1 and σ_2, respectively.

The creep and stress relaxation polymer behaviour depends heavily on the material temperature, having the highest rates of deformation around the glass transition (see Sec. 3.6.1) [4]. Many plastics materials, however, creep readily at ambient or moderate temperatures.

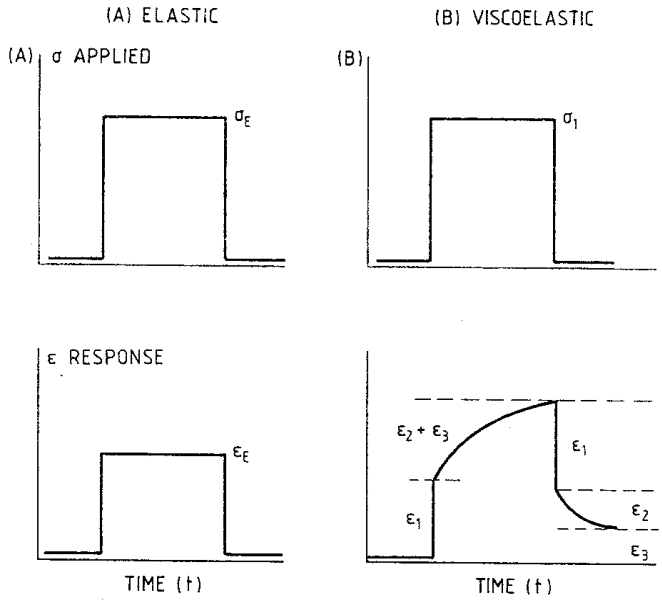

Figure 3.6: Creep loading programmes a) for elastic material, b) for viscoelastic material (according [5])

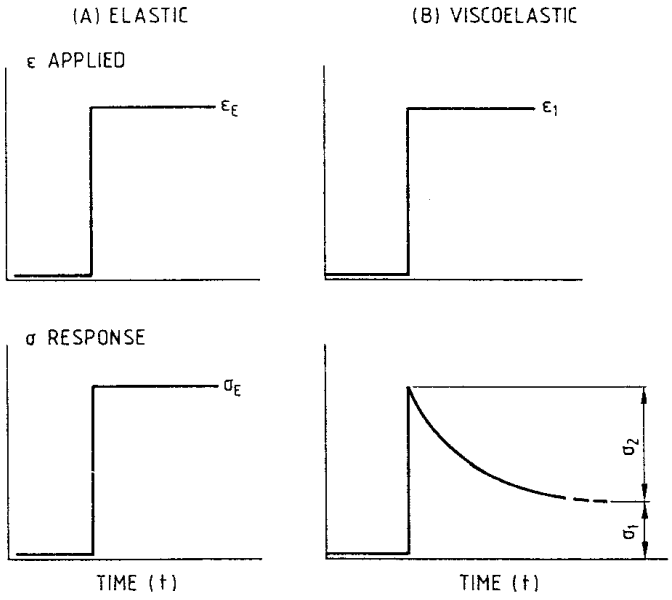

Figure 3.7: Stress relaxation loading programmes a) for elastic material, b) for viscoelastic material (according [5])

3.6 Temperature dependency of polymer properties

Polymer mechanical properties are affected by the temperature changes, cf. [5]. Changes of greater magnitude are observed if deformation characteristics are considered in the temperature range including thermal transitions.

3.6.1 Glass transition temperature

Figure 3.8 shows a typical temperature dependence of the deformation resistance (characterized with selected modulus). At very low temperatures the polymer response to loading is solid-like with high modulus. At low temperatures there maybe so-called secondary transitions (γ- and β-transitions) involving small changes of the polymer deformation resistance. At increasing temperatures there is one major transition (α-transition) called the glass transition accompanied by large decrease of the resistance. Immediately above the glass transition temperature T_g the polymer properties change to those of a rubbery material. Depending on the molecular weight, the

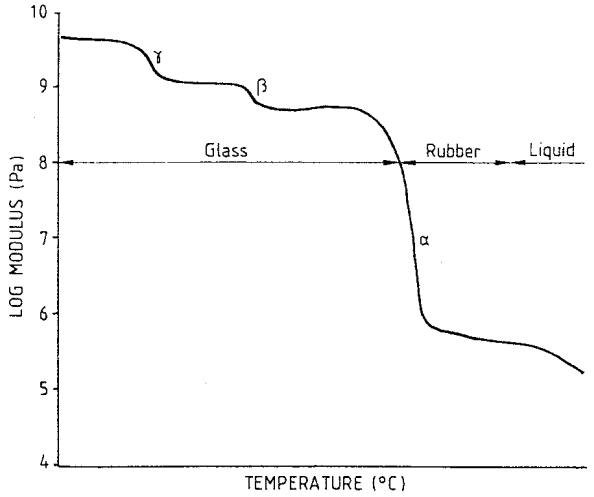

Figure 3.8: Generalized relationship between modulus (deformation resistance) and temperature for amorphous polymers (according [5])

rubber-like behaviour may persist for a certain temperature interval above the glass-transition temperature, called the rubber plateau. At further increase of temperature at melting temperature T_m linear and branched polymers change from solid to liquid (crosslinked/network polymers have only glass transition).

Glass transition temperature T_g and melting temperature T_m are important data characterizing polymers. Table 3.1 gives transition temperatures for typical polymers.

Table 3.1: Typical transition temperatures

Polymer	T_m, °C	T_g, °C	Solubility parameter δ_s*
Poly(dimethyl siloxane)	−54	−123	7.3
Polyethylene	137	−120(?)	7.9
Polyisobutylene	–	−70, −60	8.1
cis-Polyisoprene	28	−70	8.3
Polychloroprene	80	−50	9.2
Poly(vinyl acetate)	–	29	9.4
Poly(vinyl chloride)	212	87	9.7
Poly(methyl methacrylate)	–	105	9.5
Polystyrene	240 (isotactic)	100, 105	9.1
Poly(vinyl methyl ether)	144	−20, −10	
Poly(vinyl ethyl ether)	86	−25	
Poly(vinyl *n*-butyl ether)	64	−52	
Poly(vinyl isobutyl ether)	115	−5, −18	
Poly(vinyl *tert*-butyl ether)	260	−8	
Poly(ethylene terephthalate)	267	69	10.7
Cellulose tributyrate	183	120	
Ethyl cellulose	–	43	10.3

*Solubility parameter in $(cal/cm^3)^{1/2}$ taken from Table 2-5.

The glass transition temperature T_g is a decisive factor whether an amorphous polymer is a thermoplastic or an elastomer. A general rule of thumb is that an amorphous polymer with the glass transition temperature T_g below the room temperature is an an elastomer and an amorphous polymer with the glass transition temperature T_g above the room temperature is an a thermoplastic.

The glass transition temperature is also highly influential in semi-crystalline polymers, cf. Fig. 3.9, where a brittle-tough (brittle-ductile) transition in solid phase is often observed. The rate of change of modulus-temeprature characteristics across the glass transition depends on the degree of crystallinity. Figure 3.9 shows that the deformation resistance of a semi-crystalline polymer decreases dramatically on traversing the melting temperature T_m.

The mechanical properties of polymers can be modified by relaxation transitions occurring over extended periods of time (physical ageing) during service life.

Traversing the glass transition temperature influences other polymer properties, as well, cf. [6]. Time-dependent moduli characterizing creep and stress relaxation as well as some thermal properties change significantly within the glass transition.

3.6.2 Effect of temperature on stress–strain relationships

Temperature determines not only dynamic, short term or low-strain moduli, but also feasibility of plastics components undergoing yield, hardening or rubber-like deformation. Figure 3.10 [5] shows generalised stress–strain relationships for different temperatures. The curves A–E corresponding to increasing temperatures can characterize the same polymer. Curve A for the lowest temperature represents a brittle viscoelas-

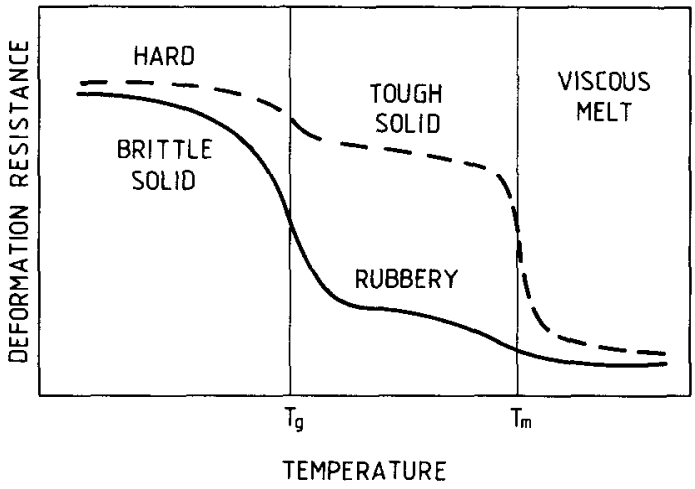

Figure 3.9: Generalized relationship between deformation resistance and temperature for amorphous (solid line) and semi-crystalline (dashed line) polymers (according [5])

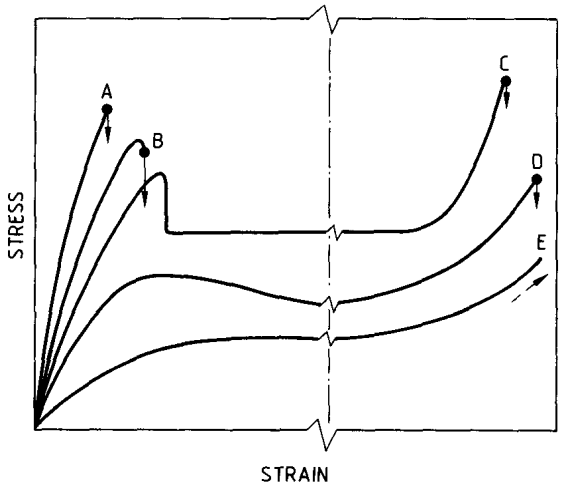

Figure 3.10: Effect of temperature on stress–strain relationships (according [5])

tic response with failure occuring at maximum load and relatively low strain. Curve B shows a distinct yield point with subsequent failure by neck instability. Curve C exhibit yielding (with a characteristic load drop), stable neck growth through cold drawing and orientation hardening and eventual failure at very high strain levels often exceeding 300%. Curves D and E are characteristics of a sigmoidal rubber-elastic response, typical of a amorphous or low cristallinity materials at temperatures just above the glass transition temperature. These materials are characterised by a low drawing process and are highly extensible. Deformation may be predominantly elastic, unless stress-induced crystallisation occurs during the drawing process.

3.6.3 Brittle–ductile transition

In the previous section a change of a polymer behaviour from brittle to ductile with an increase of temperature has been discussed. At low temperature the fracture is brittle, whereas at high temperatures the polymer shows yield and ductile failure. The deformation of a thermoplastic is considered to be a competition between crazing and shear yielding. If crazing dominates, the behaviour of the polymer is brittle. If shear yielding occurs, the polymer is ductile [1]. The brittle–ductile transition can be explained by considering that brittle fracture and and yield are independent processes that differ in their dependence on temperature [7], as it is illustrated schematically in Fig. 3.11. Both the brittle strength σ_B and the yield stress σ_y decrease with increasing

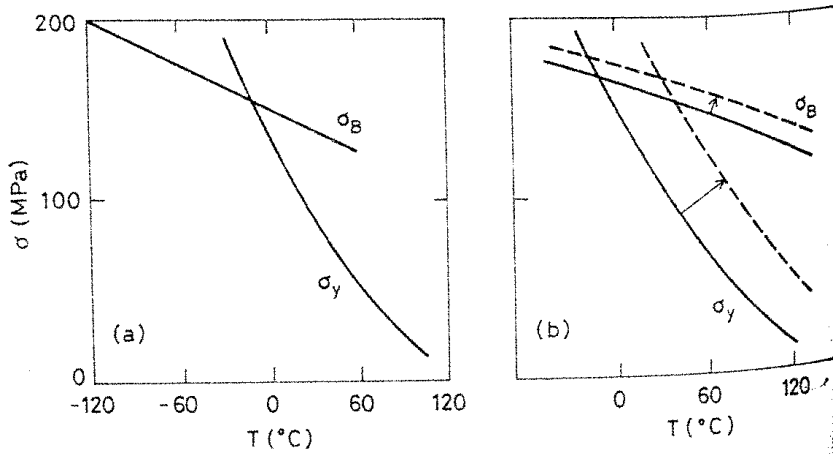

Figure 3.11: Brittle–ductile transition (according [7]); a) variation of the brittle strength σ_B and the yield stress σ_y with temperature; b) effect of strain rate on T_B, solid line – low strain rate, dashed line – high strain rate.

temperature. There is a critical value of temperature, T_B, at which $\sigma_B = \sigma_y$. At temperature below T_B, the yield stress exceeds the brittle fracture strength and the process that takes place is the one requiring the lowest stress, i.e. brittle fracture. At $T > T_B$ the situation is reversed and $\sigma_y < \sigma_B$, leading to yield and ductile failure. The temperature T_B is called the brittle–ductile transition temperature.

On the other hand it is expected that the strain rate also influences T_B. It has been found out that while brittle fracture is hardly affected, the yield stress changes significantly with the strain rate, cf. Sec. 3.5.1. As a result as it is shown in Fig. 3.11b the brittle–ductile transition temperature increases as the strain rate increases.

Although attempts have been made to relate T_B to molecular relaxation processes, in particular to the glass transition, T_g, no general relationship has been established yet [1]. In some polymers, such as natural rubber and polystyrene, T_B coincides with T_g, but other polymers present ductile behaviour at $T < T_g$. The addition of plasticizers

reduces σ_y and therefore also decreases σ_B. T_B increases as the cross-linking and crystallinity of the polymer increase. The fracture behaviour of semicrystalline polymers presents some differences with respect to that of amorphous polymers. Semicrystalline polymers can exhibit different morphologies, like oriented fibres or spherulites produced in isotropically crystallized polymers. Oriented polymers have high stiffness and strength, while isotropic crystallized polymers are tough and flexible, especially at $T > T_g$ [1].

3.7 Pressure dependence of yield behaviour

Yield behaviour of polymers under tension and compression may be different. In general for polymers the compressive yield stress is higher than the tensile yield stress, cf. [1]. It can be seen in Fig. 3.12 [1] which shows stress–strain curves for polycarbonate determined under uniaxial tension and compression. The behaviour of the material given in Fig. 3.12 under tension and compression is different as far as possibility to deform at large strains is considered, the material tested under tension fractures immediately after reaching yield while can substain large deformation under compression.

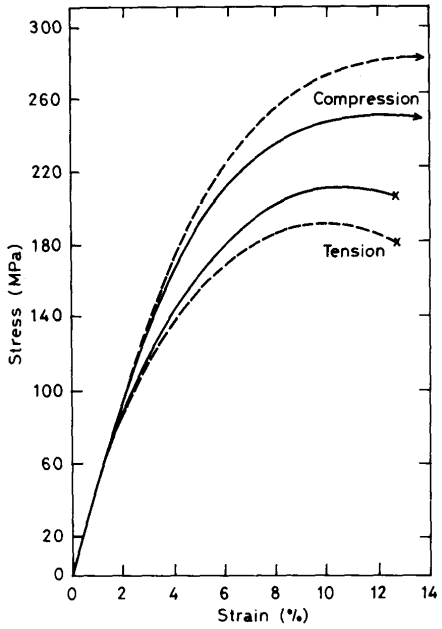

Figure 3.12: Stress–strain curves for polycarbonate for uniaxial tension and compression, dashed line: nominal stress curve, solid lines: true stress curve (according [1])

The difference in yield stress for pressure and compression is a manifestation of pressure dependency of yield behaviour of polymers. Yield stress of polymers increases

with hydrostatic pressure(absolute value of pressure). Figure 3.13 from [2] presents

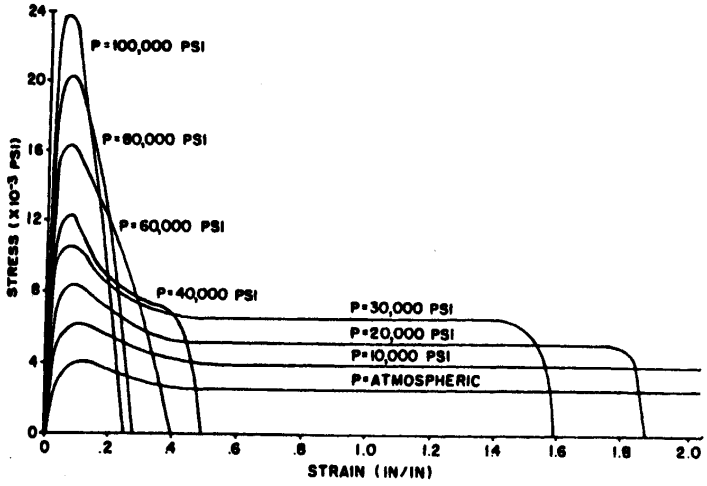

Figure 3.13: Stress–strain curves of polypropylene at various pressures (according [2])

data for polypropylene which exhibits typical effect of hydrostatic pressure.

The influence of pressure on mechanical properties can be explained by the fact that the phenomena are associated with a free volume in the polymer. Increase of pressure results in decrease of free volume (or increase of the density of packing) – the effect is similar to a temperature decrease.

Chapter 4

Thermal properties of polymers

4.1 Introduction

The process of heat conduction through the polymer material depends on its thermal properties such as specific heat, thermal conductivity, thermal diffusivity, heat transfer coefficients and thermal expansion (or contraction). Thermal properties of polymers are also strongly temperature dependent with the glass transition and melting temperatures being important points on the temperature scale.

4.2 Specific heat

The specific heat is the heat energy required to raise the temperature of a unit mass by one degree. It can be measured at either constant pressure or constant volume. The volume changes of a polymer have negligible effect so it can assumed for practical purpose that specific heat at constant volume or at constant pressure are the same.

Specific heat of polymers changes little in the range of practical processing or design tempeartures, cf. [4]. Figure 4.1 [4] shows specific heat vs. temperature curves for three categories of polymers. The specific heat capacity of amorphous thermoplastics changes slightly at temperatures close to the glass transition temperature, T_{g}. Semi-crystalline thermoplastics show big changes in the value of specific heat at the melting point of the crystallites. This jump in specific heat includes the heat require to melt the crystallites, called the heat of fusion.

the chemical reaction that takes place during solidification of thermosets also leads to considerable thermal effects. In a hardened state, their thermal data are similar to those of amorphous thermoplastics.

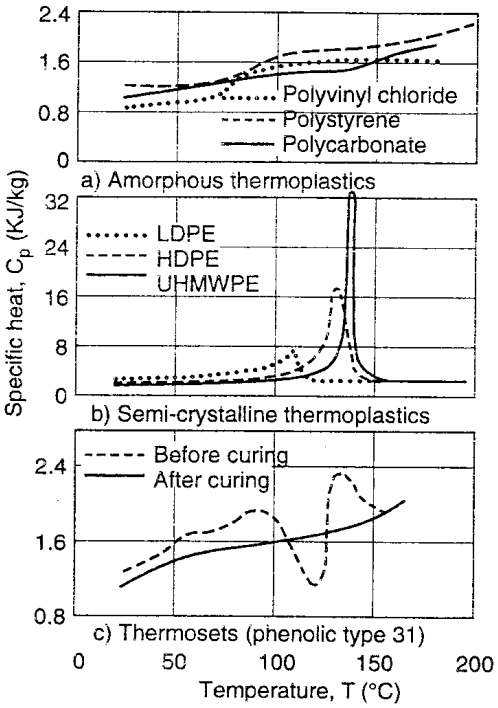

Figure 4.1: Specific heat vs. temperature curves for three categories of polymers (according to [4])

4.3 Thermal conductivity

Polymers are usually bad thermal conductors. Amorphous polymers show an increase in thermal conductivity with increasing temperature, up to the glass transition temperature. Above the glass transition temperature the thermal conductivity decreases with increasing temperature, cf. [4]. Figure 4.2 [4] shows the thermal conductivity as a function of temperature (below the glass transition temperature) for various amorphous thermoplastics.

Crystalline polymers have higher thermal conductivity than amorphous plastics. The dependence of thermal conductivity on crystallinity leads to change of conductivity in the melting region (Fig. 4.3).

Another factor influencing the conductivity is orientation, which can lead to anisotropic thermal conductivity. The effect of pressure on the thermal conductivity in the solid state is negligibly small, cf. [5], it is significant for melts, cf. [4].

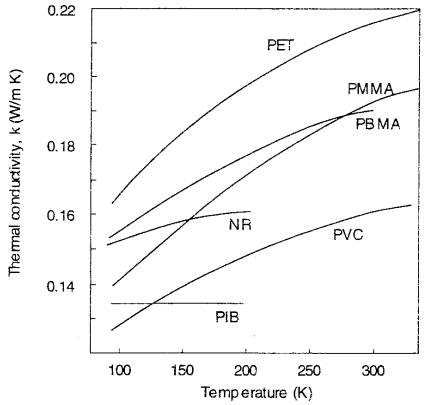

Figure 4.2: Thermal conductivity as a function of temperature for various amorphous thermoplastics, according to [4]).

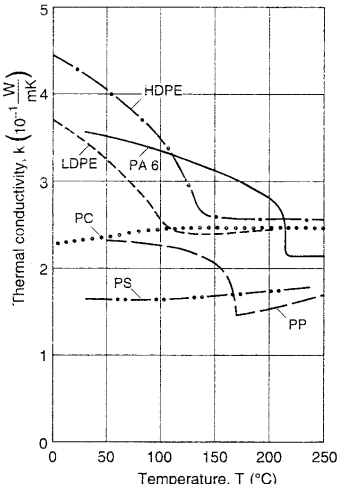

Figure 4.3: Thermal conductivity as a function of temperature for various thermoplastics, according to [4]).

4.4 Thermal expansion and contraction

With an increase of temperature material usually expands, and so do polymers. Orientation of the crystalline polymers results in anisotropic expansion (or contraction). Then the coefficients of linear expansion are usually given for the plane of orientation and perpendicular to it. Sometimes despite inaccuracies anisotropic expansion and contraction is assumed.

Expansion and contraction are similar to conductivity in the dependence on crystallinity, the higher crystallinity the lower expansion. Similarly expansion and contraction are sensitive to temperature. This is illustrated in Fig. 4.4.

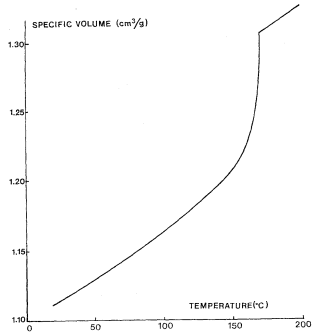

Figure 4.4: Specific volume as a function of temperature for a semi-crystalline polymer, according to [5]).

Chapter 5

Properties of polyethylene terephtalate (PET)

5.1 Introduction

Poly-Ethylene Terephtalate (PET) is a thermoplastic polyester copolymer. Because of its mechanical, optical, thermal and chemical properties is used in various packaging application. PET is a semi-crystalline polymer. Mechanical behaviour of the polymer depends on its microstructure. The PET microstructure varies depending on the thermal processing. In the forming process the microstructure depends on the process conditions – temperature and stress and strain conditions.

5.2 Microstructure

Semi-crystalline polymer have a hierarchical microstructure. Three relevant length scales can be identified: molecular, lamellar and spherulitic, cf. [8]. In a semi-crystalline polymer two different phases, the amorphous and crystalline phases coexist, with the crystalline phase confined to stacked layers separated by amorphous regions, the so-called lamellae. The mean thickness of these crystalline layers L_c is called the crystal thickness and the mean thickness of a crystalline and amorphous layers together L_{c+a} is called lamellar thickness or long period.

During polymer crystallisation a part of random coil in the supercooled melt, or superheated glass, that attaches to a crystal has to straighten out. Due to a large entropic barrier associated with this process, thermodynamic equilibrium is never reached, and L_c reflects the kinetics of the growth process. The size with the highest growth rate at a certain T_c will prevail, cf. [9]. The growth of such lamellae is initiated at various sites and proceeds radially, forming spherulites. The spherulites grow until they impinge, forming more or less well-defined polygonal boundaries. The overall rate of

crystallisation is determined by the nucleation rate and the crystall growth rate, cf. [9].

5.3 Crystallisation

PET has a glass transition temperature (T_g) of 70°C and a melting temperature (T_m) of 270°C. Thus at room temperature, the amorphous part of semi-crystalline is a glass.

For PET the crystallisation rate is zero at T_g and T_m and reaches the maximum value at $T_{max} \approx 270$°C [10]. PET crystallise slowly and it can be quenched from the melt to a glassy state. It is therefore possible to start crystallisation (glass-crystallisation) from the glass or from the melt (melt-crystallisation). Structures obtained by glass- and melt-crystallisation may be quite different. Melt crystallisation leads to larger spherulites when compared to glass crystallisation. At the lamellar scale, crystals in the melt-crystallised samples are larger and more perfectly formed (Fig. 5.1 [8]).

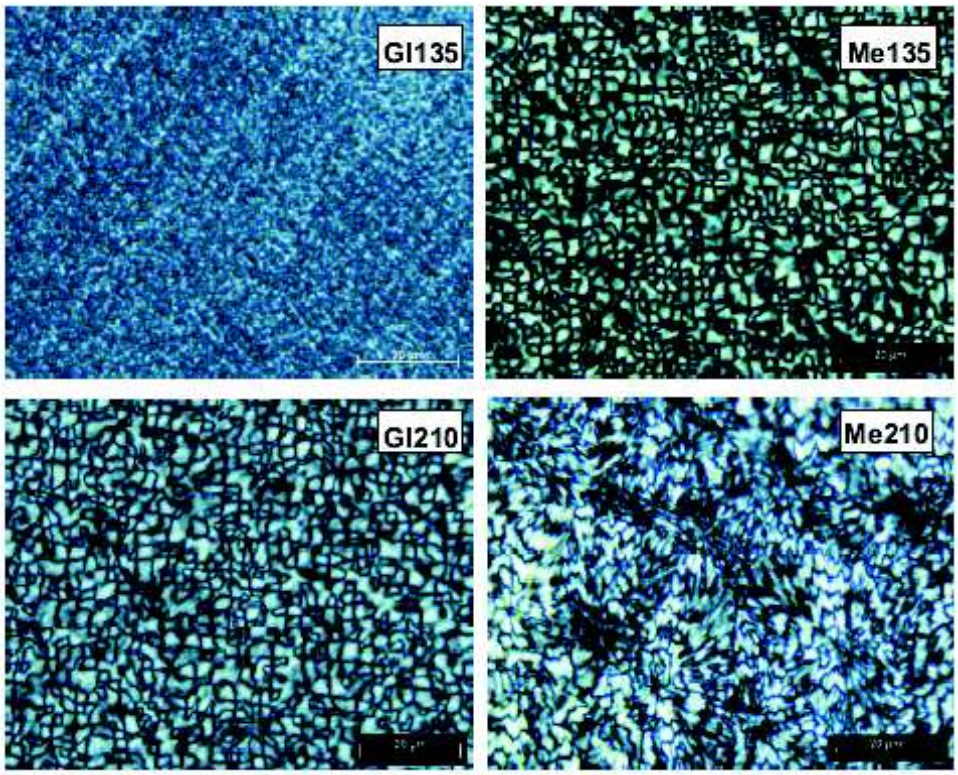

Figure 5.1: Microstructure of melt-crystallised (Me) and glass-crystallised (Gl) PET samples at temperatures 135°C and 210°C, according to [8].

5.4 Mechanical properties

The relation between structure and mechanical behaviour of a semi-crystalline polymer has usually been explained using "two-phase" model distinguishing a high-density crystalline phase and a low-density amorphous phase. The elastic moduli of the material are then related to the volume fraction of the crystalline phase. However the relationship between the crystalline fraction and large strain material parameters such as yield stress and strain hardening modulus is not so straightforward.

Mechanical properties of PET depend on the thermal treatment. Results of compression tests for PET specimens processed at different temperature conditions can be found in [8]. Figure 5.2 [8] shows a temperature treatment given to the PET samples when crystallising from glass or melt at a particular temperature T_c. These samples where then used in uniaxial compression tests. Stress–strain relationships obtained in these tests are shown in Figures 5.3 and 5.4 for the glass- and melt-crystallised PET samples, respectively. Amorphous PET initially shows an elastic response which is followed by yield which marks the onset of plastic deformation. Subsequently strain softening occurs followed by the strain hardening.

In glass-crystallised PET (Fig. 5.3) similar values for the strain hardening modulus and yield stress are found for T_c up to 120°C. Between T_c = 120°C and 135°C, the yield stress shows a large increase, which is accompanied by a simultaneous decrease in strain hardening modulus, and a decrease in strain softening.

The melt-crystallised samples (Fig. 5.4) with low crystallinity, show a low yield stress, a pronounced strain softening, and high strain-hardening modulus. The samples crystallized between 120°C to 210°C show an appreciably higher yield stress, by

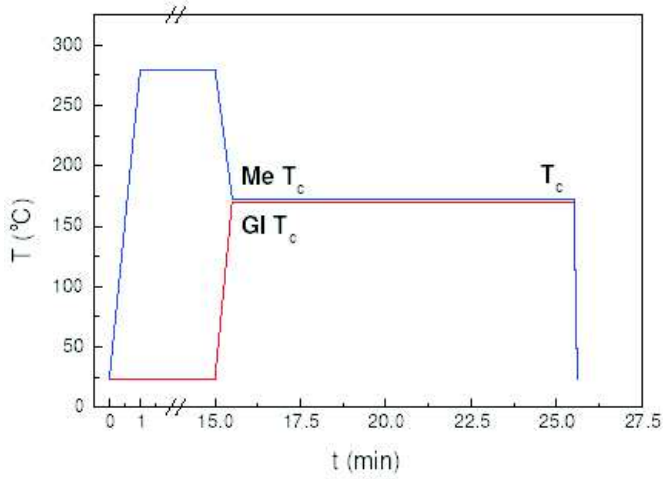

Figure 5.2: Temperature treatment given to the PET samples when crystallising from glass or melt at a particular crystallising temperature T_c, according to [8].

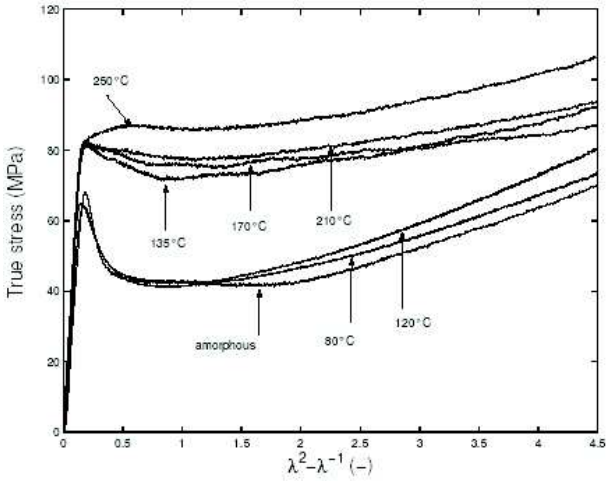

Figure 5.3: Compression stress-strain relationships of glass-crystallised PET as a function of isothermal annealing temperature T_c, according to [8].

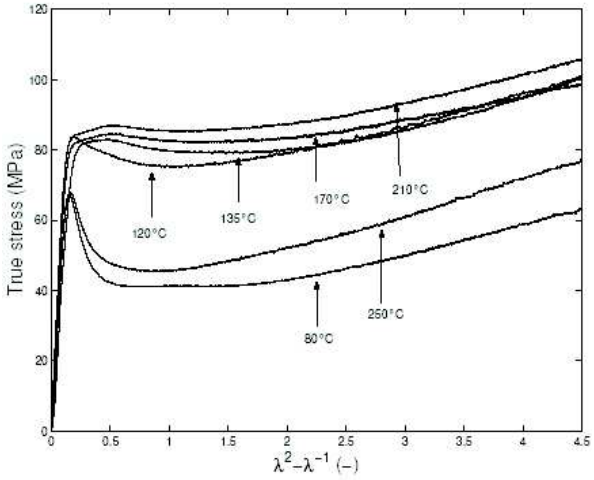

Figure 5.4: Compression stress-strain relationships of melt-crystallised PET as a function of isothermal annealing temperature T_c, according to [8].

a decreased strain softening. The sample cooled slowly from melt show a high crystallinity and is brittle.

A sudden jump of the yield properties at certain value of T_c is explained in [8] using the three-phase model, in which the amorphous phase is divided into a rigid amorphous fraction and a mobile amorphous fraction.

Figure 5.5 shows tensile behaviour of amorphous and semi-crystalline PET at a room temperature [8]. The curves for semi-crystalline PET samples correspond to different crystallisation procedure resulting in different degree of crystallisation. The amorphous

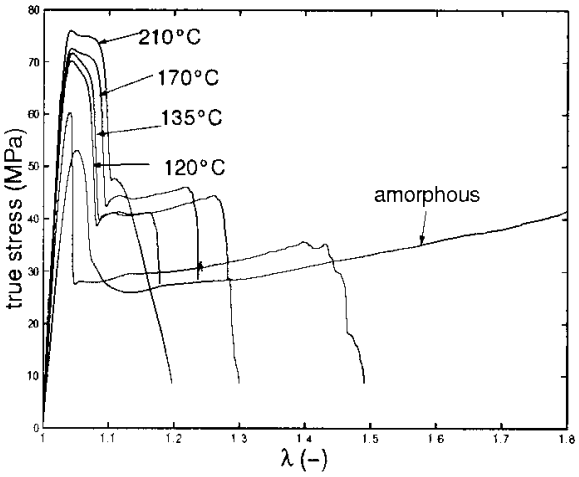

Figure 5.5: Tension stress-strain relationships of amorphous and glass-crystallised PET as a function of isothermal annealing temperature T_c, according to [8].

PET exhibits typical ductile behaviour under tension whereas semi-crystalline PET samples show brittle failure, soon after the neck is formed.

Chapter 6

Properties and deformation behaviour of the polymer–metal laminate

6.1 Introduction

The mechanical properties of the polymer (PET in this case), metal (steel) and polymer–metal interface together determine the strength of the laminate, cf. [8]. This chapter gives an insight into the polymer–metal deformation behaviour, with mechanical properties of the laminate looked upon as a result of the mechanical properties of bulk properties of constituent materials, and the effect of interaction of the polymer and metal.

6.2 Mechanical properties of steel

Steel used in the polymer–steel laminate used in packaging industry is one of the steel grades with mechanical properties suitable for deep drawing process.

Figure 6.1 [8] shows stress–strain curves for two steel grades, ECCS and IF steel, determined in a uniaxial tension test. ECCS steel shows macroscopically homogeneous deformation until the tensile strength is reached at a stress (approximately 440 MPa), after which ductile failure occurs at macroscopic strain of approximately 20%. During preparation of a laminate, the steel has to undergo a treatment at relatively high temperature (280°C), which results in a change of the mechanical behaviour [8]. Even a brief exposure of 3 sec of ECCS, to temperature as high as 280°C was found to result in an increase in yield stress and the appearance of a yield drop that leads to softening behaviour of the material, causing localization of deformation on straining. IF steel does not show any change in its mechanical behaviour even after heating at 280°C for

10 minutes. If steel can be deformed to strain of 25% before ductile failure occurs.

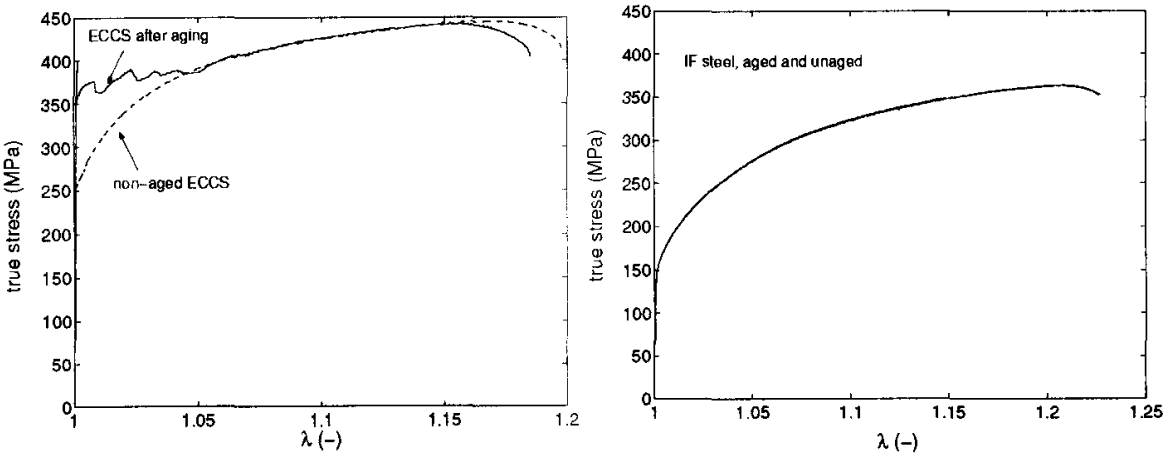

Figure 6.1: Tension stress-strain relationships of two steel grades; a) ECCS (Electrochemically Chromium Coated Steel) before and after exposure to 280°C for 3 seconds b) IF steel (From [8]).

6.3 Mechanical properties of PET

Mechanical properties of PET have been discussed more in detail in Sec. 5.4. In uniaxial tension (see Fig. 5.5), amorphous PET first undergo elastic deformation (approxiamtely up to strains of 4%, cf. [8]), followed by yielding, strain softening and strain hardening. Mechanical properties of semi-crystalline PET depend on the crystallization process and the polymer structure formed by the three phases formed in crystallization, crystalline fraction and dual amorphous phases, the rigid and mobile amorphous fractions. The quantitative fractions of each phase and their individual contributions will determine the mechanical behaviour exhibited by a semi-crystalline PET. The most striking transition in mechanical behaviour and microstructure occurs around 120°C, when crystallizing PET from the glass, since this temperature signifies the onset of thermal crystallization within 10 minutes interval. This transition has great impact on the intrinsic mechanical properties of PET, and is thus also an important factor influencing the deformation behaviour of the coating of the laminate (see Sec. 5.4).

It can be expected that using amorphous PET coating on steel will result in more stable deformation of the laminate than when using semi-crystalline PET exhibiting brittle failure soon after the neck is formed.

6.4 Deformation mechanisms of the polymer-metal laminate

Polymers and metals have greatly different material properties as it can be seen in Fig. 6.2. Macroscopic strain to fracture of both steels (ECCS and IF) represented in this figure is larger than the macroscopic yield strain for PET, but much smaller than the strain to break of PET. When the two materials materials are assembled to form a

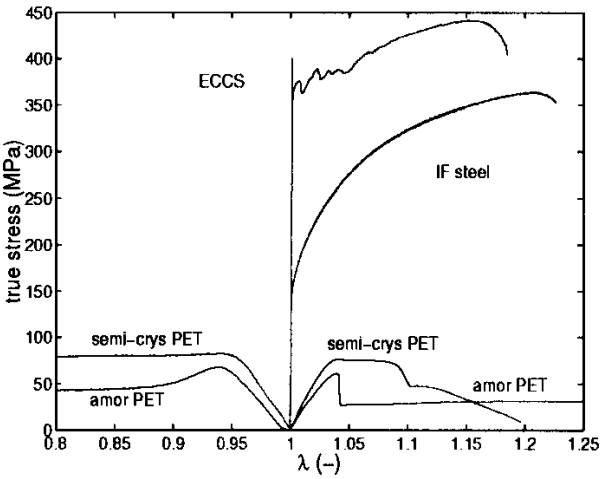

Figure 6.2: Stress–strain of the laminate bulk materials: amorphous and semi-crystalline PET and IF and ECCS steel in uniaxial compression and tension, (From [8]).

composite material, the effective behaviour may be different from the laminate base materials behaviour under similar conditions, cf. [8].

Figure 6.3 [8] illustrates schematically stress–strain curves for uniaxial tensile deformation for base materials of a typical PET-steel laminate. The deformation for the separate materials can be divided into elastic and plastic regions. In the elastic region deformation is homogeneous and in the plastic the deformation is essentially inhomogenous. Although in case of hardening the deformation macroscopically may be homogeneous, it is inhomogenous at the microscopic level.

Figure 6.3 [8] indicates different deformation regimes of the laminate. Region 1 corresponding to the elastic deformation of both base materials. In region 2 the metal enters plastic deformation while the polymer is still deforming elastically. Finally, as the strain increases, both the metal and polymer deform non-homogeneously, in region 3. Providing the adhesion at the interface is sufficient for the laminate to survive deformation in region 1, deformation of the materials 2 and 3 will differ from that of the free materials because of the boundary conditions posed on the deformation by the

interface. In region 2 the PET must adapt to the highly localized deformation at the interface. In region 3 the supported PET, if adheres, deforms to a macroscopic strains that is intrinsically unstable in the free PET. During the deformation of a laminate, however, the supported PET can be loaded to larger strains than a free film can. The problem of necking (strain localization) is circumvented thanks to the load carrying by adhesive bonds at the interface.

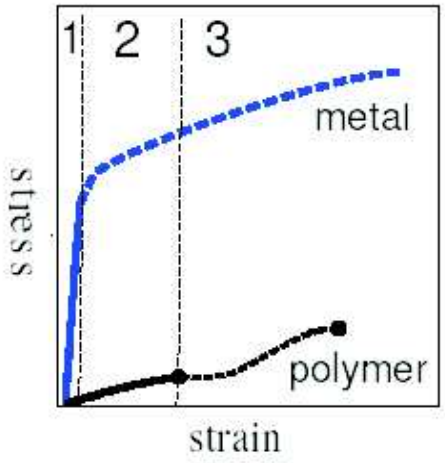

Figure 6.3: Stress-strain curves of the base materials (steel and polymer) of the laminate; region 1: elastic deformation of polymer and metal; region 2: elastic deformation of polymer and plastic deformation of metal; region 3: plastic deformation of polymer and metal; according to [8].

6.5 Mechanism of the polymer–metal interface deformation

Figure 6.4 illustrates a possible mechanism of the polymer–metal interface deformation with voids, localized deformation in the polymer, and new interface formation. Because of the much higher moduli the metal will dominate the deformation of the interface. At some scale the inhomogeneity of plastic deformation has to become apparent in the deformation of the interface. This is illustrated in Fig. 6.4 by a number of microscopic steps, that may result from single dislocations or from slip bands in the metal As a result of the deformation inhomogeneity stresses and strains near the interface will be distributed inhomogeneously. The resulting localization of stress and strain may be relieved either by delamination or plastic deformation or cracking of the supported polymer layer. Which mechanisms prevails depends on the adhesion and the properties of the polymer layer. Since the metal starts deforming plastically before the polymer, it

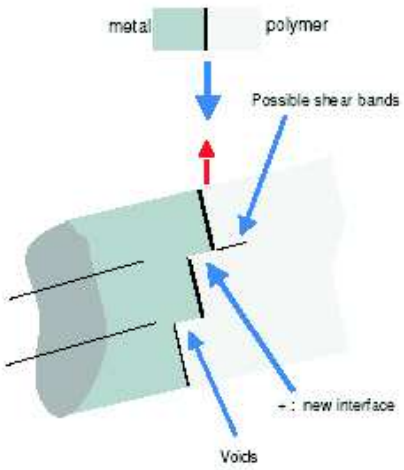

Figure 6.4: Mechanism of the polymer–metal interface deformation, according to [8].

might be expected that essentially plastic behaviour of the polymer will be locally triggered by these stress concentrations at the deforming interface at macroscopic strains that are below the macroscopic yield strain of the pure polymer. Once the deformation has reached the plastic yield strain of the polymer the adhesion at the interface may have quite a different effect, because macroscopic localization (neck formation) of the polymer is impossible. Since the polymer is intrinsically unstable (intrinsically softening) above the yield strain some localizing plastic deformation mechanism has to appear throughout the polymer. Two other interesting points about the plastic deformation of the interface are the expected appearance of fresh metal at the interface and possibly the appearance of voids or cracks. If the atoms at the interface are able to bond to the metal, there need not to be voids, but if it is not the case, voids or cracks must certainly appear, and could be unstable upon further deformation and initiate macroscopic delamination.

Chapter 7

Basic assumptions of the constitutive model of the polymer-metal laminate

7.1 Introduction

In a Draw Wall-Ironing (DWI) production process the sheet is subjected to a deep drawing step followed by several wall-ironing steps depending on the required height of the can. During forming process the polymer-metal laminate undergoes high deformations at high deformation rates and high hydrostatic pressures for in a short time period. Temperature fluctuations occur when passing under the punch and die. These extreme forming process conditions result in large strains and stresses in the metal, polymer and polymer–metal interface. High compressive stresses in polymer during forming introduce changes in microstructure of the polymer. When modelling the deformation of the laminate, the mechanical response of bulk materials (polymer and metal) as well as the response at the interface have to be taken into account. Failure of either material or of the interface could lead to ultimate failure of the laminate.

7.2 Constitutive model of steel

Steel substrate of the laminate during can manufacturing process undergoes large deformations at high deformation rates. Plastic deformation may bring about temperature increase. Although the temperature may be considerably low for steel, but the same level could be significant to cause changes of polymer properties. Therefore the thermo-mechanical coupled analysis of the forming process of the laminate may be necessary. Constitutive model of steel should take into account large elasto-plastic deformations. Influence of temperature and the strain-rate effect should also be considered.

7.3 Constitutive model of polymer coating

During mechanical forming processes, the laminates are exposed to large deformations at high strain rates, high pressures and increased temperature.

Exact constitutive modelling would require identification of several process. In many cases consideration of a dominant glass transition of the amorphous phase gives satisfactory description of the material behaviour, cf. [11].

Polymer deformation can be split into visco-elastic and plastic part. The material shows initially visco-elastic behaviour, followed by yield and a substantial intrinsic softening, continued with strain hardening behaviour [12]. Plastic part is not recovered after unloading during time equivalent to the loading time, while the visco-elastic part is recovered under such conditions.

At the yield point polymer behaviour changes from the linear elastic with relatively high modulus to rubber-like with a low modulus. To describe plastic flow in polymers different theories have been developed. In the Eyring flow theory [**?**] plastic flow is a macroscopic effect of the basic molecular processes involving the motion of chain segments occurring with a frequency dependent on a potential energy barrier, which changes upon stressing.

7.4 Constitutive model of the polymer–metal interface

In the manufacturing process the interface is subjected to high stresses. It is crucial that the adhesion between the polymer and the metal is strong enough to endure tough forming conditions. Adhesion dictates the deformation of the laminate and its ultimate performance. Constitutive model should properly calculate stresses at the interface, take into account possible degradation of the interface strength and complete delamination.

Chapter 8

Review of constitutive models of polymers

8.1 Introduction

With the growing use of polymers in different structures, a lot of research effort was dedicated to the development of constitutive models for polymeric materials.

Most research work was done for amorphous polymers. Special constitutive models have also been developed for semi-crystalline polymers although the performance is not so good. However, in many cases phenomenological constitutive models developed for glassy polymers can be successfully used for semi-crystalline polymers, as well.

Review of different approaches to modelling of deformation of polymers can be found in [13]. Rich bibliography on the numerical modelling of polymers is given in [14, 15].

8.2 General classification of material models

A complex deformation behaviour of polymers has been described using different constitutive models and different theories based on elasticity, viscoelasticity, elasto-plasticity or viscoplasticity [13, 14, 15]. At this stage it would be useful to introduce a general classification of the material behaviour and corresponding constitutive models. This will allow us to classify different constitutive models used for polymers.

Based on the experimental observation of stress–strain curves the following four different categories of materials behaviour can be distinguished, cf. [16]:

- rate-independent without hystheresis,
- rate-independent with hystheresis,
- rate-dependent without hystheresis,

- rate-dependent with hystheresis.

Illustration of these four categories is given in Fig. 8.1

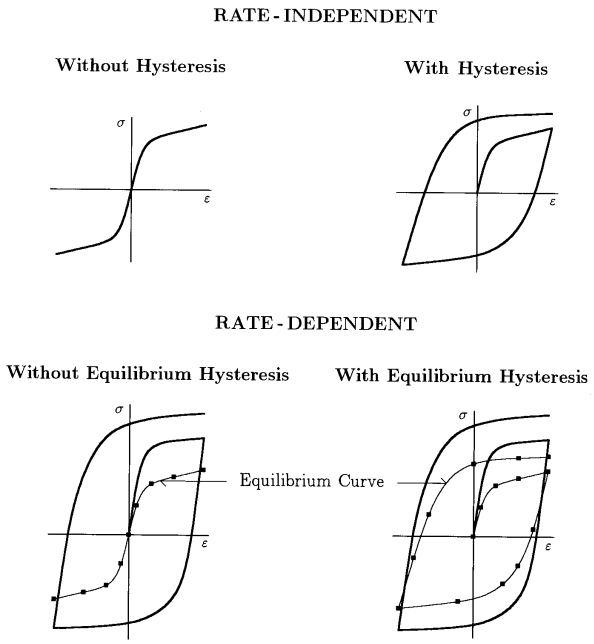

Figure 8.1: Four categories of material behaviour (after [16])

The four categories of material behaviour distinguished are matched by four categories of mathematical models, namely the theories of elasticity, plasticity, viscoelasticity and viscoplasticity as follows:

- rate-independent without hystheresis — theory of elasticity,
- rate-independent with hystheresis — theory of plasticity,
- rate-dependent without hystheresis — theory of viscoelasticity,
- rate-dependent with hystheresis — theory of viscoplasticity.

The rheological models corresponding to the four theoretical models are shown in Fig. 8.2. The rheological models consist of elastic springs, viscous dashpots and Coulomb friction elements. Figure 8.2 does not intend to to denote a concrete model — it shows only a possible representation of a given theoretical model.

Elasticity is the simplest of all constitutive models. Nonlinear elasticity is often regarded as a suitable theory to describe deformation behaviour of elastomers, if the hysteresis is sufficiently narrow to be neglected. Viscoelastic model takes into account internal friction and dissipation, assuming equilibrium hysteresis is negligibly small.

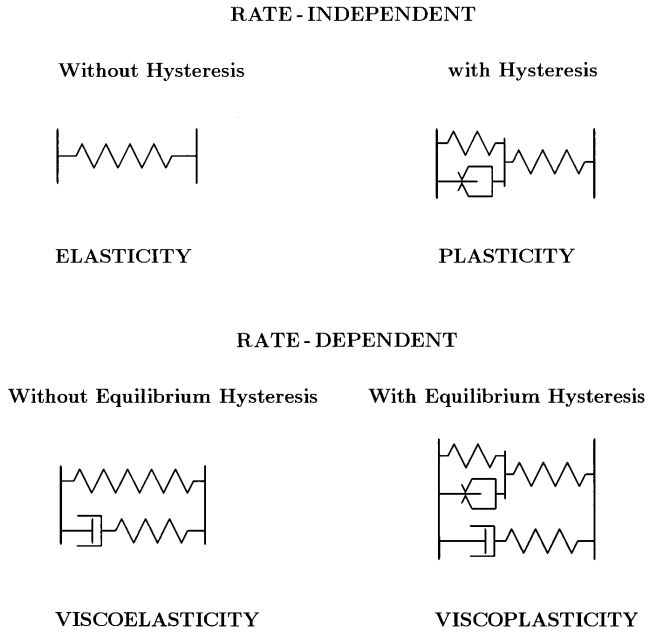

Figure 8.2: Four theories of material behaviour (after [16])

Rate independent behaviour taking into account the internal friction and hysteresis is covered by plasticity. Viscoplasticity is the most general theory which can handle both the internal friction and rate dependent equilibrium hysteresis.

8.3 Basic features of deformation behaviour of polymers

When studying the deformation behaviour of glassy polymers a distinction can be made between the linear viscoelastic region, the nonlinear viscoelastic response and the yield behaviour at high stress levels (Fig. 8.3). The linear viscoelastic deformation is adequately described using linear theory. The nonlinear regime has been described using different theories. Yield of the polymer materials is classically described by using yield criteria, of which the pressure and rate dependent Von-Mises criterion seems to be most successful. Plastic flow curve is characterized with strain softening/hardening behaviour. Initial softening often precedes hardening. Deformation behaviour of polymers has been presented more in detail in previous sections.

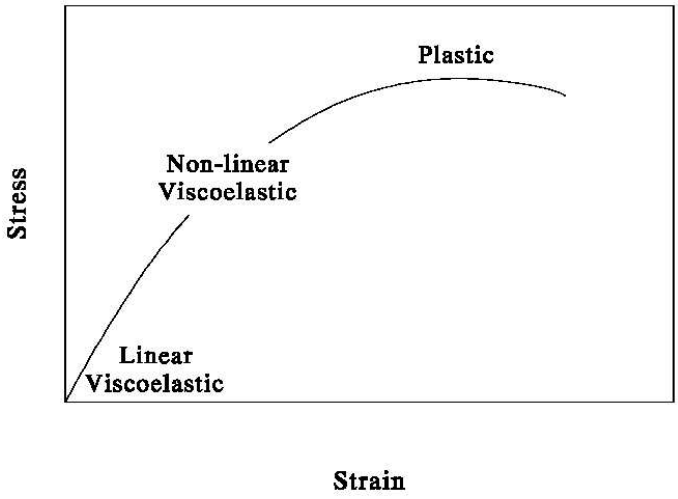

Figure 8.3: Three different stages in the deformation behaviour (after [13])

8.4 Linear viscoelastic models

Linear viscoelastic models can describe polymer deformation at the initial stage only. Viscoelastic models are represented by different combinations of viscous dashpots and elastic springs. The simplest viscoelastic models are the Maxwell model represented by a dashpot and a spring in parallel (Fig. 8.4) and the Kelvin–Voigt model represented by a dashpot and a spring in series (Fig. 8.5). In the linear case the spring represents

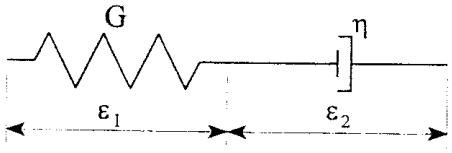

Figure 8.4: Schematic representation of the Maxwell model

the linear elastic (or Hookean) model

$$\sigma = G\varepsilon \tag{8.1}$$

and the dashpot represents the viscous (Newtonian) model

$$\sigma = \eta\dot{\varepsilon} \tag{8.2}$$

where G and η is the shear modulus and viscosity, respectively. Translating a rheological model into a one-dimensional stress–strain relationship is achieved using the

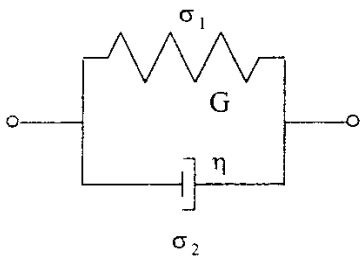

Figure 8.5: Schematic representation of the Kelvin–Voigt model

geometric condition of compatibility in the case of elements in series and the mechanical condition of the momentum balance in the case of elements in parallel. Thus for the Maxwell model we have

$$\varepsilon = \varepsilon_1 + \varepsilon_2 \tag{8.3}$$

and for the Kelvin–Voigt model

$$\sigma = \sigma_1 + \sigma_2 \tag{8.4}$$

This procedure leads to differential equations relating stress $\sigma(t)$ and strain $\varepsilon(t)$. The solution of the differential equation for the Maxwell model for the stress relaxation problem gives, cf. [1]:

$$\sigma(t) = \sigma(0^+) \exp\left(-\frac{t}{\tau}\right) \tag{8.5}$$

where $\tau = \eta/G$ is called the relaxation time. The relationship (8.5) allows us to obtain the expression for the relaxation modulus $G(t)$ for the Maxwell model as

$$G(t) = \frac{\sigma(t)}{\varepsilon_0} = \frac{\sigma(0^+)}{\varepsilon_0} \exp\left(-\frac{t}{\tau}\right) = G \exp\left(-\frac{t}{\tau}\right) \tag{8.6}$$

The Kelvin–Voigt model is adequate to describe creep behaviour. The solution of the creep problem in this case gives, cf. [1],

$$\varepsilon(t) = J\sigma(0^+) \left[1 - \exp\left(-\frac{t}{\tau}\right)\right] \tag{8.7}$$

where $J = 1/G$ is compliance and $\tau = \eta/G$ is the retardation time. The creep compliance function is given by

$$J(t) = \frac{\varepsilon(t)}{\sigma_0} = J \left[1 - \exp\left(-\frac{t}{\tau}\right)\right] \tag{8.8}$$

The Maxwell model is unable to represent creep behaviour of viscoelastic materials, nor can the Kelvin–Voigt model describe stress relaxation. To obtain a better representation of a viscoelastic material more complex model must be used.

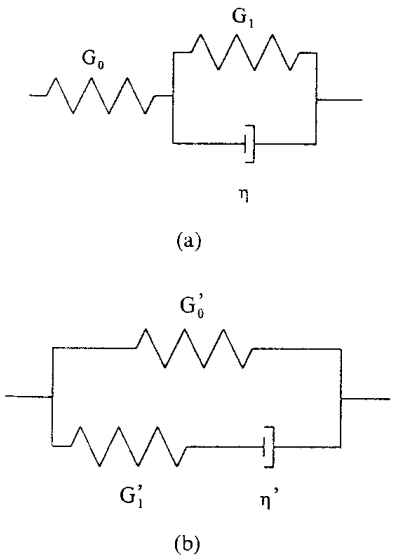

Figure 8.6: Two equivalent schemes of the Zener's solid

Figure 8.6 shows representation of the three-element standard solid (or Zener's solid) composed of either a Kelvin–Voigt element in series with a spring or, alternatively, a Maxwell element in parallel with a spring. The Burgers model shown in Fig. 8.7 is a combination of the Maxwell model with a Kkelvin–Voigt element.

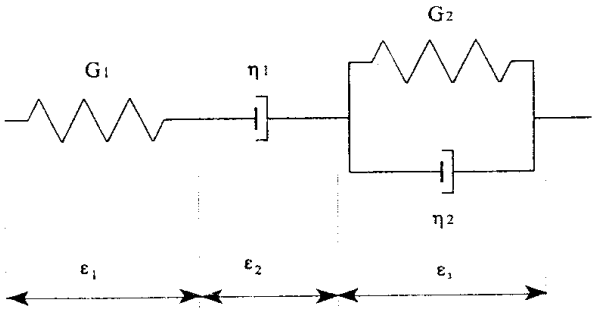

Figure 8.7: Schematic representation of the Burgers model

The elementary models are characterized by a single relaxation or retardation time. Real materials are characterized with a distribution of relaxation or retardation times. One can obtain such a distribution by taking generalized models composed of many Maxwell elements in parallel (Fig. 8.8a) or of a number of Kelvin–Voigt elements in series (Fig. 8.8b). In Fig. 8.8a an elastic element has been added to account for the instantaneous response. In Fig. 8.8b a Maxwell element has been added in series to reflect liquid behaviour.

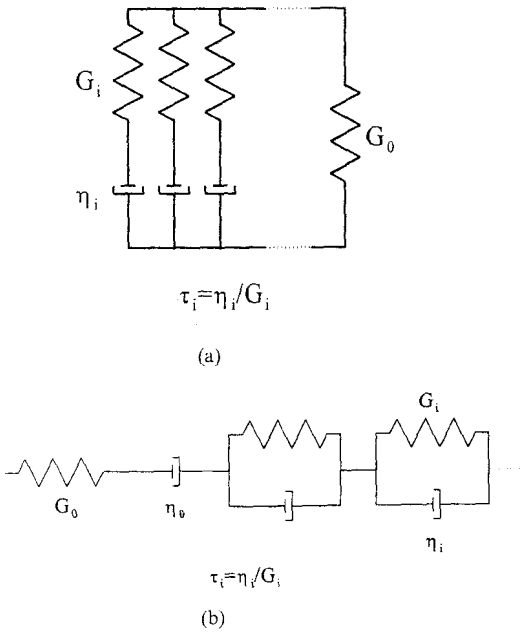

Figure 8.8: Generalized models a) Maxwell's elements in parallel, b) Kelvin–Voigt elements in series

The relaxation or retardation functions for these models in the case of a discrete distribution of relaxation or retardation times are given by, cf. [1]:

$$G(t) = G_e + \sum_{i=1}^{n} G_i \exp\left(-\frac{t}{\tau_i}\right) \tag{8.9}$$

$$J(t) = J_g + \sum_{i=1}^{n} J_i \left[1 - \exp\left(-\frac{t}{\tau_i}\right)\right] + \frac{t}{\eta_0} \tag{8.10}$$

8.5 Elastoplastic models

In the classical approach, solid polymers are considered to be ideally-plastic materials. This implies a description of the yield behaviour by means of a yield criterion. The yield stress of polymers depends on the hydrostatic pressure as it was stated in Sec. 3.7. The classical yield criteria, the Tresca criterion

$$\sigma_1 - \sigma_3 = 2\tau_y\,, \quad \text{(assuming } \sigma_1 > \sigma_2 > \sigma_3\text{)} \tag{8.11}$$

and the Mises–Huber criterion

$$(\sigma_1 - \sigma_2)^2 + (\sigma_2 - \sigma_3)^2 + (\sigma_3 - \sigma_1)^2 = 6\tau_y^2\,, \tag{8.12}$$

do not take into account the pressure dependency of the yield stress. In the above Eqs. (8.11) and (8.12) σ_1, σ_2 and σ_3 are principal stresses and τ_y is the yield stress in pure shear test. The relationship between shear yield stress τ_y and tensile yield stress σ_y is

$$\sigma_y = 2\tau_y \tag{8.13}$$

for the Tresca criterion and

$$\sigma_y = \sqrt{3}\tau_y \tag{8.14}$$

for the Mises–Huber criterion. The Tresca and Huber–Mises yield criteria can be easily modified to take into account the pressure dependence. The shear yield stress τ_y can be expressed as a function of hydrostatic pressure p as follows

$$\tau_y = \tau_y^0 - \mu p \tag{8.15}$$

where τ_y^0 is yield stress at zero pressure, μ is a material constant that describes the effect of pressure, and p is given by

$$p = \frac{\sigma_1 + \sigma_2 + \sigma_3}{3} \tag{8.16}$$

Here the hydrostatic pressure is assumed positive for tensile loading and negative for compression. Modified yield surfaces for plane stress conditions ($\sigma_3 = 0$) are shown in Fig. 8.9.

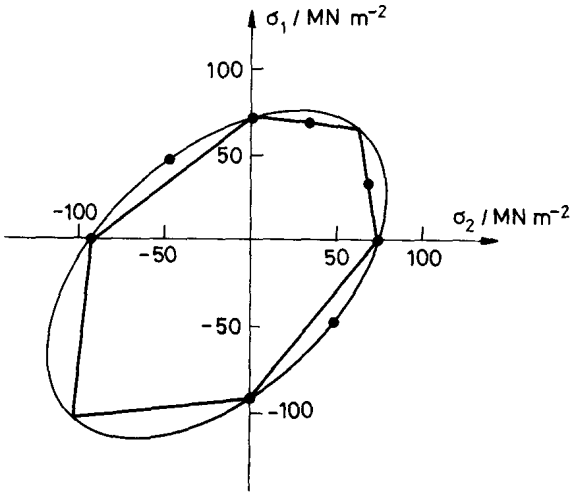

Figure 8.9: Yield stress according the Tresca and Mises–Huber criteria accounting for pressure dependency (according [1])

An elastoplastic constitutive model of cold drawing of polycarbonates has been developed by Masud [17] and by Masud and Chudnovsky [18]. The model is based on

the representation of cold drawing as a double glass transition, i.e. transition from a glass into a rubbery state, when a certain yield surface in the stress space is reached, and a transition back to the glassy state upon unloading or when a certain molecular orientation (draw ratio) is achieved. The stretching process in the rubbery state is modeled by a hyperelastic extension of the J_2-flow theory to the finite strain range. An appropriate yield surface and an associative flow rule (defined via the Kuhn–Tucker optimality conditions) are presented to simulate this process. The isochoric constraint during double glass transition is treated via en exact multiplicative decomposition of the deformation gradient into volume preserving and spherical parts.

8.6 Nonlinear viscoelastic models

Elastoplastic models are typical for solid material models. Polymer deformation behaviour can be treated using a fluid-like approach in which solid polymers are treated as strongly nonlinear viscoelastic fluids with very high relaxation times. In this approach the deformation behaviour is described using a nonlinear Maxwell element with a single, temperature and stress-activated relaxation time. The idea dates back to Tobolsky and Eyring [19], it was employed in a class of models, including the Haward and Thackray model [20], the BPA model proposed by Boyce et al. [21], the "full chain model" by Wu and van der Giessen [22], and the "modified Leonov model" proposed by Tervoort [6]. In all these models, no explicit use is made of a yield criterion.

Schematic representation of the model proposed by Haward and Thackray [20] is shown in Fig. 8.10. The initial elastic response is characterized by a linear spring,

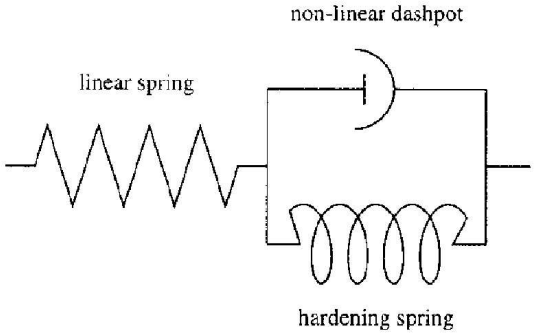

Figure 8.10: Schematic representation of the model proposed by Haward and Thackray [20]

the yield point is determined by a non-linear dashpot with a stress dependent Eyring viscosity [23] and the strain hardening response is modelled by a hardening spring. Use of a single relaxation time in the Haward and Hackaray model results in a sharp

transition from solid-like to fluid-like behaviour, almost identical to an elastic-perfectly plastic response employing a rate dependent yield criterion.

The Haward and Thackray model was generalised to three dimensions in the BPA model proposed by Boyce et al. [21]. Similarly to the original one-dimensional version, visco-elastic behaviour prior to yielding (which is observed in experiments) is not taken into account, since only one stress dependent relaxation time is used.

To improve the description of the visco-elastic behaviour, Tervoort [6] proposed the use of a spectrum of relaxation times. This can be looked upon as a number of

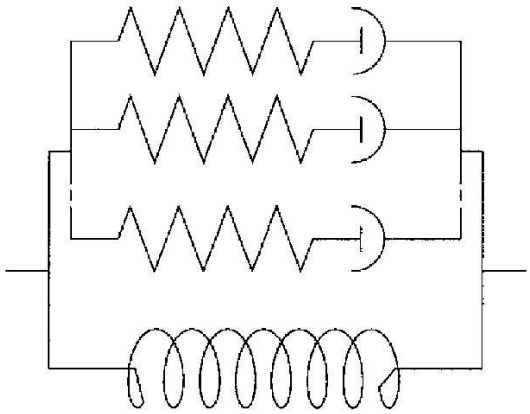

Figure 8.11: Schematic representation of the multi-mode model proposed by Tervoort [6]

Maxwell models in parallel (Fig. 8.11), each consisting of a linear spring and non-linear dashpot in series. It is a compressible generalisation of the Leonov model [24] proposed by Baaijens [25]. Tervoort separated the elastic hydrostatic stress and the visco-elastic deviatoric stress in each Maxwell element and named such an element a single "Leonov mode". Plastic flow of polymers was described by Tervoort using non-Newtonian viscous flow rule with the viscosity calculated from a generalised Eyring equation, cf. Sec. 8.7. Strain hardening was modelled by a hardening spring parallel to the Leonov modes (Fig. 8.11). Each of the Leonov modes is capable to describe rate dependent yield behaviour at finite deformations (Fig. 9.6). The stress in the Leonov mode, activating plastic flow, is called the driving stress, while the stress caused by strain hardening is called the hardening or back stress. The contribution of the driving stress and the hardening stress for an amorphous polymer is shown in Fig. 9.6.

8.7 The Eyring model of viscoelasticity

Plastic flow of polymers is often described using a non-Newtonian viscous flow rule with the viscosity calculated from a generalised Eyring equation, cf. [6]. This section

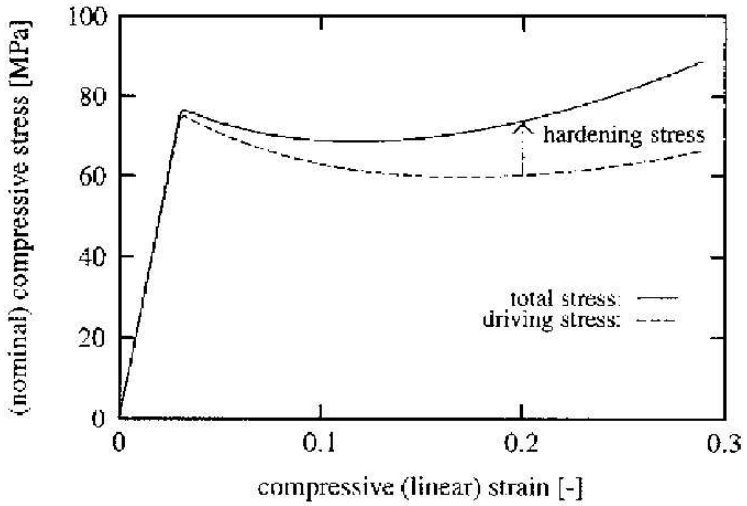

Figure 8.12: Simulation of a uniaxial compression test using a single Leonov mode with a hardening spring in parallel

presents basic concepts of the Eyring model of viscoelasticity following [1].

The Eyring model [23] was developed to describe the viscous flow in liquids. The ideas of this model can also be applied to describe yield behaviour of glassy polymers.

The model assumes that when a segment of a macromolecule has to move to an adjacent site it must pass over an energy barrier represented as ΔE^* (see Fig. 8.13a). In the absence of stress, the segments of the polymer jump over the barrier infrequently,

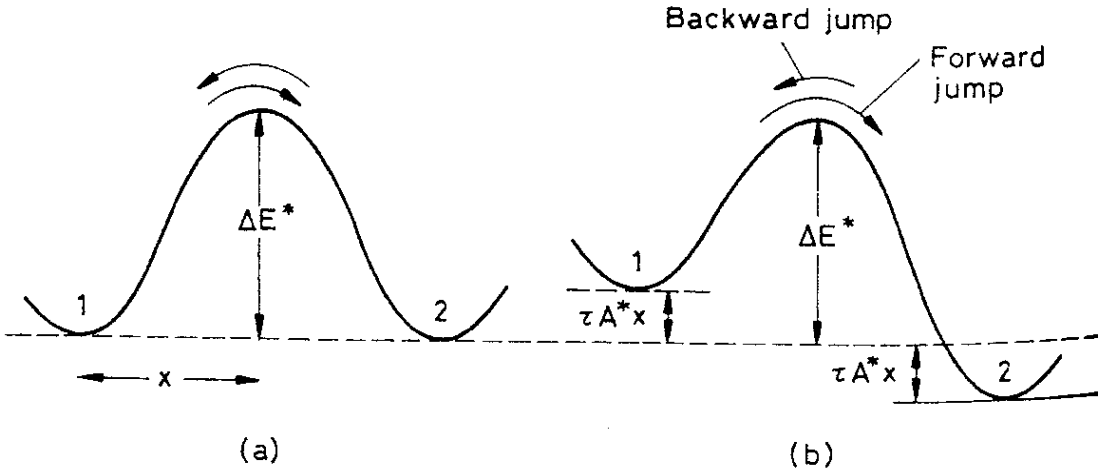

Figure 8.13: Eyring's model; a)

and they do so in random directions. The frequency with which the segments jump

the barrier is represented by the Arrhenius equation,

$$\nu_0 = A' \exp\left[-\frac{\Delta E^*}{KT}\right] \tag{8.17}$$

where A' is a constant.

According to the Eyring model, the application of a shear stress modifies the barrier height. In the direction of stress, the rate at which segments jump forward over the barrier will be increased, and consequently the height of the barrier will be reduced. If τ is the shear stress applied and A^* is the effective area of the polymer segment, the height of the barrier is reduced by by $\tau A^* x$, which corresponds to the work done in moving a segment a distance x. This is illustrated in Fig. 8.13b. The frequency with which the segments jump the new barrier in the forward direction is

$$\nu_1 = A' \exp\left[-\frac{\Delta E^* - \tau A^* x}{KT}\right] == A' \exp\left(-\frac{\Delta E^*}{KT}\right) \exp\left(\frac{\tau A^* x}{KT}\right) \tag{8.18}$$

Since the frequency with which the polymer segments jump in the backward direction is very low, the reverse jump rate can be neglected the net rate flow is assumed to be given by Eq. (8.18). The product $A^* x = V^*$ has the dimensions of volume and is called the activation volume.

Yielding can be considered as viscous flow in which activation energy barrier ΔE^* for load shear displacements of polymer segments is decreased by the applied stress τ. The imposed strain rate, $\dot{\varepsilon}_y$ can be considered proportional to the net rate flow, and τ can be considered the maximum shear stress. Then $\tau = \sigma_y/2$, σ_y being the tensile yield stress. Consequently, Eq. (8.18) becomes

$$\dot{\varepsilon}_y = \dot{\varepsilon}_0 \exp\left(\frac{\Delta E^*}{KT}\right) \exp\left(\frac{\sigma_y V^*}{2KT}\right) \tag{8.19}$$

where $\dot{\varepsilon}_0$ is a constant.

Equation (8.19) can be rearranged as

$$\sigma_y = \left[2.303K \log\left(\frac{\dot{\varepsilon}_y}{\dot{\varepsilon}_0}\right) + \frac{\Delta E^*}{T}\right]\left(\frac{2T}{V^*}\right) \tag{8.20}$$

Equation (12.21) describes the temperature and strain rate dependence of the yield stress, σ_y.

Figure 8.14 shows the plots of σ_y vs. $\log \dot{\varepsilon}_y$ for polycarbonate ($T_g = 140°\text{C}$) in the range of temperature $21.5°\text{C} < T < 140°\text{C}$. The data in this figure indicate that the Eyring model accounts for many features of yielding in glassy polymers. The negative temperature dependence of the yield stress σ_y is revealed. The plots show the positive strain rate dependence of σ_y.

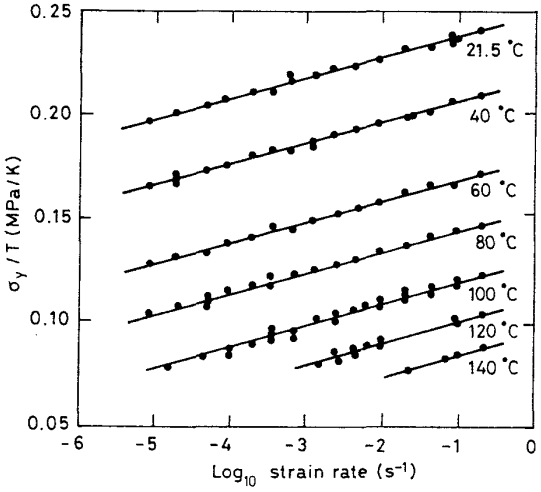

Figure 8.14: Eyring plot of σ_y/T versus $\log \dot{\varepsilon}$ for polycarbonate (From [26])

Equation (12.21) fails when it is used to describe the yield behaviour of polymers over a wide range of temperature. This has led to a modification of the model [27] by an assumption that the deformation process involves two different flow processes that have different values of ΔE^* and V^*. Another modification [28] includes the effect of hydrostatic pressure.

8.8 Viscoplastic models

The theory of viscoplasticity describes rate-dependent material behaviour with equilibrium hysteresis. Viscoplasticity is the most general material model. In principle, it considers all macroscopically observable phenomena.

Basically, there are three different approaches to development of viscoplastic models, cf. [16]:

- introducing static yield surface defining elastic domain
- a uniform formulation of evolution equations without yield surface
- decomposition of the total stress into rate-independent equilibrium stress and rate-dependent overstress

The first concept was introduced by Perzyna [29]. In this approach states outside the static yield surface lead to the evolution of inelastic deformations. It can be viewed as a generalisation of the classical theory of plasticity, which is included as a special case.

The second method of modelling viscoplasticity has no need for yield surfaces or the case distinction connected with it. A system of nonlinear diferential equations

describes material properties with internal variables used to describe process dependent material behaviour in a uniform manner. These constitutive models are named unified viscoplasticity models, eg. [30].

A third way of constructing constitutive models of viscoplasticity is built on the a priori decomposition of the total stress into an equilibrium part (equilibrium stress) and non-equilibrium part (overstress). In this concept, the relations between the equilibrium stress and overstress become uncoupled to large extent from each other, resulting in a modular structure of the constitutive model. This kind of models were developed by Krempl [31] and Krempl et al [32]. Their application to polymer materials is presented in [33]. Recent developments and application of this model to polymer materials can be found in [34].

8.9 Conclusions and recommendations

The present work is concerned on the polymer coating of the sheet used for the can manufacture. In this case deformation of the polymeric material at large plastic strains is of greatest importance, small visco-elastic strains are of minor importance and the viscous behaviour prior to yielding can be neglected. This means that in case of models employing the Leonov modes, only one mode can be considered. This assumption minimizes the number of model parameters necessary to determine.

Chapter 9

Selected constitutive models

9.1 Introduction

This chapter presents selected constitutive models suitable to polymer modelling. First the description of finite inelastic deformations employ is presented. This description is generally accepted as the most suitable framework for the development of constitutive models for large viscoelastic or elasto-plastic/viscoplastic deformation. Most of the assumptions are common for the constitutive models of polymers presented later in this chapter.

9.2 Kinematics of finite inelastic deformations

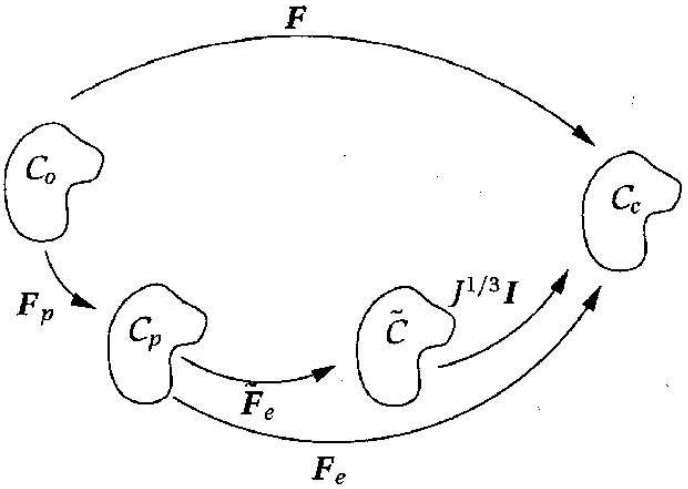

Figure 9.1: Decomposition of the continuum deformation

The deformation of a continuum is shown schematically in Fig. 9.1. The transformation from the undeformed configuration C_0 to the deformed one C_c is described by the deformation gradient tensor $\mathbf{F}$. An existence of a stress-free plastic intermediate configuration C_p is postulated. This assumption leads to the multiplicative decopmosition of the deformation gradient tensor $\mathbf{F}$ into an elastic and plastic part, $\mathbf{F}_e$ and $\mathbf{F}_p$, respectively

$$\mathbf{F} = \mathbf{F}_e \mathbf{F}_p \tag{9.1}$$

It is assumed that volume does not change during plastic deformation

$$J_p = \det \mathbf{F}_p = 1 \tag{9.2}$$

so

$$J = \det \mathbf{F}_p = \det \mathbf{F}_e \tag{9.3}$$

Following Simo [35] the elastic deformation can be decoupled into volumetric and isochoric (volume preserving) distortional deformation. Thus we have another intermediate configuration $\bar{C}$ (Fig. 9.1) and the following multiplicative decomposition is introduced

$$\mathbf{F}_e = \mathbf{F}_e^v \bar{\mathbf{F}}_e \tag{9.4}$$

where the tensor $\bar{\mathbf{F}}_e$ describes the isochoric deformation and

$$\mathbf{F}_e^v = J^{1/3} \mathbf{I} \tag{9.5}$$

represents the volumetric deformation. The elastic left Cauchy–Green tensor $\mathbf{B}_e$ is related to the left Cauchy–Green tensor for the isochoric deformation as follows $\bar{\mathbf{B}}_e$

$$\mathbf{B}_e = \mathbf{F}_e \mathbf{F}_e^T = J^{2/3} \bar{\mathbf{F}}_e \bar{\mathbf{F}}_e^T = J^{2/3} \bar{\mathbf{B}}_e \tag{9.6}$$

The velocity gradient tensor $\mathbf{L}$ is given by

$$\mathbf{L} = \frac{\partial \mathbf{v}}{\partial \mathbf{x}} = \dot{\mathbf{F}} \mathbf{F}^{-1} \tag{9.7}$$

using (9.1) can be split into an elastic and plastic part as

$$\mathbf{L} = \mathbf{L}_e + \mathbf{L}_p \,, \qquad \mathbf{L}_e = \dot{\mathbf{F}}_e \mathbf{F}_e^{-1} \,, \qquad \mathbf{L}_p = \mathbf{F}_e \dot{\mathbf{F}}_p \mathbf{F}_p^{-1} \mathbf{F}_e^{-1} \tag{9.8}$$

The velocity gradient tensor $\mathbf{L}$ is often written as the sum of the symmetric deformation rate tensor $\mathbf{D}$

$$\mathbf{L} = \mathbf{D} + \boldsymbol{\Omega} \,, \qquad \mathbf{D} = \tfrac{1}{2}(\mathbf{L} + \mathbf{L}^T) \,, \qquad \boldsymbol{\Omega} = \tfrac{1}{2}(\mathbf{L} - \mathbf{L}^T) \tag{9.9}$$

which can be split into their respective elastic and plastic parts, $\mathbf{D}_e$, $\mathbf{D}_p$, $\boldsymbol{\Omega}_e$ and $\boldsymbol{\Omega}_p$

$$\mathbf{D} = \mathbf{D}_e + \mathbf{D}_p \,, \qquad \boldsymbol{\Omega} = \boldsymbol{\Omega}_e + \boldsymbol{\Omega}_p \tag{9.10}$$

where

$$\mathbf{D}_e = \tfrac{1}{2}(\mathbf{L}_e + \mathbf{L}_e^T)\,, \qquad \boldsymbol{\Omega}_e = \tfrac{1}{2}(\mathbf{L}_e - \mathbf{L}_e^T) \tag{9.11}$$

$$\mathbf{D}_p = \tfrac{1}{2}(\mathbf{L}_p + \mathbf{L}_p^T)\,, \qquad \boldsymbol{\Omega}_p = \tfrac{1}{2}(\mathbf{L}_p - \mathbf{L}_p^T) \tag{9.12}$$

The decomposition defined by Eq. (9.1) is not unique with respect to rotation contribution. Different assumptions are possible regarding the rotations. The following assumptions have been proposed by Boyce et al. [21, 36]:

I. Symmetric elastic deformation gradient tensor

In this case, the elastic rotation tensor $\mathbf{R}_e$ resulting from the polar decomposition of the elastic deformation gradient $\mathbf{F}_e$

$$\mathbf{F}_e = \mathbf{R}_e\mathbf{U}_e \tag{9.13}$$

is chosen equal to the second order unit tensor

$$\mathbf{R}_e = \mathbf{I} \tag{9.14}$$

This assumption means that the relaxed configuration is obtained from the current configuration by elastic unloading without rotation. This means

$$\mathbf{F}_e = \mathbf{F}_e^T \tag{9.15}$$

II. No elastic spin.

The elastic and plastic spin tensors are assumed as follows

$$\boldsymbol{\Omega}_p = \boldsymbol{\Omega}\,, \qquad \boldsymbol{\Omega}_e = \mathbf{0} \tag{9.16}$$

III. No plastic spin.

The elastic and plastic spin tensors are defined by

$$\boldsymbol{\Omega}_p = \mathbf{0}\,, \qquad \boldsymbol{\Omega}_e = \boldsymbol{\Omega} \tag{9.17}$$

This choice is employed for instance in the compressible Leonov model [6] presented in Sec. [**?**].

These options have been verified in different tests by Timmermans [11] and it was demonstrated that the Leonov model with assumptions I and II lead to unrealistic results.

9.3 J_2 plasticity model

Hyperelastic J_2 plasticity formulation has been extended and applied to modelling large deformations of polymers by Masud and Chudnovsky [18, 17]. This shows the possibility of adaptation of standard elastoplastic algorithms successfully used in metal modelling to model polymers. The theoretical model treats cold drawing of polycarbonates involving loading and unloading as the so-called double glass transition. In this concept the necking phenomenon of a glassy polymer is a special type of transformation involving a three-steps process:

(i) transformation from an isotropic glass (α state) to an isotropic rubber (rubbery mesostate β) when the yield surface in the stress space is reached during loading,

(ii) a stretching of the rubbery state,

(iii) a transformation of the stretched rubbery state into an oriented glass upon unloading, or when a certain molecular orientation (draw ratio) is achieved.

These mechanisms are illustrated in Fig. 9.2.

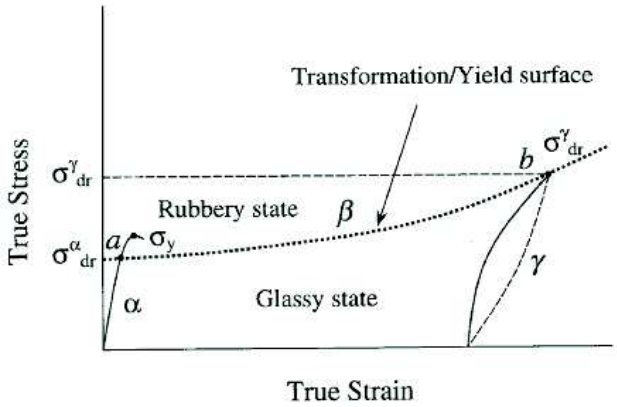

Figure 9.2: The process of cold-drawing as transitions $\alpha \rightarrow \beta \rightarrow \gamma$

In the kinematics description the multiplicative split of the deformation gradient tensor $\mathbf{F}$ into elastic and inelastic (plastic) components is assumed according to Eq. (9.1). The free energy potential is assumed in the following form:

$$\phi(\mathbf{g}, \mathbf{B}_e^{-1}, \mathbf{q}, \mathbf{F}) = \bar{\phi}(\mathbf{g}, \mathbf{B}_e^{-1}, \mathbf{F}) + \chi(\mathbf{q}) \tag{9.18}$$

where $\mathbf{g}$ is the spatial metric tensor, $\mathbf{B}_e$ is the elastic left Cauchy–Green tensor, and $\mathbf{q}$ is a set of internal variables characterizing the inelastic (plastic) response. The

hyperelastic stored energy function with uncoupled pressure relative to the intermediate (unloaded) configuration is defined as

$$\bar{\phi}(\mathbf{g}, \mathbf{B}_e^{-1}, \mathbf{F}) = U(J) + \tfrac{1}{2}\mu(\bar{I}_b e - 3) = \tfrac{1}{2}K(\lg J)^2 + \tfrac{1}{2}\mu(\bar{I}_b e - 3) \tag{9.19}$$

where $\bar{I}_b e = J^{-2/3}\mathbf{B}_e : \mathbf{g}$, K is the bulk modulus and μ is the shear modulus. The Kirchhoff stress tensor can be obtained from

$$\boldsymbol{\tau} = 2\rho_o \frac{\partial \bar{\phi}(\mathbf{g}, \mathbf{B}_e^{-1}, \mathbf{F})}{\partial \mathbf{g}} \tag{9.20}$$

The Huber–Mises yield condition is assumed

$$\bar{f}(\mathbf{g}, \mathbf{B}_e^{-1}, \mathbf{q}, \mathbf{F}) := \|\mathbf{s}\| - \sqrt{\tfrac{2}{3}}\kappa(\bar{e}^i) \leq 0 \tag{9.21}$$

where $\mathbf{s}$ is deviatoric part of the Kirchhoff stress tensor, $\mathbf{q} = \{\bar{e}^i\}$, $\bar{e}^i$ being the equivalent inelastic (plastic) flow. The associative flow rule is adopted. The state of stress during transition from the initial unoriented state into the oriented one is given by:

$$\kappa(\bar{e}^i) = \sigma_{dr}^{\alpha} + (\sigma_{dr}^{\gamma} - \sigma_{dr}^{\alpha})\left[1 - \exp\left(-\delta_1 \bar{e}^i\right)\right] + (\sigma_{dr}^{\gamma} - \sigma_{dr}^{\alpha}) \exp\left[\delta_2(\bar{e}^i - \ln \lambda_n)\right] \tag{9.22}$$

where σ_{dr}^{α}, σ_{dr}^{γ}, δ_1, δ_2 and λ_n are material specific constants. λ_n is related to the so-called maximum residual strain under uniaxial state and is termed as the draw-ratio. σ_{dr}^{α} is the stress initiating necking (Fig. 9.2). σ_{dr}^{γ} represents the true draw stress, i.e. $\sigma_{dr}^{\gamma} = \lambda_n \sigma_{dr}^{\alpha}$. It is the stress that a material particle develops once it has reached the second stable branch (i.e. the end of β state in Fig. 9.2). An example of the stress–strain curve defined by Eq. (9.22) is shown in Fig. 9.3.

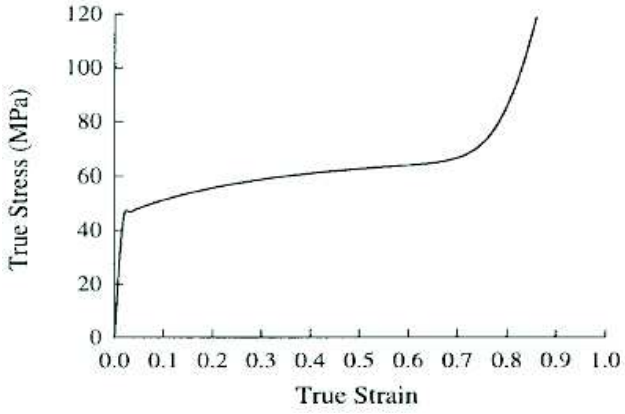

Figure 9.3: True stress–true strain curve defined by Eq. (9.22), from [18]

9.4 The Arruda–Boyce (AB) Model

The Arruda–Boyce model was developed [37, 38, 21] for predicting the large strain, time and temperature-dependent response of glassy polymers. The model incorporates the behaviour of materials characterized by an initial linear elastic response followed by yielding and then strain hardening at large deformations.

Description of large inelastic deformations is based on the multiplicative decomposition of the deformation gradient tensor $\mathbf{F}$ into elastic and plastic components as given by Eq. (9.1). The rheological representation of the Arruda-Boyce model (Fig. 9.4) is composed of two networks acting in series: an elastic network (e) and a plastic network (p).

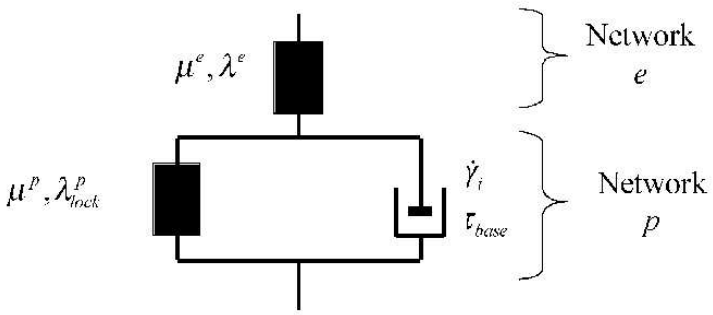

Figure 9.4: Rheological representation of the Arruda–Boyce model

Using the decomposition of the deformation gradient (9.1) the Cauchy stress is calculated from the linear elastic relationship:

$$\mathbf{T} = \frac{1}{J^e}(2\mu^e \mathbf{E}^e + \lambda^e \mathrm{tr}\,[\mathbf{E}^e]\mathbf{I}) \tag{9.23}$$

where $\mathbf{E}^e = \ln[\mathbf{V}^e]$ is the logarithmic true strain, $J^e = \det[\mathbf{F}^e]$, and μ^e and λ^e are Lamé constants. The stress driving the plastic flow is given by the tensorial difference between the total stress and the convected back stress

$$\mathbf{T}^* = \mathbf{T} - \frac{1}{J^e}\mathbf{F}^e \mathbf{T}^p \mathbf{F}^{eT} \tag{9.24}$$

where the deviatoric back stress is given by the incompressible 8-chain model which can be written

$$\mathbf{T}^p = \frac{\mu^p}{\bar{\lambda}^p} \frac{L^{-1}\left(\dfrac{\bar{\lambda}^p}{\lambda^p_{lock}}\right)}{L^{-1}\left(\dfrac{1}{\lambda^p_{lock}}\right)} \mathrm{dev}[\mathbf{B}^p] \tag{9.25}$$

with μ^p and λ^p_{lock} being physically motivated material constants, $\mathbf{B}^p = \mathbf{F}_p\mathbf{F}_p^T$, $\bar{\lambda}^p = \sqrt{\mathrm{tr}\,[\mathbf{B}^p]/3}$ is the effective chain stretch based on the eight-chain topology assumption, and $L(x) = \coth(x) - 1/x$ is the Langevin function.

In the original work the [37, 38] the plastic flow rate was given by

$$\dot{\gamma}^p = \dot{\gamma}_0 \exp\left[\frac{-As}{k_B\theta}\left(1 - \left(\frac{\tau}{s}\right)^{5/6}\right)\right] \tag{9.26}$$

where $\dot{\gamma}_0$, A_0, s are material constants, k_B is the Boltzmann's constant, and θ is the absolute temperature. Taking the stress ecponent to be 1 instead of 5/6 and grouping material constants together we obtain the expression for the plastic flow in the form similar to the Eyring equation

$$\dot{\gamma}^p = \dot{\gamma}_0 \exp\left[\frac{\tau - s}{\tau_{base}}\right] = \dot{\gamma}_i \exp\left[\frac{\tau}{\tau_{base}}\right] \tag{9.27}$$

where $\tau_{base} = k_B\theta/A$, and $\dot{\gamma}_i = \dot{\gamma}_0 \exp -s/\tau_{base}$. The scalar equivalent stress is taken as the Froenius norm of the deviatoric part of the driving stress $\tau = \|\mathrm{dev}\,[\mathbf{T}^*]\|_F$, where $\|\mathbf{A}\|_F = (A_{ij}A_{ij})^{1/2}$. The rate of plastic deformation is given by

$$\mathbf{D}_p = \frac{\dot{\gamma}^p}{\tau}\mathrm{dev}\,[\mathbf{T}^*] \tag{9.28}$$

and the plastic spin is taken to be zero, $\mathbf{\Omega}_p = \mathbf{0}$, which uniquely specifies the rate kinematics.

The AB model also allows for modeling of strain softening through an evolution equation of the athermal shear resistance s.

9.5 The Bergström–Boyce (BB) Model

The Bergström–Boyce model was developed [39] for predicting time-dependence and hystheresis of crosslinked polymers above the glass transition temperature, ie. elastomeric materials.

The basic idea in the BB model is that the material response is governed by two interacting networks: one network gives the equilibrium response and the second network provides the independent deviation from the equilibrium state. The rheological representation of the BB model is shown in Fig. 9.5. The spring element of network A is modeled with 8-chain model, the spring element of network B is modeled with a neo-Hookean hyperelasticity model, and the time-dependent element is modeled with a reptation motivated representation.

In the constitutive framework the total deformation gradient $\mathbf{F}$acts both on the equilibrium network A and on the time dependent network B, ie. $\mathbf{F} = \mathbf{F}_A = \mathbf{F}_B$.

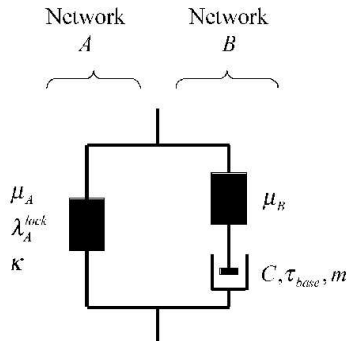

Figure 9.5: Rheological representation of the Bergström–Boyce model

The deformation gradient tensor $\mathbf{F}$ is decomposed into distortional (isochoric) and dilatation (volumetric) parts:

$$\mathbf{F} + J^{1/3}\mathbf{F}^* \tag{9.29}$$

where $J = \det(\mathbf{F})$. The Cauchy stress acting on network A can be obtained from the eight-chain model:

$$J\mathbf{T}^A = \frac{\mu_A}{\bar{\lambda}^*}\frac{L^{-1}\left(\frac{\bar{\lambda}^*}{\lambda_A^{lock}}\right)}{L^{-1}\left(\frac{1}{\lambda_A^{lock}}\right)}\text{dev}[\mathbf{B}^*] + K[\ln J]\mathbf{I} \tag{9.30}$$

where μ_A is the initial shear modulus, λ_A^{lock} the limiting chain stretch, K the bulk modulus, $\mathbf{B}^* = J^{-2/3}\mathbf{F}\mathbf{F}^T$, and $\bar{\lambda}^* = \sqrt{\text{tr}\,[\mathbf{B}^*]/3}$ is the effective chain stretch based on the eight-chain topology assumption.

The deformation gradient on network B is decomposed into elastic and viscous parts

$$\mathbf{F}_B = \mathbf{F}_B^e\mathbf{F}_B^p \tag{9.31}$$

The deviatoric part of the Cauchy stress acting on network B is obtained from the neo-Hookean hyperelasticity model:

$$\mathbf{T}'_B = \mu_B\text{dev}\,[\mathbf{B}_B^e] \tag{9.32}$$

where μ_B is the shear modulus,

$$\mathbf{B}_B^e = (J_B^e)^{-2/3}\mathbf{F}_B^e{\mathbf{F}_B^e}^T, \qquad J_B^e = \det(\mathbf{F}_B^e) \tag{9.33}$$

In the proposed framwork the total stress in the system is given by $\mathbf{T}_A + \mathbf{T}_B$.

9.6 Compressible Leonov model

9.6.1 Introduction

In this section the single mode compressible Leonov model — simplification of the generalised compressible Leonov model developed by Tervoort [6, 40] is presented.

The rheological schematic model of the is shown in Fig. 8.11. It can be looked upon as a number of Maxwell models in parallel, each consisting of a linear spring and non-linear dashpot in series. Tervoort separated the elastic hydrostatic stress and the visco-elastic deviatoric stress in each Maxwell element and named such an element a single "Leonov mode". Plastic flow of polymers was described by Tervoort using non-Newtonian viscous flow rule with the viscosity calculated from a generalised Eyring equation, cf. Sec. 8.7. Strain hardening was modelled by a hardening spring parallel to the Leonov modes (Fig. 8.11).

The multi-mode Leonov model requires many parameters depending on the number of Leonov modes used — the polycarbonate model [6] comprises eighteen modes to describe the glass transition spectrum and a single spring to capture the strain hardening behaviour.

If one is interested in rate dependent yield behaviour, a useful approximation is the single mode compressible Leonov model presented schematically in Fig. 9.6. The single Leonov mode describes rate-dependent yield behaviour and the spring represents the strain hardening response. The single-mode compressible Leonov model has been successfully applied to modelling of polymer behaviour in forming processes of polymer coated sheet [12].

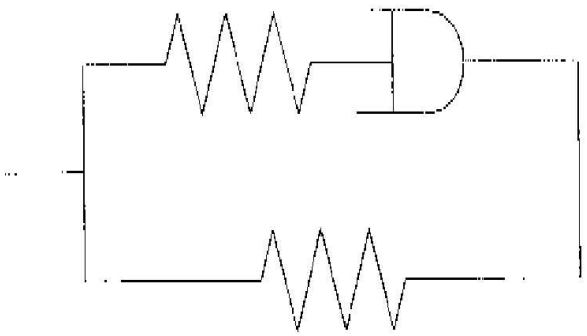

Figure 9.6: Rheological schematic model of the single-mode compressible Leonov model

In accordance with the rheological scheme of the model presented in Fig. 9.6 the Cauchy stress is additively decomposed in the driving stress $\mathbf{s}$ and the hardening stress $\mathbf{w}$

$$\boldsymbol{\sigma} = \mathbf{s} + \mathbf{w} \tag{9.34}$$

9.6.2 Elastic behaviour

Large inelastic deformations are described using the multiplicative decomposition of the deformation gradient tensor $\mathbf{F}$ into elastic $\mathbf{F}_e$ and inelastic $\mathbf{F}_p$ parts defined by Eq. (9.1) and decoupling of the elastic deformation into volume preserving (isochoric) $\bar{\mathbf{F}}_e$ and volumetric $\mathbf{F}_e^v$ denoted by Eq. (9.4).

Separation of volumetric and isochoric deformations is introduced into the free energy function Ψ

$$\Psi = \Psi^v + \Psi^{iso} \tag{9.35}$$

The free energy is assumed to be a function of the invariants of the left Cauchy–Green tensor for the isochoric deformation $\bar{\mathbf{B}}_e$ and the volume deformation factor J

$$\Psi = \Psi(J, I_{\bar{\mathbf{B}}_e}, II_{\bar{\mathbf{B}}_e}) = \Psi^v(J) + \Psi^{iso}(I_{\bar{\mathbf{B}}_e}, II_{\bar{\mathbf{B}}_e}) \tag{9.36}$$

where

$$J = \det \mathbf{F} \tag{9.37}$$

Decoupling of the free energy function (9.36) leads to the decomposition of the driving stress $\mathbf{s}$ into the hydrostatic part $\mathbf{s}^v$ and the deviatoric part $\mathbf{s}^d$:

$$\mathbf{s} = \mathbf{s}^v + \mathbf{s}^d \tag{9.38}$$

where, cf. [6]:

$$\mathbf{s}^v = J\frac{\partial \Psi^v}{\partial J}\mathbf{I}\,, \qquad \mathbf{s}^d = 2\bar{\alpha}_1 \bar{\mathbf{B}}_e^d + 2\bar{\alpha}_2 \mathrm{tr}\,(\bar{\mathbf{B}}_e)\bar{\mathbf{B}}_e^d + 2\bar{\alpha}_2(\bar{\mathbf{B}}_e \cdot \bar{\mathbf{B}}_e)^d \tag{9.39}$$

where $\bar{\alpha}_i, i = 1, 2$ are the derivatives of the free energy with respect to invariants of $\bar{\mathbf{B}}_e$.

The strains must be updated by integration of appropriate evolution laws for $\bar{\mathbf{B}}_e$ and J. For J we have

$$\dot{J} = J\,\mathrm{tr}\,\mathbf{D} \tag{9.40}$$

The evolution law for $\bar{\mathbf{B}}_e$ must be objective with respect to rigid material rotations, which implies necessity of using an objective derivative. Originally in [6] the Jaumann derivative has been used

$$\mathring{\bar{\mathbf{B}}}_e = (\mathbf{D}^d - \mathbf{D}_p) \cdot \bar{\mathbf{B}}_e - \bar{\mathbf{B}}_e \cdot (\mathbf{D}^d - \mathbf{D}_p) \tag{9.41}$$

where $\mathring{\bar{\mathbf{B}}}_e$ is the Jaumann derivative of $\bar{\mathbf{B}}_e$, $\mathbf{D}$ is the symmetric part of $\mathbf{L}$ and $\mathbf{D}_p$ is the plastic deformation rate tensor (deviatoric).

9.6.3 Plastic flow

In the evolution law for $\bar{\mathbf{B}}_e$ (9.41) the decomposition of deformation rate tensor $\mathbf{D}$ into elastic and plastic parts $(9.10)_1$ is employed. It is assumed in the model [6, 11] that for polymers, plastic flow occurs at constant volume, described by a non-Newtonian visocus flow rule

$$\mathbf{D}_p = \frac{1}{2\eta}\mathbf{s}^d \tag{9.42}$$

where $\mathbf{s}^d$ is the deviatoric driving stress tensor and η is a variable viscosity.

An expression for the viscosity can be formulated starting from the generalised Eyring equation as follows, cf. [6], Sec. 8.7:

$$\eta = \eta(\mathbf{s}^d, T) = A\tau_0 \frac{(\tau_{eq}/\tau_0)}{\sinh(\tau_{eq}/\tau_0)} = \eta_0 a_\sigma(\tau_{eq}) \tag{9.43}$$

where A is a time constant, τ_0 is characteristic stress, a_σ is the so-called shift function, $\eta_0 = A\tau_0$ is the zero-shear viscosity, and τ_{eq} is the equivalent stress

$$\tau_{eq} = \sqrt{\mathbf{s}^d : \mathbf{s}^d} \tag{9.44}$$

Material constants A and τ_0 are given by

$$A = A_0 \exp\left(\frac{\Delta H}{RT}\right), \qquad \tau_0 = \frac{RT}{V} \tag{9.45}$$

where A_0 is a material constant involving the fundamental vibration frequency, ΔH — the activation energy, R — the universal gas constant, T — the absolute temperature, and V — the shear activation volume.

The Eyring approach implies that deformation mechanisms of yielding are essentially always present with the stress changing the rate of deformation. This is clearly expressed by the functional dependence of the Eyring viscosity on stress expressed by Eq. (9.43). There is a linear region at low stress ($\tau_{eq} \ll \tau_0$), where the viscosity is equal to the zero-shear viscosity $\eta_0 = A\tau_0$ and all the non-linear effects are incorporated into the shift function a_σ. According to the Eyring equation, deformation process are accelerated by stress.

On a fitting level, the Eyring equation is almost indistinguishable from the Argon equation [41] used in the BPA-model [21]. There are however conceptual differences. The Argon theory regards yielding as a nucleation-controlled process.

The Eyring equation can be augmented in a straightforward way to allow for pressure dependence and intrinsic softening effects. To account for pressure Ward [7] modified the activation energy based upon an experimentally observed linear increase of the activation energy with increasing pressure. The time constant A in Eq. (9.45) is then given by

$$A = A_0 \exp\left[\frac{\Delta H + p\Omega}{RT}\right] = A_0 \exp\left[\frac{\Delta H}{RT} + \frac{\mu p}{\tau_0}\right] \tag{9.46}$$

where p is the hydrostatic component of stress, Ω is the pressure activation volume, and $\mu = \Omega/V$ is a material parameter describing the pressure dependence.

Hasan et al. [42] included intrinsic softening including a parameter D into the time constant A

$$A = A_0 \exp\left[\frac{\Delta H}{RT} + \frac{\mu p}{\tau_0} - D\right] \tag{9.47}$$

The current value of the softening variable D is determined from the evolution equation

$$\dot{D} = h\left(1 - \frac{D}{D_\infty}\right)\dot{\gamma}_p \tag{9.48}$$

with initial condition $D = 0$, h being the softening slope, D_∞ the saturation value of D, and $\dot{\gamma}_p$ the equivalent plastic strain rate

$$\dot{\gamma}_p = \sqrt{\mathbf{D}_p : \mathbf{D}_p} = \frac{\sqrt{\mathbf{s}^d : \mathbf{s}^d}}{2\eta} = \frac{\tau_{eq}}{2\eta} \tag{9.49}$$

During elastic deformation D is constant — material state does not change. During plastic deformation D evolves to a saturation value D_∞.

9.6.4 Strain hardening

The hardening stress is calculated in [6, 11] according to the neo-Hookean relation

$$\mathbf{s}^d = H\bar{\mathbf{B}}^d \tag{9.50}$$

where H is the hardening modulus (assumed temperature dependent). Contrary to [21] the hardening stress is not related to the plastic deformation but to the total deformation. This is explained by the assumption in the model presented both elastic and plastic deformations are assumed to decrease the configurational entropy of the polymer. In case of small elastic deformations these approaches are nearly identical.

9.6.5 Simplified model

If small volume changes can be assumed ($J \approx 1$) the hydrostatic stress term $\mathbf{s}^v$ in Eq. $(9.39)_1$ can be written as

$$\mathbf{s}^v = K(J-1)\mathbf{I} \tag{9.51}$$

where K is the bulk modulus and $\mathbf{I}$ is the unit tensor. Further simplification can be made by choosing $\bar{\alpha}_2 = 0$ in Eq. $(9.39)_2$ (this means assumption of a linear dependence of $\mathbf{s}^d$ on $\bar{\mathbf{B}}_e$). The identifying $2\bar{\alpha}_1$ to the shear modulus G, the deviatoric part of the driving stress is given by

$$\mathbf{s}^d = G\bar{\mathbf{B}}_e^d \tag{9.52}$$

9.7 Generalised viscoelastic/elastoplastic model

9.7.1 Introduction

The model developed by M. Luege [43] is extension of the general viscoplastic model [16] to finite deformations. In fact it combines viscoelasticity and elastoplasticity. The model takes into account such important features of polymers like nolinear elastic stress–strain relationship, plastic deformation and viscous effects. It is assumed it can represent the PET deformation behaviour under isothermal conditions.

9.7.2 Basic assumptions

The rheological schematic model of viscoelasticty combined with elastoplasticity is shown in Fig. 9.7. The developed elastoviscoplastic model is based on the following

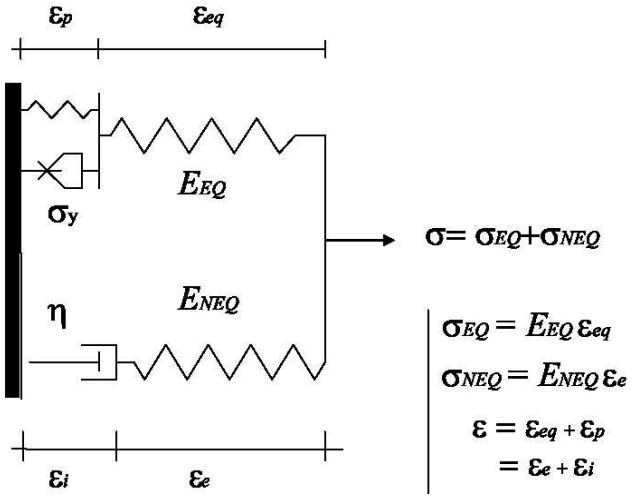

Figure 9.7: Rheological model of combined viscoelasticity and elastoplasticity

assumptions:

- Multiplicative decomposition of the deformation gradient tensor $\mathbf{F}$ into a plastic parts $\mathbf{F}_p$ and elastic equilibrium part $\mathbf{F}_{eq}$

$$\mathbf{F} = \mathbf{F}_{eq}\mathbf{F}_p \tag{9.53}$$

  At the same time the non-equilibrium viscous deformation mechanism is assumed so that we have another multiplicative decomposition of the deformation gradient tensor into the viscous part $\mathbf{F}_i$ and the elastic non-equilibrium part $\mathbf{F}_e$

$$\mathbf{F} = \mathbf{F}_e\mathbf{F}_i \tag{9.54}$$

- Additive decomposition of the Helmholtz free energy Ψ into the elastic and plastic parts, Ψ^e and Ψ^p, respectively

$$\Psi(\mathbf{C}, \mathbf{F}_i, \mathbf{F}_p, \alpha) = \Psi^e(\mathbf{C}, \mathbf{F}_i, \mathbf{F}_p) + \Psi^p(\alpha) \tag{9.55}$$

  where $\mathbf{C} = \mathbf{F}^T\mathbf{F}$ is the right Cauchy–Green tensor and α is the equivalent plastic deformation

- Additive decomposition of the Helmholtz elastic free energy Ψ^e into the equilibrium and non-equilibrium parts, Ψ_{EQ} and Ψ_{NEQ}, respectively

$$\Psi(\mathbf{C}, \mathbf{F}_i, \mathbf{F}_p) = \Psi_{EQ}(\mathbf{C}_{eq}(\mathbf{C}, \mathbf{F}_p)) + \Psi_{NEQ}(\mathbf{C}_e(\mathbf{C}, \mathbf{F}_i)) \tag{9.56}$$

  where respective right Cauchy–Green tensors are defined as follows

$$\mathbf{C}_{eq} = \mathbf{F}_{eq}^T\mathbf{F}_{eq} = \mathbf{F}_p^{-T}\mathbf{C}\mathbf{F}_p^{-1}\,, \qquad \mathbf{C}_e = \mathbf{F}_e^T\mathbf{F}_e = \mathbf{F}_i^{-T}\mathbf{C}\mathbf{F}_i^{-1} \tag{9.57}$$

The constitutive model thermodynamically admissible must satisfy the equation of the internal energy dissipation

$$\mathcal{D}_{int} = \mathbf{S} : \tfrac{1}{2}\dot{\mathbf{C}} - \dot{\Psi} \geq 0 \tag{9.58}$$

where $\mathbf{S}$ is the second Piola–Kirchhoff stress tensor, $\mathbf{C} = \mathbf{F}^T\mathbf{F}$ is the right Cauchy–Green deformation tensor, $\mathbf{F}$ is the deformation gradient tensor and Ψ is the free Helmholtz energy per unit volume in the reference configuration.

Taking into account relationships (9.53)–(9.57) and (9.58) the following relationships can be obtained

$$\mathbf{S} = 2\frac{\partial \Psi^e}{\partial \mathbf{C}}\,, \qquad R = \frac{\partial \Psi^p}{\partial \alpha} \tag{9.59}$$

$$\mathcal{D}_{int} = \frac{\partial \Psi_{EQ}}{\partial \mathbf{C}_{eq}} : (\mathbf{l}_p^T\mathbf{C}_{eq} + \mathbf{C}_{eq}\mathbf{l}_p) + \frac{\partial \Psi_{NEQ}}{\partial \mathbf{C}_e} : (\mathbf{l}_i^T\mathbf{C}_e + \mathbf{C}_e\mathbf{l}_i) - R : \dot{\alpha} \geq 0 \tag{9.60}$$

where R is the thermodynamic force associated with the internal parameter α, and $\mathbf{l}_p = \dot{\mathbf{F}}_p\mathbf{F}_p^{-1}$ and $\mathbf{l}_i = \dot{\mathbf{F}}_i\mathbf{F}_i^{-1}$ are the plastic and viscous deformation velocity gradients, respectively.

Detailed derivation of anterior equations is presented below. First deriving the free energy function Ψ given by Eq. (9.55) with respect to time we obtain

$$\dot{\Psi} = \dot{\Psi}^e + \dot{\Psi}^p \tag{9.61}$$

where

$$\begin{aligned} \dot{\Psi}^e \;=\; & \frac{\partial \Psi_{EQ}}{\partial \mathbf{C}_{eq}} : \frac{\partial \mathbf{C}_{eq}}{\partial \mathbf{C}} : \dot{\mathbf{C}} + \frac{\partial \Psi_{NEQ}}{\partial \mathbf{C}_e} : \frac{\partial \mathbf{C}_e}{\partial \mathbf{C}} : \dot{\mathbf{C}} + \\ & \frac{\partial \Psi_{EQ}}{\partial \mathbf{C}_{eq}} : \frac{\partial \mathbf{C}_{eq}}{\partial \mathbf{F}_p} : \dot{\mathbf{F}}_p + \frac{\partial \Psi_{NEQ}}{\partial \mathbf{C}_e} : \frac{\partial \mathbf{C}_e}{\partial \mathbf{F}_i} : \dot{\mathbf{F}}_i \end{aligned} \tag{9.62}$$

$$\dot{\Psi}^p = \frac{\partial \Psi^p}{\partial \alpha} : \dot{\alpha} \tag{9.63}$$

From Eq. $(9.57)_1$ we have

$$\begin{aligned} \frac{\partial \mathbf{C}_{eq}}{\partial \mathbf{F}_p} : \dot{\mathbf{F}}_p &= \dot{\overline{\mathbf{F}_p^{-T}}}\mathbf{C}\mathbf{F}_p^{-1} + \mathbf{F}_p^{-T}\mathbf{C}\dot{\overline{\mathbf{F}_p^{-1}}} \\ &= -\mathbf{l}_p^T\mathbf{F}_p^{-T}\mathbf{C}\mathbf{F}_p^{-1} - \mathbf{F}_p^{-T}\mathbf{C}\mathbf{F}_p^{-1}\mathbf{l}_p \\ &= -\mathbf{l}_p^T\mathbf{C}_{eq} - \mathbf{C}_{eq}\mathbf{l}_p \end{aligned} \tag{9.64}$$

where we take into account that with $\dfrac{d}{dt}(\mathbf{F}_p^T\mathbf{F}_p^{-T}) = \mathbf{0}$ the following relationships are satisfied

$$\dot{\mathbf{F}}_p^T\mathbf{F}_p^{-T} = \mathbf{0} + \mathbf{F}_p^T\dot{\overline{\mathbf{F}_p^{-T}}} = \mathbf{0} \tag{9.65}$$

$$\mathbf{l}_p^T = -\dot{\overline{\mathbf{F}_p^{-T}}}\mathbf{F}_p^T \tag{9.66}$$

Analogically from Eq. $(9.57)_2$ we obtain

$$\frac{\partial \mathbf{C}_e}{\partial \mathbf{F}_i} : \dot{\mathbf{F}}_i = -\mathbf{l}_i^T\mathbf{C}_e - \mathbf{C}_e\mathbf{l}_i \tag{9.67}$$

with $\mathbf{l}_i = \dot{\mathbf{F}}_i\mathbf{F}_i^{-1}$ and $\mathbf{l}_i^T = -\dot{\overline{\mathbf{F}_i^{-T}}}\mathbf{F}_i^T$. Finally we

$$\frac{\partial \Psi_{EQ}}{\partial \mathbf{C}_e} : \frac{\partial \mathbf{C}_e}{\partial \mathbf{C}} : \dot{\mathbf{C}} = \frac{\partial \Psi_{EQ}}{\partial \mathbf{C}} : \dot{\mathbf{C}} \tag{9.68}$$

$$\frac{\partial \Psi_{NEQ}}{\partial \mathbf{C}_{eq}} : \frac{\partial \mathbf{C}_{eq}}{\partial \mathbf{C}} : \dot{\mathbf{C}} = \frac{\partial \Psi_{NEQ}}{\partial \mathbf{C}} : \dot{\mathbf{C}} \tag{9.69}$$

Substituting relationships (9.61)–(9.64) and (9.67)–(9.69) into Eq. (9.58) we obtain

$$\begin{aligned} \mathcal{D}_{int} &= \left(\mathbf{S} - 2\frac{\partial \Psi^e}{\partial \mathbf{C}}\right) : \tfrac{1}{2}\dot{\mathbf{C}} + \frac{\partial \Psi_{NEQ}}{\partial \mathbf{C}_{eq}} : (\mathbf{l}_p^T\mathbf{C}_{eq} + \mathbf{C}_{eq}\mathbf{l}_p) \\ &\quad + \frac{\partial \Psi_{NEQ}}{\partial \mathbf{C}_e} : (\mathbf{l}_i^T\mathbf{C}_{eq} + \mathbf{C}_e\mathbf{l}_i) - \frac{\partial \Psi^p}{\partial \alpha} : \dot{\alpha} \geq 0 \end{aligned} \tag{9.70}$$

From Eq. (9.70) it results immediately the following

$$\mathbf{S} = 2\frac{\partial \Psi^e}{\partial \mathbf{C}}, \qquad R = \frac{\partial \Psi^p}{\partial \alpha} \tag{9.71}$$

$$\mathcal{D}_{int} = \frac{\partial \Psi_{EQ}}{\partial \mathbf{C}_{eq}} : (\mathbf{l}_p^T\mathbf{C}_{eq} + \mathbf{C}_{eq}\mathbf{l}_p) + \frac{\partial \Psi_{NEQ}}{\partial \mathbf{C}_e} : (\mathbf{l}_i^T\mathbf{C}_e + \mathbf{C}_e\mathbf{l}_i) - R : \dot{\alpha} \geq 0 \tag{9.72}$$

where R is the thermodynamic force associated with the internal parameter α.

For the elastic free energy given by Eq. (9.56) Eq. (9.71) is written as follows

$$\mathbf{S} = \underbrace{2\frac{\partial \Psi_{EQ}}{\partial \mathbf{C}}}_{\mathbf{S}_{EQ}} + \underbrace{2\frac{\partial \Psi_{NEQ}}{\partial \mathbf{C}}}_{\mathbf{S}_{NEQ}} = 2\frac{\partial \Psi_{EQ}}{\partial \mathbf{C}_{eq}} : \frac{\partial \mathbf{C}_{eq}}{\partial \mathbf{C}} + 2\frac{\partial \Psi_{NEQ}}{\partial \mathbf{C}_e} : \frac{\partial \mathbf{C}_e}{\partial \mathbf{C}} \tag{9.73}$$

The Cauchy stress tensor is given by

$$\boldsymbol{\sigma} := J^{-1}\mathbf{F}\mathbf{S}\mathbf{F}^T = 2J^{-1}\mathbf{F}\frac{\partial \Psi^e}{\partial \mathbf{C}}\mathbf{F}^T = 2J^{-1}\mathbf{B}\frac{\partial \Psi^e}{\partial \mathbf{B}} \tag{9.74}$$

where $\mathbf{B} := \mathbf{F}\mathbf{F}^T$ is the left Cauchy–Green tensor. Developing Eq. (9.74) in terms of the equilibrium and non-equilibrium parts we have

$$\begin{aligned}
\boldsymbol{\sigma} &= 2J^{-1}\left[\mathbf{F}_{eq}\frac{\partial \Psi_{EQ}}{\partial \mathbf{C}_{eq}}\mathbf{F}_{eq}^T + \mathbf{F}_e\frac{\partial \Psi_{NEQ}}{\partial \mathbf{C}_e}\mathbf{F}_e^T\right] \\
&= J^{-1}\left[\mathbf{F}_{eq}\left(\frac{\partial \Psi_{EQ}}{\partial \mathbf{F}_{eq}}\right)^T + \mathbf{F}_e\left(\frac{\partial \Psi_{NEQ}}{\partial \mathbf{F}_e}\right)^T\right] \\
&= \underbrace{2J^{-1}\mathbf{B}_{eq}\frac{\partial \Psi_{EQ}}{\partial \mathbf{B}_{eq}}}_{\boldsymbol{\sigma}_{EQ}} + \underbrace{2J^{-1}\mathbf{B}_e\frac{\partial \Psi_{NEQ}}{\partial \mathbf{B}_e}}_{\boldsymbol{\sigma}_{NEQ}} = \boldsymbol{\sigma}_{EQ} + \boldsymbol{\sigma}_{NEQ}
\end{aligned} \tag{9.75}$$

where the respective tensors of deformation $\mathbf{B}_{eq}$ and $\mathbf{B}_e$ are defined as

$$\mathbf{B}_{eq} := \mathbf{F}_{eq}\mathbf{F}_{eq}^T \qquad \mathbf{B}_e := \mathbf{F}_e\mathbf{F}_e^T \tag{9.76}$$

The respective Kirchhoff stress tensors are given by

$$\boldsymbol{\tau}_{EQ} := 2\mathbf{F}_{eq}\frac{\partial \Psi_{EQ}}{\partial \mathbf{C}_{eq}}\mathbf{F}_{eq}^T, \qquad \boldsymbol{\tau}_{NEQ} := 2\mathbf{F}_e\frac{\partial \Psi_{NEQ}}{\partial \mathbf{C}_e}\mathbf{F}_e^T \tag{9.77}$$

where it is shown that

$$\boldsymbol{\tau}_{EQ} = J\boldsymbol{\sigma}_{EQ}, \qquad \boldsymbol{\tau}_{NEQ} = J\boldsymbol{\sigma}_{NEQ} \tag{9.78}$$

9.7.3 Free energy for elastic deformation

In the present section the forms of the free energy for elastic deformation are considerd. Elastic deformation can be described using a suitable model of nonlinear elasticity. Here the Ogden model for incompressible and quasi-incompressible material is considered. First the formulation of the free energy for elastic materials is presented and then its implementation in the viscoelastic-viscoplastic model is presented.

Nonlinear elasticity for incompressible materials

If we consider the incompressible material, that is with the restriction

$$J = \lambda_1 \lambda_2 \lambda_3 = 1 \tag{9.79}$$

we can use the function of the free energy postulated by Ogden, cf. [**?**] given in terms of the principal stretches λ_A, $A = 1, 2, 3$

$$\Psi = \Psi(\lambda_1, \lambda_2, \lambda_3) = \sum_{p=1}^{N} \frac{\mu_p}{\alpha_p} \left(\lambda_1^{\alpha_p} + \lambda_2^{\alpha_p} + \lambda_3^{\alpha_p} - 3 \right) \tag{9.80}$$

In order to have a consistency with the linear (small deformation) theory the following condition is imposed, cf. [**?**]:

$$2\mu_m = \sum_{p=1}^{N} \mu_p \alpha_p \quad \text{with} \quad \mu_p \alpha_p > 0, p = 1, \ldots, N \tag{9.81}$$

where μ_m is the classical shear modulus.

Nonlinear elasticity for quasi-incompressible materials

For elastic materials with small compressibility the free energy Ψ can be decomposed into the volumetric and isochoric parts, Ψ^v and Ψ^{iso}, respectively

$$\Psi(\mathbf{B}) = \Psi^{iso}(\bar{\mathbf{B}}) + \Psi^v(J) \tag{9.82}$$

The tensor $\bar{\mathbf{B}}$ is the left Cauchy–Green tensor for the distorsional (preserving volumen) deformation. It can be deduced from the multiplicative decomposition of the deformation gradient $\mathbf{F}$ into the distortional and volumetric parts, $\bar{\mathbf{F}}$ and $J^{1/3}\mathbf{I}$, respectively

$$\mathbf{F} = J^{1/3}\mathbf{I}\bar{\mathbf{F}} \tag{9.83}$$

Introducing the above decomposition into the definition of the left Cauchy–Green tensor gives

$$\mathbf{B} = \mathbf{F}\mathbf{F}^T = J^{2/3}\bar{\mathbf{F}}\bar{\mathbf{F}}^T = J^{2/3}\bar{\mathbf{B}} \tag{9.84}$$

where $\bar{\mathbf{B}} = \bar{\mathbf{F}}\bar{\mathbf{F}}^T$.

For the isochoric part of the free energy the Ogden equation (9.80) can be used in terms of the principal stretches of the isochoric part of the deformation $\bar{\lambda}_A$, eigenvalues of the tensor $\bar{\mathbf{F}}$. Then Eq. (9.82 takes the form:

$$\Psi(\lambda_1, \lambda_2, \lambda_3) = \Psi^{iso}(\bar{\lambda}_1, \bar{\lambda}_2, \bar{\lambda}_3) + \Psi^v(J) \tag{9.85}$$

where the volumetric and deviatoric components are defined as

$$\Psi^{iso}(\bar{\lambda}_1, \bar{\lambda}_2, \bar{\lambda}_3) = \sum_{p=1}^{N} \frac{\mu_p}{\alpha_p} \left(\bar{\lambda}_1^{\alpha_p} + \bar{\lambda}_2^{\alpha_p} + \bar{\lambda}_3^{\alpha_p} - 3 \right) \tag{9.86}$$

$$\Psi^{v}(J) = \tfrac{1}{2} K (J-1)^2 \tag{9.87}$$

The Cauchy stress tensor is given now by:

$$\boldsymbol{\sigma} = 2J^{-1}\mathbf{B}\frac{\partial \Psi^e}{\partial \mathbf{B}} = 2J^{-1}\mathbf{B}\frac{\partial \Psi^{iso}}{\partial \mathbf{B}} + 2J^{-1}\mathbf{B}\frac{\partial \Psi^{v}}{\partial \mathbf{B}} \tag{9.88}$$

Considering the following decomposition

$$\boldsymbol{\sigma} = \mathrm{dev}\boldsymbol{\sigma} + p\mathbf{I}\,, \qquad \text{with} \quad p = \tfrac{1}{3}\mathrm{tr}[\boldsymbol{\sigma}] \tag{9.89}$$

it can be easily demonstrated that

$$\mathrm{dev}\boldsymbol{\sigma} = 2J^{-1}\mathbf{B}\frac{\partial \Psi^{iso}}{\partial \mathbf{B}}\,, \qquad p = \frac{\partial \Psi^{v}}{\partial \mathbf{B}} \tag{9.90}$$

9.7.4 Free elastic energy for the viscoelastic/elastoviscoplastic model

For the viscoelastic/elastoviscoplastic model it is assumed that the free elastic energy Ψ^e is composed of the isochoric and volumetric parts, Ψ^{iso} and Ψ^{v}, respectively

$$\Psi^e = \Psi^{iso} + \Psi^{v} \tag{9.91}$$

The volumetric part is assumed in the following form

$$\Psi^{v}(J) = \tfrac{1}{2} K (J-1)^2$$

The isochoric part is assumed to be composed of the equilibrium and non-equilibrium parts, Ψ^{iso}_{EQ} and Ψ^{iso}_{NEQ}, respectively

$$\Psi^{iso} = \Psi^{iso}_{EQ}(\bar{\lambda}_{eq1}, \bar{\lambda}_{eq2}, \bar{\lambda}_{eq3}) + \Psi^{iso}_{NEQ}(\bar{\lambda}_{e1}, \bar{\lambda}_{e2}, \bar{\lambda}_{e3})$$

where the equilibrium and non-equilibrium parts are taken in the form proposed by Ogden

$$\Psi^{iso} = \sum_{p=1}^{N} \frac{\mu_p}{\alpha_p} \left(\sum_{A=1}^{3} \bar{\lambda}_{eqA}^{\alpha_p} - 3 \right) + \sum_{p=1}^{N} \frac{\mu_{vp}}{\alpha_{vp}} \left(\sum_{A=1}^{3} \bar{\lambda}_{eA}^{\alpha_{vp}} - 3 \right)$$

where $\bar{\lambda}_{eA}$ and $\bar{\lambda}_{eqA}$ are respective eigenvalues of the tensors $\bar{\mathbf{B}}_e$ and $\bar{\mathbf{B}}_{eq}$, defined analogically to Eq. (9.84)

$$\bar{\mathbf{B}}_{eq} = J^{-2/3}\mathbf{B}_{eq}\,, \qquad \bar{\mathbf{B}}_{e} = J^{-2/3}\mathbf{B}_{e} \tag{9.92}$$

From Eq. (9.74) the Cauchy stress tensor for the model developed is obtained as

$$\begin{aligned}
\boldsymbol{\sigma} &= 2J^{-1}\mathbf{B}\frac{\partial \Psi^e}{\partial \mathbf{B}} = 2J^{-1}\mathbf{B}\frac{\partial \Psi^{iso}}{\partial \mathbf{B}} + 2J^{-1}\mathbf{B}\frac{\partial \Psi^v}{\partial \mathbf{B}} \\
&= \underbrace{2J^{-1}\mathbf{B}_{eq}\frac{\partial \Psi^{iso}_{EQ}}{\partial \bar{\mathbf{B}}_{eq}} : \frac{\partial \bar{\mathbf{B}}_{eq}}{\partial \mathbf{B}_{eq}}}_{\mathrm{dev}\boldsymbol{\sigma}_{EQ}} + \underbrace{2J^{-1}\mathbf{B}_{e}\frac{\partial \Psi^{iso}_{NEQ}}{\partial \bar{\mathbf{B}}_{e}} : \frac{\partial \bar{\mathbf{B}}_{e}}{\partial \mathbf{B}_{e}}}_{\mathrm{dev}\boldsymbol{\sigma}_{NEQ}} + \underbrace{K(J-1)\mathbf{I}}_{\boldsymbol{\sigma}^v} \\
&= \mathrm{dev}\boldsymbol{\sigma}_{EQ} + \mathrm{dev}\boldsymbol{\sigma}_{NEQ} + \boldsymbol{\sigma}^v \\
&= J^{-1}(\mathrm{dev}\boldsymbol{\tau}_{EQ} + \mathrm{dev}\boldsymbol{\tau}_{NEQ}) + \boldsymbol{\sigma}^v \\
&= J^{-1}\mathrm{dev}\boldsymbol{\tau} + \boldsymbol{\sigma}^v
\end{aligned} \tag{9.93}$$

9.7.5 Evolution of the internal variable

The evolution law for the internal variable should be assumed in the form satisfying the the dissipation inequality (9.72). It is convenient to transform the dissipation inequality (9.72) into the following form:

$$\mathcal{D}_{int} = -\mathrm{dev}\boldsymbol{\tau}_{EQ} : \tfrac{1}{2}\mathcal{L}_{\boldsymbol{\chi}}[\mathbf{b}_{eq}]\mathbf{b}_{eq}^{-1} - \mathrm{dev}\boldsymbol{\tau}_{NEQ} : \tfrac{1}{2}\mathcal{L}_{\boldsymbol{\chi}}[\mathbf{b}_{e}]\mathbf{b}_{e}^{-1} - R\dot{\alpha} \geq 0 \tag{9.94}$$

where $\mathcal{L}_{\boldsymbol{\chi}}[\mathbf{a}]$ identifies the Lie derivative of the tensor $\mathbf{a}$. The Lie derivative is defined as

$$\mathcal{L}_{\boldsymbol{\chi}}[\mathbf{a}] := \boldsymbol{\chi}^* \left[\frac{d}{dt}\left(\boldsymbol{\chi}^{*-1}[\mathbf{a}]\right)\right] \tag{9.95}$$

where $\boldsymbol{\chi}^{*-1}[\mathbf{a}] := \mathbf{F}^{-1}\mathbf{a}\mathbf{F}^{-T}$ indicates the pull-back operation of the spatial field to the reference configuration $\boldsymbol{\chi}^*[\mathbf{a}] := \mathbf{F}\mathbf{a}\mathbf{F}^T$ and denotes the push-forward operation of the material field.

Below the transformation of Eq. (9.72) into the form (9.94) is explained following [**?**]. Starting from the equation

$$\mathbf{B}_{eq} = \mathbf{F}_{eq}\mathbf{F}_{eq}^T = \mathbf{F}\mathbf{F}_p^{-1}\mathbf{F}_p^{-T}\mathbf{F}^T \tag{9.96}$$

the temporal derivative of the tensor $\mathbf{B}_{eq}$ is evaluated as follows

$$\begin{aligned}
\dot{\mathbf{B}}_{eq} &= \frac{d}{dt}(\mathbf{F}\mathbf{F}_p^{-1}\mathbf{F}_p^{-T}\mathbf{F}^T) = \frac{d}{dt}(\mathbf{F}\mathbf{C}_p^{-1}\mathbf{F}^T) \\
&= \dot{\mathbf{F}}\mathbf{C}_p^{-1}\mathbf{F}^T + \mathbf{F}\dot{\overline{\mathbf{C}_p^{-1}}}\mathbf{F}^T + \mathbf{F}\mathbf{C}_p^{-1}\dot{\mathbf{F}}^T \\
&= \dot{\mathbf{F}}\mathbf{F}^{-1}\mathbf{F}\mathbf{C}_p^{-1}\mathbf{F}^T + \mathbf{F}\dot{\overline{\mathbf{C}_p^{-1}}}\mathbf{F}^T + \mathbf{F}\mathbf{C}_p^{-1}\mathbf{F}^T\mathbf{F}^{-T}\dot{\mathbf{F}}^T \\
&= \mathbf{l}\mathbf{B}_{eq} + \mathcal{L}_{\boldsymbol{\chi}}[\mathbf{B}_{eq}] + \mathbf{B}_{eq}\mathbf{l}^T
\end{aligned} \tag{9.97}$$

where the Lie time derivative of the tensor $\mathbf{B}_{eq}$ is defined by

$$\mathcal{L}_{\boldsymbol{\chi}}[\mathbf{B}_{eq}] := \mathbf{F}\frac{d}{dt}\left(\mathbf{F}^{-1}\mathbf{B}_{eq}\mathbf{F}^{-T}\right) = \mathbf{F}\dot{\overline{\mathbf{C}_p^{-1}}}\mathbf{F}^T \tag{9.98}$$

Given $\overline{\dot{\mathbf{C}_p^{-1}}} = -\mathbf{F}_p^{-1}(\mathbf{l}_p + \mathbf{l}_p^T)\mathbf{F}_p^{-T}$, we have the Lie derivative

$$\mathcal{L}_{\boldsymbol{\chi}}[\mathbf{B}_{eq}] = -\mathbf{F}_{eq}(\mathbf{l}_p + \mathbf{l}_p^T)\mathbf{F}_{eq}^T \tag{9.99}$$

Analogically using expression for the tensor $\mathbf{B}_e$

$$\mathbf{B}_e = \mathbf{F}_e\mathbf{F}_e^T = \mathbf{F}\mathbf{F}_i^{-1}\mathbf{F}_i^{-T}\mathbf{F}^T = \mathbf{F}\mathbf{C}_i^{-1}\mathbf{F}^T \tag{9.100}$$

we have

$$\dot{\mathbf{B}}_e = \mathbf{l}\mathbf{B}_e + \mathbf{B}_e\mathbf{l}^T + \mathcal{L}_{\boldsymbol{\chi}}[\mathbf{B}_e] \tag{9.101}$$

with

$$\begin{aligned} \dot{\mathbf{B}}_e &= \mathbf{F}\frac{d}{dt}(\mathbf{F}^{-1}\mathbf{B}_e\mathbf{F}^{-T})\mathbf{F}^T = \mathbf{F}\overline{\dot{\mathbf{C}_i^{-1}}}\mathbf{F}^T \\ &= -\mathbf{F}_e(\mathbf{l}_i + \mathbf{l}_i^T)\mathbf{F}_e^T \end{aligned} \tag{9.102}$$

Taking into account Eqs. (9.99) and (9.102), definitions of $\mathrm{dev}\boldsymbol{\tau}_{EQ}$ and $\mathrm{dev}\boldsymbol{\tau}_{NEQ}$ in Eq. (9.93) in Eq. (9.72) we can transform it into the form (9.94).

9.7.6 Dissipative potential

The dissipative potential is assumed in the following form:

$$\Phi = \frac{1}{\eta_D}\mathrm{dev}\boldsymbol{\tau}_{NEQ} : \mathrm{dev}\boldsymbol{\tau}_{NEQ} + \mathcal{I}_E(\boldsymbol{\tau}_{EQ}, R) \tag{9.103}$$

where $\mathcal{I}_E$is the indicator function of the elastic domain E defined as

$$E = \{(\boldsymbol{\tau}_{EQ}, R) : \mathcal{F} \leq 0, R \geq 0\} \tag{9.104}$$

and $\mathcal{F}$is the yield function given by the Huber–Mises criterion

$$\mathcal{F}(\boldsymbol{\tau}_{EQ}, R) = \|\mathrm{dev}\boldsymbol{\tau}_{EQ}\| - \sqrt{\tfrac{2}{3}}\hat{y} \tag{9.105}$$

with

$$\hat{y} = \sigma_y + R \tag{9.106}$$

where σ_y is the initial yield stress and R is the thermodynamic force associated with the internal variable α. The evolution laws are derived from Eq. (9.103), assuming the evolution law for the non-equilibrium elastic part in the form

$$-\tfrac{1}{2}(\mathcal{L}_{\boldsymbol{\chi}}[\mathbf{B}_e])\mathbf{B}_e^{-1} = \frac{\partial\Phi}{\partial\boldsymbol{\tau}_{NEQ}} = \frac{1}{\eta_D}\boldsymbol{\tau}_{NEQ} \tag{9.107}$$

while for the equilibrium elastic part and the associated plasticity we have

$$\left(-\tfrac{1}{2}\mathcal{L}_{\boldsymbol{\chi}}[\mathbf{B}_{eq}]\mathbf{B}_{eq}^{-1}, -\dot{\alpha}\right) \in \partial\mathcal{I}_E \tag{9.108}$$

where $\partial\mathcal{I}_E$ is subdiferential of the functional $\mathcal{I}_E$. Equation (9.108) is equivalent to the following conditions:

$$-\tfrac{1}{2}(\mathcal{L}_{\boldsymbol{\chi}}[\mathbf{B}_{eq}])\mathbf{B}_{eq}^{-1} = \dot{\lambda}\frac{\partial\mathcal{F}}{\partial \mathrm{dev}\boldsymbol{\tau}_{EQ}} = \dot{\lambda}\frac{\mathrm{dev}\boldsymbol{\tau}_{EQ}}{\|\mathrm{dev}\boldsymbol{\tau}_{EQ}\|} = \dot{\lambda}\mathbf{n} \tag{9.109}$$

$$\dot{\alpha} = \sqrt{\tfrac{2}{3}}\dot{\lambda} \tag{9.110}$$

$$\dot{\lambda} \geq 0\,; \qquad \mathcal{F} \leq 0\,; \qquad \dot{\lambda}\mathcal{F} = 0\,. \tag{9.111}$$

If instead of the plastic part the Perzyna viscoplastic deformation were assumed Eq. (9.109) would be replaced by

$$-\tfrac{1}{2}(\mathcal{L}_{\boldsymbol{\chi}}[\mathbf{B}_{eq}])\mathbf{B}_{eq}^{-1} = \gamma\left(\frac{\langle \mathrm{dev}\boldsymbol{\tau}_{EQ} - \hat{y}\rangle}{\hat{y}}\right)\frac{\partial\mathcal{F}}{\partial \mathrm{dev}\boldsymbol{\tau}_{EQ}} \tag{9.112}$$

where γ is the viscoplastic material parameter, and $\langle \mathrm{dev}\boldsymbol{\tau}_{EQ} - \hat{y}\rangle$ represents overstress.

9.7.7 Integration of the constitutive equation

The numerical algorithm proposed for the combined viscoelastic/elastoplastic model [**?**] employ the integration method of elastoplasticity proposed by Simo [44] and the integration method of viscoelastic model developed by Reese and Govindjee [45]. Basically the algorithms employed make use of the operator splitting which consists of the elastic predictor made in the first step and the inelastic correction performed in the second step. The extension proposed by M. Luege [**?**] consists in consideration of elastoplasticity combined with viscoelasticity.

The material derivatives of the tensors $\mathbf{B}_{eq}$ and $\mathbf{B}_e$ can be split into elastic and inelastic parts

$$\dot{\mathbf{B}}_{eq} = \frac{d}{dt}(\mathbf{F}\mathbf{C}_p^{-1}\mathbf{F}^T) = \underbrace{\mathbf{l}\mathbf{B}_{eq} + \mathbf{B}_{eq}\mathbf{l}^T}_{elastic} + \underbrace{\mathcal{L}_{\boldsymbol{\chi}}[\mathbf{B}_{eq}]}_{plastic} \tag{9.113}$$

$$\dot{\mathbf{B}}_{e} = \frac{d}{dt}(\mathbf{F}\mathbf{C}_i^{-1}\mathbf{F}^T) = \underbrace{\mathbf{l}\mathbf{B}_{e} + \mathbf{B}_{e}\mathbf{l}^T}_{elastic} + \underbrace{\mathcal{L}_{\boldsymbol{\chi}}[\mathbf{B}_{e}]}_{viscous} \tag{9.114}$$

Given the state of material at time t_{n-1} and the total deformation at time t_n defined by $\mathbf{F}_n = \mathbf{F}_\Delta\mathbf{F}_{n-1}$ the algorithm presented below allows us to determine $\mathbf{B}_{eq}^n$, $\mathbf{B}_e^n$ and α^n in the following steps.

Step 1: Elastic prediction

Given:

$$\mathbf{F}_{n-1}, \mathbf{B}_e^{n-1}, \mathbf{B}_{eq}^{n-1}, \alpha^{n-1}$$

$$\mathbf{F}_\Delta^t = \mathbf{F}^t \mathbf{F}_{n-1}^{-1} \quad \text{with} \quad \mathbf{F}_\Delta = \mathbf{F}_n \mathbf{F}_{n-1}^{-1} \quad \text{for} \quad t = t_n$$

Determine $\mathbf{B}_{eq}^{trial,t}$, $\mathbf{B}_e^{trial,t}$, $\alpha^{trial,t}$ assuming that the deformation gradient tensors defining inelastic deformations, $\mathbf{F}_p$ and $\mathbf{F}_i$ remain constants (with values the same as at time t_{n-1})

$$\begin{aligned}
&\mathbf{B}_{eq}^{trial,t} = \mathbf{F}_\Delta^t \mathbf{B}_{eq}^{n-1} (\mathbf{F}_\Delta^t)^T && \rightarrow \bar{\mathbf{B}}_{eq}^{trial,t} = J^{-2/3} \mathbf{B}_{eq}^{trial,t} \\
&\mathbf{B}_e^{trial,t} = \mathbf{F}_\Delta^t \mathbf{B}_e^{n-1} (\mathbf{F}_\Delta^t)^T && \rightarrow \bar{\mathbf{B}}_e^{trial,t} = J^{-2/3} \mathbf{B}_e^{trial,t} \\
&\alpha^{trial,t} = \alpha^{n-1} && \rightarrow R^{trial,t} = R(\alpha^{trial,t}) \\
&\mathrm{dev}\boldsymbol{\tau}_{EQ}^{trial,t} = 2J^{-1} \mathbf{B}_{eq}^{trial,t} \frac{\partial \Psi_{EQ}^{iso}(\bar{\mathbf{B}}_{eq}^{trial,t})}{\partial \bar{\mathbf{B}}_{eq}} && \rightarrow \mathcal{F}^{trial,t}(\mathrm{dev}\boldsymbol{\tau}_{EQ}^{trial,t}, R^{trial,t})
\end{aligned} \tag{9.115}$$

where $J = \det \mathbf{F}^t$.

Step 2a: Viscous correction

The viscous correction is defined by the solution of the following system:

$$\dot{\mathbf{B}}_e = \mathcal{L}_{\boldsymbol{\chi}}[\mathbf{B}_e] = -\frac{2}{\eta_D} \mathrm{dev}\boldsymbol{\tau}_{NEQ} \mathbf{B}_e$$

$$\mathbf{B}_e(t_{n-1}) = \mathbf{B}_e^{trial,n}$$

$$\mathrm{dev}\boldsymbol{\tau}_{NEQ} := 2\mathbf{B}_e \frac{\partial \Psi_{NEQ}^{iso}(\bar{\mathbf{B}}_e)}{\partial \mathbf{B}_e}$$

An approximate solution is obtained applying the algorithm of exponential mapping which predicts for the time t_n the following solution

$$\mathbf{B}_{eq}^n = \exp\left[-2\frac{\Delta t}{\eta_D} \mathrm{dev}\boldsymbol{\tau}_{NEQ}^n \mathbf{B}_e^{trial,n}\right] \tag{9.116}$$

Step 2b: Plastic correction

The plastic correction, independent of the viscous correction is obtained as the solution of the following system

$$\dot{\bar{\mathbf{B}}}_{eq} = 2\dot{\lambda} \frac{\mathrm{dev}\boldsymbol{\tau}_{EQ}}{\|\mathrm{dev}\boldsymbol{\tau}_{EQ}\|} \bar{\mathbf{B}}_{eq}$$

$$\dot{\alpha} = \tfrac{2}{3}\dot{\lambda}$$

$$\mathrm{dev}\boldsymbol{\tau}_{EQ} := 2\mathbf{B}_{eq}\frac{\partial \Psi^{iso}_{EQ}(\bar{\mathbf{B}}_{eq})}{\partial \mathbf{B}_{eq}}\,, \quad R = R(\alpha)$$

with the complementary Kuhn–Tucker conditions

$$\dot{\lambda} \geq 0\,; \qquad \mathcal{F}(\mathrm{dev}\boldsymbol{\tau}_{EQ}, R) \leq 0\,; \qquad \dot{\lambda}\mathcal{F} = 0\,.$$

and the following initial conditions

$$\mathbf{B}_{eq}(t_{n-1}) = \mathbf{B}^{trial,t}_{eq}$$

$$\alpha(t_{n-1}) = \alpha^{trial,t}$$

The solution is as follows.
If $\mathcal{F}^{trial,n} < 0$ the elastic solution defines the solution for the time t_n

$$\mathbf{B}^n_{eq} = \mathbf{B}^{trial,n}_{eq}\,, \quad \alpha^n = \alpha^{trial,n}\,, \quad \boldsymbol{\tau}^n_{EQ} = \boldsymbol{\tau}^{trial,n}_{EQ}\,, \quad R^n = R^{trial,n}$$

Otherwise the plastic correction is performed according to return mapping algorithm obtained as a solution of the following system:

$$\mathbf{B}^n_{eq} = \exp[-2\Delta\lambda\mathbf{n}^n]\mathbf{B}^{trial,t}_{eq}$$

$$\alpha^n = \alpha^{trial,t}\sqrt{\tfrac{2}{3}}\Delta\lambda$$

$$\mathrm{dev}\boldsymbol{\tau}_{EQ} := 2\mathbf{B}_{eq}\frac{\partial \Psi^{iso}_{EQ}(\bar{\mathbf{B}}^n_{eq})}{\partial \mathbf{B}_{eq}}\,,$$

$$R^n = R(\alpha^n)$$

$$\mathbf{n}^n = \frac{c}{\left\|\mathrm{dev}\boldsymbol{\tau}^n_{EQ}\right\|}$$

with the complementary Kuhn–Tucker conditions

$$\Delta\lambda \geq 0\,; \qquad \mathcal{F}(\mathrm{dev}\boldsymbol{\tau}^n_{EQ}, R^n) \leq 0\,; \qquad \Delta\lambda\mathcal{F}(\mathrm{dev}\boldsymbol{\tau}^n_{EQ}, R^n) = 0\,.$$

Verifying the condition

$$\mathcal{F}(\mathrm{dev}\boldsymbol{\tau}^n_{EQ}(\Delta\lambda), R^n(\Delta\lambda)) = 0\,.$$

the value of $\Delta\lambda$ is found. The iterative Newton–Raphson method can be used to solve (9.7.7):

$$k = 0\,, \quad \Delta\lambda^{k=0} = 0\,, \quad \mathcal{F}^{k=0} = \mathcal{F}^{trial}\,.$$

$$k = k + 1\,,$$

$$\delta\Delta\lambda^k = -\frac{\mathcal{F}^{k-1}}{\left.\dfrac{\partial\mathcal{F}}{\partial(\Delta\lambda)}\right|_{k-1}}$$

$$\Delta\lambda^k = \Delta\lambda^{k-1} + \delta\Delta\lambda^k$$

$$\mathcal{F}^k = \mathcal{F}(\Delta\lambda^k)$$

The iteration process is terminated if $\mathcal{F}^k < tol$. Then the variables for $t = t_n$ are updated.

Chapter 10

Constitutive properties of the polymer–metal interface

10.1 Introduction

Adhesion across the polymer–metal interface is a key factor in the good performance of polymer coated metal laminates in packaging industry. Polymer coated steel laminate are obtained by coating a polymer (PET) film on to electro-chemically coated steel (ECCS) by a co-extrusion process. The polar nature of polypethylene terephtalate (PET) makes it an excellent material for achieving adhesion with metals. ECCS has a thin coating of metallic chromium followed by a chromium-oxide layer, both together not thicker than 14 nm, which acts as an adhesion layer between steel and PET.

In the manufacturing process the interface is subjected to high stresses. It is crucial that the adhesion between the polymer and the metal is strong enough to endure tough forming conditions. Adhesion dictates the deformation of the laminate and its ultimate performance.

10.2 Polymer-metal interface

Adhesion is not a sharp boundary between the two materials, but can be more realistically regarded as the transition zone between the metal substrate and the polymer having its volume and distinct physical properties. The interface properties depend on their binding of chemical nature as well as on the geometric characteristics of the substrate surface.

10.2.1 Adhesion bonding between polymer and metal

The polar nature of PET also makes it an excellent metarial for achieving adhesion with metals. A polymer molecule can be bonded to a metal in more than one site. The strength of a polymer depends on the strength of inter-chain Van der Waal's forces. The total force of adhesion between phases depends on the single bonds associated with the type of intermolecular and interatomic interactions across the interface, the number of interaction sites and range of bonds. Comparing the range of intermolecular forces to the interaction of H-bonds, other weaker forces are negligible, we can assume that H-bonds play a dominant role in adhesion.

10.3 Polymer-metal adhesion under deformation and delamination

The purpose of the forming process is to obtain the product of required shape without fracturing and loss of adhesion. During the forming operation the adhesion layer does not remain intact, due to continuous formation of new polymer and metal surfaces at the interface. It is important to consider the influence of the deformation of the laminate on the adhesion at the polymer–metal interface.

Chapter 11

Modelling the interface as the contact problem with adhesion

11.1 Interfaces in finite element modelling

The finite element method has been used for many years for the analysis of contact interfaces. Most of the earlier work was done using the assumption of perfect bonding between the two different materials. with compatibility of displacements at the interface (which is equivalent to the assumptions of the infinite strength of the interface). The models with rigid bonds across the interface do not describe properly not only a mechanism of the interface but the load transfer in the mechanical system, as well.

Standard contact formulation neglects tensile stresses at the interfaces and allows the shear stresses only when the contact pressure is compressive. Accurate modelling of the polymer–metal interface requires taking into account adhesion between two contacting materials allowing us to transmit tensile forces at the interface as well as the tangential interaction produced by adhesive bonds.

In the next section some fundamental notions related to adhesion are recalled. Next a general approach to the formulation of unilateral contact allowing adhesive forces is proposed. This will allow us to create a realistic finite element model of the polymer–metal interface.

11.2 Adhesion: some basic notions

According to [46] there is a difference between adhesion at the molecular level and adhesion in engineering. The lack of adhesion that we observe in engineering circumstances is rather an aberration that depends on the mechanisms of contact than on molecular adhesion. If we define the molecular forces through the work of adhesion per unit area of contact, equations for the mechanical force of adhesion in particular

geometries are now briefly examined. Primarily, however, we observe that adhesion between two solids may be due to ionic, covalent metallic, hydrogen or van der Waals forces; for more details the reader is referred to [46, 47, 48]. To cut these bonds and to reversibly separate the two solids 1 and 2 in contact on unit area, energies γ_1 and γ_2 are needed to create the unit areas 1 and 2, whereas the excess energy γ_{12} (interfacial energy) is recovered. The quantity

$$w = \gamma_1 + \gamma_2 - \gamma_{12}, \tag{11.1}$$

is the *Dupré energy of adhesion* or the *thermodynamic work of adhesion.* We observe that for a single crystal one has $\gamma_{12} = 0$; between two grains of polycrystal γ_{12} is the grain boundary energy ($\gamma_{GB} = \gamma/3$) or the twin boundary energy ($\gamma_{TB} = \gamma/50$).

The separation never occurs as a whole, but by progression of a crack. During this propagation interface bonds are broken, elastic energy is released and irreversible work is dissipated at the crack tip.

Work of adhesion is a useful quantity because it distinguishes the two states, contact and separation. This work is done over a very small distance for van der Waals forces, 99% of the work is achieved when the surfaces are pulled 1 nm apart. For other types of bonding, such as ionic and covalent, even smaller distances are involved. Thus, the precise shape of the force separation curve need not be known to understand many phenomena. Indeed, the precise shape may even not be measurable because of the instability of the spontaneous jumping of smooth surfaces into contact.

The available expressions for the calculation of the mechanical force F needed to separate two contacting bodies depicted in Fig. 11.1 [46].

The force F needed to separate from molecular contact two identical spherical particles of diameter D and work of adhesion w (Fig. 11.1A) is given by

$$F = kwD\,, \tag{11.2}$$

where k is a constant near unity. For elastic spheres $k = 3\pi/8$.

A polymer film peeling from a rigid substrate is also described by Eq. (11.2), but with D replaced by the film width (Fig. 11.1B).

In more complex situations, where the joint is stretched significantly during breakage as in the lap joint of Fig. 11.1C, the elastic modulus E and thickness d of the materials become important and the adhesion criteria for fracture becomes

$$F = (4wEd)^{1/2}b\,, \tag{11.3}$$

which has the same form as Griffith's cracking equation for glass.

These equations are instructive because they show that adhesion force can vary substantially with geometry and material stiffness, as well with the molecular surface quantitied by w.

Kendall discussed also the influence of fluid molecules on contacting solid surfaces [46]. Other interacting adhesion mechanisms are adhesive drag, hysteresis, stringing and clustering.

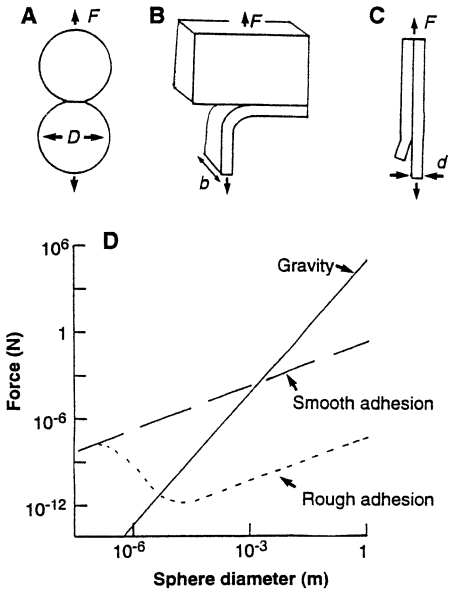

Figure 11.1: (A) Two identical spheres in contact under van der Waals attraction with a force F applied to separate them. (B) peeling of an elastic film from a rigid surface. (C) Cracking of a lap joint. (D) Comparison of the adhesion force and gravity for very smooth and rough spheres of different diameteres, after [46]

11.2.1 Modelling unilateral contact with adhesion

A general framework for the study of contact problems with adhesion has been developed in [49, 50]. The main idea consists in introducing the *intensity of adhesion* $\beta(\mathbf{x}, t)$ where $\mathbf{x} \in \Gamma_c$ and t stands for the time variable. Here Γ_c is the surface of potential contact. To simplify the presentation, let us first consider the unilateral contact with adhesion of a deformable body, occupying a domain Ω of $\mathbb{R}^3$ in its undeformed configuration, with a rigid obstacle. Contact of deformable bodies simulating the system bone-prosthesis or bone-cement-prosthesis will also be considered.

The intensity of adhesion β is such that:

(i) if $\beta = 1$ all the bonds are active,

(ii) if $\beta = 0$ all the bonds are broken or the adhesion is absent,

(iii) if $0 < \beta < 1$, a part β of the the bonds remain active, the remaining bonds are broken, the adhesion is partial.

Let $\Gamma = \partial\Omega$ consists of three parts: Γ_0, Γ_1 and Γ_c such that $\Gamma = \bar{\Gamma}_0 \cup \bar{\Gamma}_1 \cup \bar{\Gamma}_c$. Here the bar denotes the closure of set. Consider a linear elastic body satisfying

$$\begin{aligned} \sigma_{ij,j} + f_i &= 0 \quad \text{in } \Omega\,, && (11.4)\\ \mathbf{u} &= \mathbf{0} \quad \text{on } \Gamma_0\,, && (11.5)\\ \sigma_{ij} n_j &= g_i \quad \text{on } \Gamma_1\,, && (11.6)\\ \sigma_{ij} n_j &= R_i \quad \text{on } \Gamma_c\,, && (11.7)\\ \sigma_{ij} &= a_{ijkl} e_{ij}(\mathbf{u})\,, && (11.8) \end{aligned}$$

where

$$e_{ij}(\mathbf{u}) = u_{(i,j)} = \frac{1}{2}\left(\frac{\partial u_i}{\partial x_j} + \frac{\partial u_j}{\partial x_i}\right)\,. \tag{11.9}$$

The elastic moduli a_{ijkl} are functions from $L^\infty(\Omega)$ and satisfy the following condition

$$\exists c_1 \geq c_0 > 0\,, \quad \forall \boldsymbol{\epsilon} \in \mathbb{E}^3_s \quad c_0 \epsilon_{ij}\epsilon_{ij} \leq a_{ijkl}(\mathbf{x})\epsilon_{ij}\epsilon_{kl} \leq c_1 \epsilon_{ij}\epsilon_{ij} \tag{11.10}$$

for almost every $\mathbf{x} \in \Omega$. Here $\mathbb{E}^3_s$ stands for the space of symmetric 3×3 matrices, whilst $\mathbf{n} = (n_i)$ denotes the outward unit normal to Γ. Obviously, the functions $\mathbf{g}$ and $\mathbf{f}$ are prescribed. Our assumptions allow for the body to be made of anisotropic material. Let $\mathbf{w} = (w_i)$ denote displacement field of the rigid foundation. We set

$$[\![\mathbf{u}]\!] = \mathbf{u} - \mathbf{w}\,. \tag{11.11}$$

The jump $[\![\mathbf{u}]\!]$ and the adhesion intensity β are not independent since they satisfy

$$0 \leq \beta \leq 1\,, \quad \beta[\![\mathbf{u}]\!] = \mathbf{0}\,, \quad [\![\mathbf{u}]\!] \cdot \mathbf{n} \leq 0 \quad \text{on } \Gamma_c\,. \tag{11.12}$$

The condition (11.12) implies that for $[\![\mathbf{u}]\!] \neq \mathbf{0}$ there is no interaction between the structure and the foundation, i.e., $\beta = 0$.

It is natural to introduce the following *nonconvex* set of constraints

$$K = \{(\gamma, \mathbf{v}) \,|\, 0 \leq \gamma \leq 1\,,\ \gamma\mathbf{v} = \mathbf{0}\,,\ \mathbf{v}\cdot\mathbf{n} = 0 \quad \text{on } \Gamma_c\}\,. \tag{11.13}$$

From now on we set $\mathbf{w} = \mathbf{0}$. By I_K we denote the indicator function of the set K, cf. [**?**]

$$I_K(\gamma, \mathbf{v}) = \begin{cases} 0 & \text{if } (\gamma, \mathbf{v}) \in K\,, \\ +\infty & \text{otherwise}\,. \end{cases} \tag{11.14}$$

Many possibilities are offered to model the contact with adhesion between Ω and the foundation. Consider now some physical motivated cases:

(i) the adhesion is described by using the generalized potential $\varphi(\beta, \mathbf{u})$; for instance

$$\varphi(\beta, \mathbf{u}) = \int_{\Gamma_c} \left(\frac{k}{2}|\mathbf{u}|^2 - w\beta\right) \mathrm{d}\Gamma + I_K(\beta, \mathbf{u})\,, \tag{11.15}$$

where k is a nonnegative constant and w stands for Dupré's energy, introduced earlier.

In general, adhesion action on Γ_c consists of the interior force F with the dimension of a surface work and the external force A. For instance, A may be the electrostatic force modifying the contact. In the case of the contact bone–prosthesis A may model the forces existing in a thin membrane, which develop between the bone and the prosthesis, cf. [**?**].

Anyway, we have

$$F = A \tag{11.16}$$

In many practical situations A disappears. It is natural to split F into reversible $\mathbf{F}_e$ and irreversible part $\mathbf{F}_i$ (on Γ_c). We have

$$(\mathbf{F}_e, \mathbf{R}) \in \partial\varphi(\beta, \mathbf{u})\,, \tag{11.17}$$

where $\partial\varphi$ denotes the *local subdifferential* of the the potential φ, cf. [49, 50]. We observe that I_K is not a convex function. Consequently, in the constitutive relationship (11.17) $\partial\varphi$ cannot be the usual subdifferential, cf. [**?**]. Alternatively, $\partial\varphi$ can be interpreted as Clarke's subdifferential [**?**]. The last notion was not employed by [49, 50].

To describe the irreversible part $\mathbf{F}_i$ of F, we introduce a convex, positive functional Φ of $\dot\beta = \mathrm{d}\beta/\mathrm{d}t$, such that $\Phi(0) = 0$. Then

$$\mathbf{F}_i \in \partial\Phi(\dot\beta)\,, \tag{11.18}$$

where $\partial\Phi$ denotes the subdifferential of Φ. We recall that

$$\partial\Phi(\dot\beta) = \{G \,|\, \Phi(\gamma) - \Phi(\dot\beta) \geq \int_{\Gamma_c} G(\gamma - \dot\beta)\,\mathrm{d}\Gamma \quad \text{for every} \gamma\}\,. \tag{11.19}$$

For instance, a nonlinear viscous potential of Norton–Hoff type is given by

$$\Phi(\dot\beta) = \int_{\Gamma_c} \frac{1}{p}\left[(\omega * \dot\beta)\dot\beta\right]^{p/2}\,\mathrm{d}\Gamma = \frac{1}{p}\left(\langle\omega * \dot\beta, \dot\beta\rangle\right)^{p/2}\,. \tag{11.20}$$

Here $*$ denotes the convolution product and ω is a C^∞-function, which is positive, and $p > 1$. For $p = 2$ we have

$$\Phi(\dot\beta) = \frac{1}{2}\langle\omega * \dot\beta, \dot\beta\rangle = \frac{1}{2}\int_{\Gamma_c} (\omega * \dot\beta)\dot\beta\,\mathrm{d}\Gamma\,, \tag{11.21}$$

and

$$\mathbf{F}_i = \omega * \dot\beta = \int_{\Gamma_c} \omega(\mathbf{x} - \mathbf{y})\dot\beta(\mathbf{y})\,\mathrm{d}y\,. \tag{11.22}$$

Introducing the energy release rate denoted by H in [49, 51, 50], one can consider all possible situation occurring during contact, i.e., the total adhesion ($\mathbf{u} = \mathbf{0}$, $\beta = 1$, on Γ_c), partial adhesion ($\mathbf{u} = \mathbf{0}$, $0 < \beta < 1$), contact without adhesion ($\mathbf{u} = \mathbf{0}$, $\beta = 0$), and lack of adhesion ($\mathbf{u} \neq \mathbf{0}$, $\beta = 0$).

We omit the details. It is worth noting, however, that for $\mathbf{u} \neq \mathbf{0}$ and $\beta = 0$ we have

$$R_n + ku_n \leq 0\,, \quad (R_n + ku_n)u_n = 0\,, \quad \mathbf{R}_T + k\mathbf{u}_T = \mathbf{0}\,, \quad \text{on } \Gamma_c \tag{11.23}$$

where $R_n = R_i n_i$, $u_n = u_i n_i$, $\mathbf{R}_T = \mathbf{R} - R_n\mathbf{n}$, $\mathbf{u}_T = \mathbf{u} - u_n\mathbf{n}$. If $\mathbf{F}_i$ is given by (11.22), then $\mathbf{F}_i(\mathbf{x})$ does not necessarily vanishes even for $\mathbf{x}$ belonging to the decohesion zone.

(ii) Consider now the contact with adhesion and friction. The potential (11.15) is replaced by

$$\varphi(\beta, \mathbf{u}, \dot{\mathbf{u}}_T) = \int_{\Gamma_c}\left(\frac{k}{2}u_n^2 - w\beta\right)\,\mathrm{d}\Gamma + \int_{\Gamma_c} D\left(\mathbf{R}_n, -\dot{\mathbf{u}}_T\right)\,\mathrm{d}\Gamma + I_K(\beta, \mathbf{u})\,. \tag{11.24}$$

Here D denotes the friction dissipation density, cf. [**?**]. It may be assumed that D depends additionally on β. The function $D(R_n, \cdot)$ is assumed to be convex, thus D is subdifferentiable in the second argument. We recall that $D(R_n, \cdot)$ is finite and lower semicontionuous. The reaction $\mathbf{R}$ is written as follows

$$\mathbf{R} = \mathbf{R}_n + \mathbf{R}_T = R_n\mathbf{n} + \mathbf{R}_T\,.$$

Instead of the relationship (11.17) we have

$$(\mathbf{F}_e, \mathbf{R}_n, \mathbf{R}_T) \in \partial\varphi_1(\beta, \mathbf{u}, \dot{\mathbf{u}}_T)\,. \tag{11.25}$$

Now the condition $(11.23)_3$ is to be replaced by

$$\mathbf{R}_T \in \partial_2 D(\mathbf{R}_n, -\dot{\mathbf{u}}_T)\,, \tag{11.26}$$

and expresses the friction law. Here $\partial_2 D(\mathbf{R}_n, -\dot{\mathbf{u}}_T)$ stands for the partial subdifferential with respect to the second argument. In the case of Coulomb's friction we have

$$\mathbf{R}_T = -\lambda\dot{\mathbf{u}}_T\,, \quad \lambda 0 \geq 0\,. \tag{11.27}$$

(iii) Consider now the viscous behaviour with impossible bond restitution. Let $\mathbb{M}^-(\Gamma_c)$ be the set of negative measures on Γ_c. The function β can be discontinuous. The space of functions with bounded variation constitutes a proper mathematical framework for β, cf. [**?**, **?**]. We introduce the following potential for F^i:

$$\Phi_1(\dot{\beta}) = \frac{1}{2}\langle \omega * \dot{\beta}, \dot{\beta}\rangle + I_{\mathbb{M}^-}(\dot{\beta})\,, \tag{11.28}$$

where

$$I_{\mathbb{M}^-}(\dot{\beta}) = \begin{cases} 0 & \text{if } \dot{\beta} \in \mathbb{M}^-\,, \\ +\infty & \text{otherwise}\,. \end{cases} \tag{11.29}$$

Denote by $\mathcal{O}$ the interior of the support of $\dot{\beta}$, then

$$\mathbf{F}_i(\mathbf{x}) = (\omega * \dot{\beta})(\mathbf{x})\,, \qquad \text{if} \mathbf{x} \in \mathcal{O}\,, \tag{11.30}$$

$$\mathbf{F}_i(\mathbf{x}) \geq (\omega * \dot{\beta})(\mathbf{x})\,, \qquad \text{if} \mathbf{x} \notin \mathcal{O}\,. \tag{11.31}$$

Also in this case one can consider the unilateral frictionless contact or unilateral contact with friction. In the former case φ is given by (11.15) whilst in the latter the constitutive modelling involves φ_1 given by (11.17).

(iv) One can envisage much more complicated contact modelling involving adhesion and friction. For instance, it is possible to develop a first gradient theory involving $\nabla\beta$, cf. [51]. The reversible part $\mathbf{F}_e$ of F may be modelled by a non-quadratic, or even non-convex expression instead of $\frac{1}{2}k|\mathbf{u}|^2$. Having in mind cementless prostheses, their coated parts can be modelled by using fractals. It would also be interesting and very useful to include influence of wear debris on loss of adhesion, cf. [**?**].

(v) Consider now the contact of two deformable bodies, cf. Fig. 11.2. Γ_c is now the surface of potential contact. Now $[\![\mathbf{u}]\!] = \mathbf{u}^{(1)} - \mathbf{u}^{(2)}$, $\mathbf{R} = \mathbf{R}^{(1)} = -\mathbf{R}^{(2)}$. The unit normal vector $\mathbf{n}$ is taken as exterior to Ω_1.

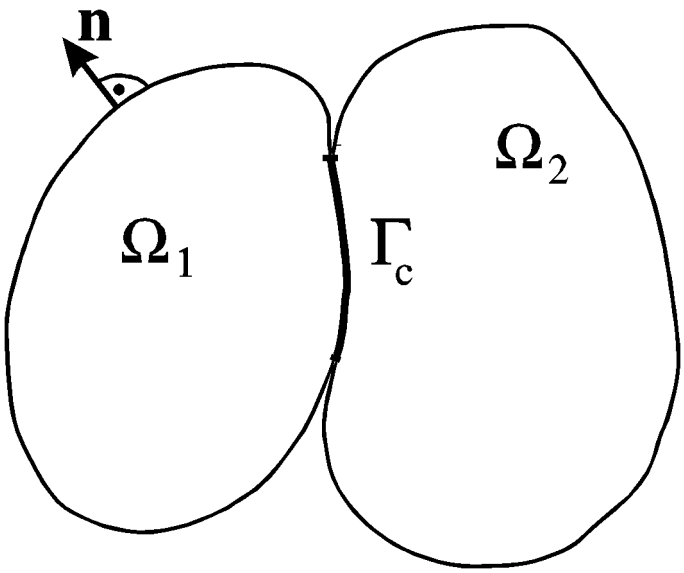

Figure 11.2: Two deformable bodies in contact

The set K of constraints is to be replaced by

$$K_1 = \left\{(\gamma, [\![\mathbf{u}]\!]), [\![\mathbf{u}]\!] = \mathbf{u}^{(1)} - \mathbf{u}^{(2)} \,|\, 0 \le \gamma \le 1\,, \gamma_{[\![\mathbf{u}]\!]} = \mathbf{0}\,, [\![\mathbf{u}]\!] \le 0 \text{ on } \Gamma_c\right\}\,, \tag{11.32}$$

In the formulae (11.15), (11.17), (11.24), (11.25) $\mathbf{u}$ is to be replaced by $[\![\mathbf{u}]\!]$ whilst in (11.23) u_n, u_T by $[\![u_n]\!]$, $[\![u_T]\!]$, respectively. The friction law takes the form

$$\mathbf{R}_T \in \partial_2(\mathbf{R}_n, [\![\dot{\mathbf{u}}_T]\!])\,. \tag{11.33}$$

11.2.2 Formulation of the initial–boundary value problem with adhesion

Let consider the situation depicted in Fig. 11.2. Both solids are assumed to be made of linear elastic, anisotropic and nonhomogeneous materials. The system of equations (11.4)–(11.7) is to be replaced by

$$\begin{aligned}
\sigma^{(\alpha)}_{ij,j} + f^{(\alpha)}_i &= 0 \quad \text{in } \Omega_{(\alpha)}\,, && (11.34)\\
\mathbf{u}^{(\alpha)} &= \mathbf{0} \quad \text{on } \Gamma^{(\alpha)}_0\,, && (11.35)\\
\sigma^{(\alpha)}_{ij} n^{(\alpha)}_j &= g^{(\alpha)}_i \quad \text{on } \Gamma^{(\alpha)}_1\,, && (11.36)\\
\sigma^{(1)}_{ij} n^{(1)}_j &= -\sigma^{(2)}_{ij} n^{(2)}_j = R_i \quad \text{on } \Gamma_c\,, && (11.37)\\
\sigma^{(\alpha)}_{ij} &= a^{(\alpha)}_{ijkl} e_{ij}(\mathbf{u}^{(\alpha)})\,, && (11.38)
\end{aligned}$$

where $\alpha = 1, 2$. All the quantities appearing in Eqs. (11.34)–(11.38) depend on spatial variables and time $t \in [0, T]$. Here and below there is no summation over α. The initial

conditions are specified by

$$\begin{aligned} \beta(0,\mathbf{x}) &= \beta_0(\mathbf{x})\,, \quad \mathbf{x}\in\Gamma_c\,, && (11.39)\\ \mathbf{u}^{(\alpha)}(0,\mathbf{x}^{(\alpha)}) &= \mathbf{u}^{(\alpha)}\beta_0(\mathbf{x}^{(\alpha)})\,, \quad \mathbf{x}^{(\alpha)}\in\Omega_{(\alpha)}\,. && (11.40)\end{aligned}$$

We assume that adhesion is modelled by the functional (11.20) and

$$\varphi(\beta,[\![\mathbf{u}]\!]) = -\int_{\Gamma_c} w\beta\,\mathrm{d}\Gamma + I_{K_1}(\beta,[\![\mathbf{u}]\!])\,, \tag{11.41}$$

where K_1 is defined by (11.32). The presence of the indicator function I_{K_1} makes the functional φ nondifferentiable. Having in mind approximate solutions we regularize it as follows, cf. [52].

$$\varphi_2(\beta,[\![\mathbf{u}]\!]) = -\int_{\Gamma_c} w\left[\beta\,\mathrm{d}\Gamma + \frac{1}{4\varepsilon}\int_{\Gamma_c} 2\beta^2\left|[\![\mathbf{u}]\!]\right|^2 + \left|(\beta-1)^+\right|^4 + \left|\beta^-\right|^4 + 2\left|[\![\mathbf{u}_n]\!]^+\right|^2\right]\mathrm{d}\Gamma\,, \tag{11.42}$$

where $\varepsilon>0$ and a^+ stands for the positive part of a whilst a^- for the negative part; similarly $[\![\mathbf{u}_n]\!]^+ = [\![u_n]\!]^+\mathbf{n}$.

We set

$$a^{(\alpha)}(\mathbf{u}^{(\alpha)},\mathbf{v}^{(\alpha)}) = \int_{\Omega_\alpha} a^{(\alpha)}_{ijkl}(x)e_{ij}(\mathbf{u}^{(\alpha)})e_{kl}(\mathbf{v}^{(\alpha)})\,\mathrm{d}\Omega_\alpha\,, \tag{11.43}$$

$$l^{(\alpha)}(\mathbf{v}^{(\alpha)}) = \int_{\Omega_\alpha} f_i^{(\alpha)}\cdot v_i^{(\alpha)}\,\mathrm{d}\Omega_\alpha + \int_{\Gamma_1^\alpha} g_i^{(\alpha)}v_i^{(\alpha)}\,\mathrm{d}\Gamma\,. \tag{11.44}$$

The approximate problem reads: find $\mathbf{u}^{(\alpha)}$ $(\alpha=1,2)$ vanishing on $\Gamma_0^{(\alpha)}$ and β_ε such that

$$a^{(1)}(\mathbf{u}^{(1)},\mathbf{v}^{(1)}) + a^{(2)}(\mathbf{u}^{(2)},\mathbf{v}^{(2)}) + \frac{1}{\varepsilon}\int_{\Gamma_c}\left(\beta^2[\![\mathbf{u}]\!] + [\![\mathbf{u}_n]\!]^+\right)\cdot[\![\mathbf{v}]\!]\,\mathrm{d}\Gamma = l^{(1)}(\mathbf{v}^{(1)}) + l^{(2)}(\mathbf{v}^{(2)})\,, \tag{11.45}$$

for each $\mathbf{v}^{(\alpha)}$ vanishing on $\Gamma_0^{(\alpha)}$, and

$$\left(\langle\omega*\dot\beta,\dot\beta\rangle\right)^{p/2-1}\omega*\dot\beta = w + A\,\frac{1}{\varepsilon}\left[\beta\left|[\![\mathbf{u}]\!]\right|^2 + \left|(\beta-1)^+\right|^3 - \left|\beta^-\right|^3\right] \quad \text{on } \Gamma_c\,, \tag{11.46}$$

$$\begin{aligned} \beta(0,\mathbf{x}) &= \beta_0(\mathbf{x}) \qquad \text{on } \Gamma_c\\ \mathbf{u}^{(\alpha)}(0,\mathbf{x}) &= \mathbf{u}_0^{(\alpha)}(\mathbf{x})\,, \quad \mathbf{x}\in\Omega_\alpha\,. \end{aligned} \tag{11.47}$$

Obviously, both β and $\mathbf{u}^{(\alpha)}$ depend on ε. We observe that the quantity

$$-\left\{\frac{1}{\varepsilon}\beta^2[\![\mathbf{u}]\!] + \frac{1}{\varepsilon}[\![\mathbf{u}_n]\!]^+\right\}$$

is an approximation of $\mathbf{R}$ whilst

$$-\left\{w - \frac{1}{\varepsilon}\left[\beta\left|[\![\mathbf{u}]\!]\right|^2 + \left|(\beta-1)^+\right|^3 - \left|\beta^-\right|^3\right]\right\}$$

is an approximation of $\mathbf{F}_i$. It is also wort noting, that precise formulation of the exact problem involves the notion of hemivariational inequality, which here we want to avoid.

Remark 7.1. To solve approximately adhesion problem with friction one has to regularize the functional of the total friction dissipation defined by

$$J(R_n, [\![\dot{\mathbf{u}}_T]\!]) = \int_{\Gamma_c} D(R_n, [\![\dot{\mathbf{u}}_T]\!])\,\mathrm{d}\Gamma\,.$$

This fact is well known in the numerical study of contact problems with friction, cf. [**?**].

Chapter 12

Constitutive contact models

12.1 Frictional contact model

First we will consider the frictional contact model. The contact conditions are considered using master/slave approach.

A gap/penetration function g is defined for each point $\mathbf{x}^s$ belonging to a slave surface as

$$g = (\mathbf{x}^s - \bar{\mathbf{x}}^m) \cdot \mathbf{n} \tag{12.1}$$

where $\bar{\mathbf{x}}^m$ is the closest point projection of the slave node on the master surface and $\mathbf{n}$ is the unit normal vector, normal to the master surface defined at the point $\bar{\mathbf{x}}^m$ and directed outwards. The contact force $\mathbf{p}$ at the node $\mathbf{x}^s$ is decomposed into the normal and tangential components, $\mathbf{p}_n$ and $\mathbf{p}_T$, respectively

$$\mathbf{p} = \mathbf{p}_n + \mathbf{p}_T = p_n \mathbf{n} + \mathbf{p}_T \tag{12.2}$$

The gap/penetration g and normal contact force p_n are related by the following Kuhn–Tucker conditions

$$g \geq 0\,, \quad p_n \leq 0\,, \quad g p_n = 0 \tag{12.3}$$

which represent the constraints for the contact in normal direction.

Tangential contact due to friction is described in turn by a similar set of stick/slip conditions

$$\lambda \geq 0\,, \quad \phi \leq 0\,, \quad \lambda \phi = 0 \tag{12.4}$$

where ϕ is the slip criterion and λ is defined by the non-associated slip rule

$$\dot{\mathbf{u}}_T = -\lambda \frac{\mathbf{p}_T}{\|\mathbf{p}_T\|} \tag{12.5}$$

where $\dot{\mathbf{u}}_T$ is the relative tangential velocity at the contact point. For the Coulomb friction law the slip criterion takes the following form

$$\phi = \|\mathbf{p}_T\| - \mu |p_n| \tag{12.6}$$

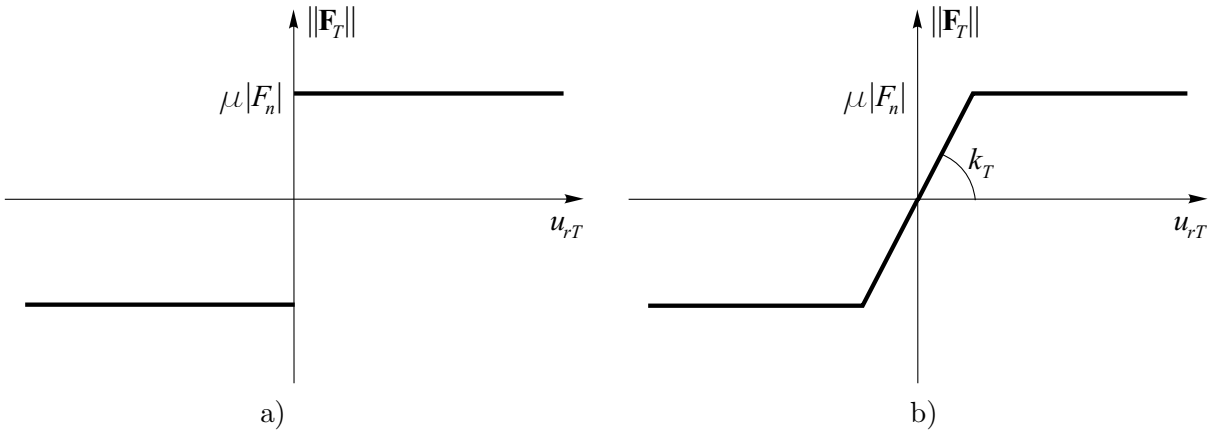

Figure 12.1: Friction force vs. relative tangential displacement a) Coulomb law, b) regularized Coulomb law

where μ is the Coulomb friction coefficient.

Our numerical implementation is based on the regularization of contact constraints using the penalty method. The normal impenetrability condition is enforced by

$$p_n = -k_n g^- \tag{12.7}$$

where k_n is the normal penalty and g^- denotes the negative part of g. The regularization of frictional constraints is carried out by introducing the tangential penalty k_T into the slip rule (12.5)

$$\dot{\mathbf{u}}_T + \lambda \frac{\mathbf{p}_T}{\|\mathbf{p}_T\|} = \frac{1}{k_T} L_v \mathbf{p}_T \tag{12.8}$$

where $L_v \mathbf{p}_T$ is the Lie derivative of $\mathbf{p}_T$. The regularization becomes exact when $k_n \to \infty$ and $k_T \to \infty$, in the explicit dynamic formulation, however, high values of penalty would limit critical time step. To avoid this the values of penalty are taken as a certain fraction of values allowed for the critical time step evaluated for the sheet elements.

The relationships between the friction force $\|\mathbf{F}_T\|$ and the relative tangential displacement u_{rT} for the classical and regularized Coulomb models (for a constant normal force F_n) are shown in Fig. 12.1a and b. The non-regularized relationship would produce non physical oscillations of the friction force in the numerical solution due to possible changes of the direction of sliding velocity. The regularization procedure prevents this non-physical behaviour.

12.2 Constitutive models of contact with cohesion

12.2.1 Elastic perfectly brittle model

The elastic perfectly brittle contact model is characterized by linear elastic behaviour when cohesive bonds are active. An instantaneous breakage of these bonds occurs when the interface strength is exceeded. When two particles are bonded the contact forces in both normal and tangential directions are calculated from the linear constitutive relationships:

$$\sigma = k_n u_n \,, \tag{12.9}$$

$$\tau = k_t \, u_t \,, \tag{12.10}$$

where σ and τ are the normal and tangential contact force, respectively, k_n and k_t are the interface stiffness in the normal and tangential directions and u_n and u_t the normal and tangential relative displacements, respectively.

Cohesive bonds are broken instantaneously when the interface strength is exceeded in the tangential direction by the tangential contact force or in the normal direction by the tensile contact force. The failure (decohesion) criterion is written (for 2D) as:

$$\sigma \leq R_n \,, \tag{12.11}$$

$$|\tau| \leq R_t \,, \tag{12.12}$$

where R_n and R_t are the interface strengths in the normal and tangential directions, respectively.

In the absence of cohesion the normal contact force can be compressive only, i.e.

$$\sigma \leq 0 \tag{12.13}$$

and the (positive) tangential contact force is given by

$$\tau = \mu |\sigma| \tag{12.14}$$

if $\sigma < 0$ or zero otherwise. The friction force is given by Eq. (12.14) expressing the Coulomb friction law, with μ being the Coulomb friction coefficient.

Contact laws for the normal and tangential directions for the elastic perfectly brittle model are shown in Figs. 12.2 and 12.3, respectively. The failure surface for the elastic perfectly brittle model defined by conditions (12.11) and (12.12) is shown in Fig. 12.4.

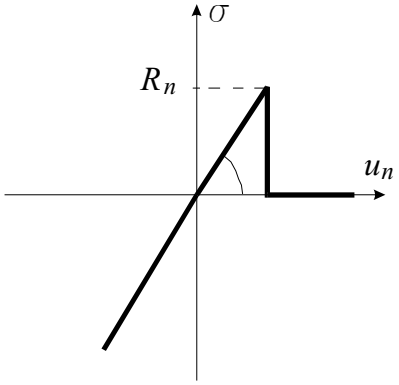

Figure 12.2: Normal contact force in the elastic perfectly brittle model

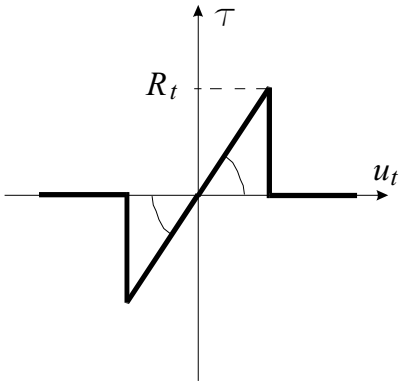

Figure 12.3: Tangential contact force in the elastic perfectly brittle model (tensile normal contact force)

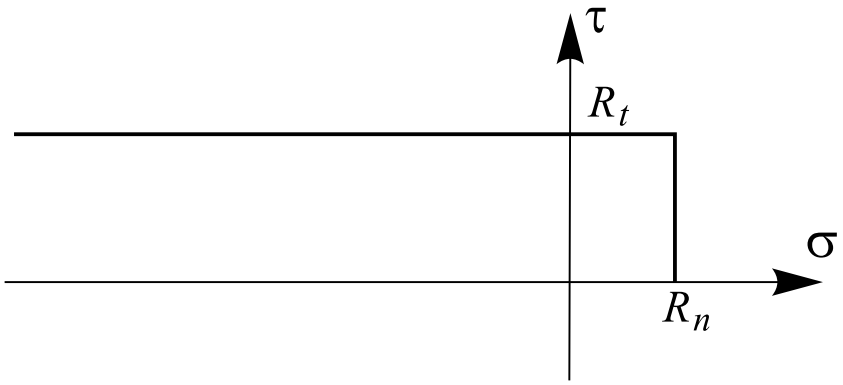

Figure 12.4: Failure surface for the elastic perfectly brittle model

12.2.2 Elasto-plastic contact model with linear softening

A contact law relates the contact force acting between two spheres to their relative displacement. The model developed is based on the analogous elasto-plastic relationships established for the normal and tangential directions:

$$\sigma = k_n(u_n - u_n^p)\,, \tag{12.15}$$

$$\tau = k_T\,(u_t - u_T^p)\,, \tag{12.16}$$

where σ and τ are the normal and tangential contact force, respectively, k_n and k_T are the interface stiffness in the normal and tangential directions, u_n and u_T are the normal and tangential relative displacements, and u_n^p and u_T^p are the plastic parts of the normal and tangential relative displacements, respectively.

For combined tension and shear the following yield criterion has been adopted

$$F(\sigma,\tau,\alpha) = \sqrt{\sigma^2 + m^2\tau^2} - \sigma_Y(\alpha) = 0\,, \tag{12.17}$$

where σ_Y is the yield stress for pure tension, m defines the ratio between interface strengths in the normal and tangential directions

$$m = \frac{\sigma_Y^0}{\tau_Y^0}\,, \tag{12.18}$$

and α is the softening parameter defined as follows

$$\alpha = \int_0^t \sqrt{(\dot{u}_n^p)^2 + m^2(\dot{u}_T^p)^2}\,\mathrm{d}t\,. \tag{12.19}$$

Yielding under the combined compression and shear is described by the Coulomb–Mohr criterion written as

$$F(\sigma,\tau,\alpha) = |\tau| + \mu|\sigma| - \tau_Y(\alpha) = 0\,, \tag{12.20}$$

where μ is the Coulomb friction coefficient and $\tau_Y(\alpha)$ defines the interface cohesion.

The complete yield surface defined by Eqs. (12.17) and (12.20) is shown in Fig. 12.5.

Elasto-plastic force-displacement relationships for normal and tangential directions are shown in Figs. 12.6 and 12.7. The elasto-plastic contact laws with linear softening

$$\sigma_Y = \sigma_Y^0 - H_n u_n^p = \sigma_Y^0 - H_n\alpha\,, \tag{12.21}$$

$$\tau_Y = \tau_Y^0 - H_T u_T^p = \tau_Y^0 - \frac{H_T}{m}\alpha\,, \tag{12.22}$$

are assumed for the shear and normal tensile contact forces, H_n and H_T being the softening moduli for the tensile and shear yield stresses, respectively.

Flow rule

The plastic strain increments of relative displacements are calculated from the following flow rules:

- associative flow rule for the combined tension and shear

$$\dot{u}_n^p = \gamma \frac{\partial F}{\partial \sigma}\,, \quad \dot{u}_T^p = \gamma \frac{\partial F}{\partial \tau}\,, \tag{12.23}$$

  where F is given by Eq. (12.17)

- non-associative flow rule for the combined compression and shear

$$\dot{u}_n^p = \gamma \frac{\partial G}{\partial \sigma}\,, \quad \dot{u}_T^p = \gamma \frac{\partial G}{\partial \tau}\,, \tag{12.24}$$

  which with the plastic flow potential

$$G = |\tau|\,. \tag{12.25}$$

  gives

$$\dot{u}_n^p = 0\,, \quad \dot{u}_T^p = \gamma\,\mathrm{sign}(\tau)\,. \tag{12.26}$$

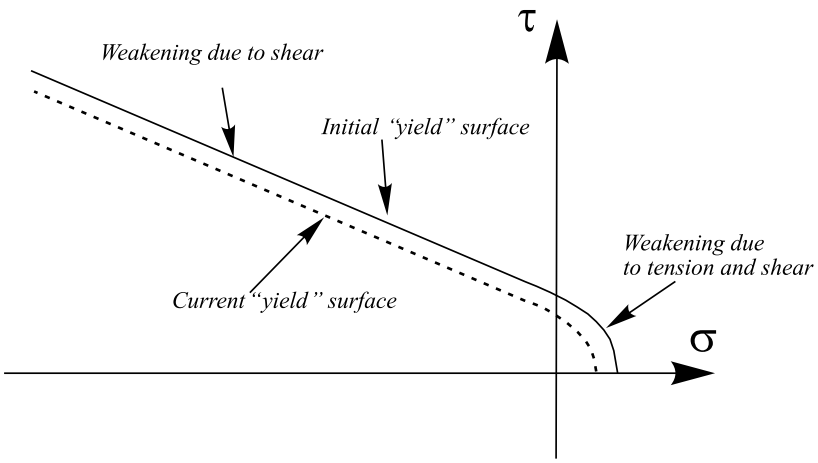

Figure 12.5: Yield surface for elasto-plastic model

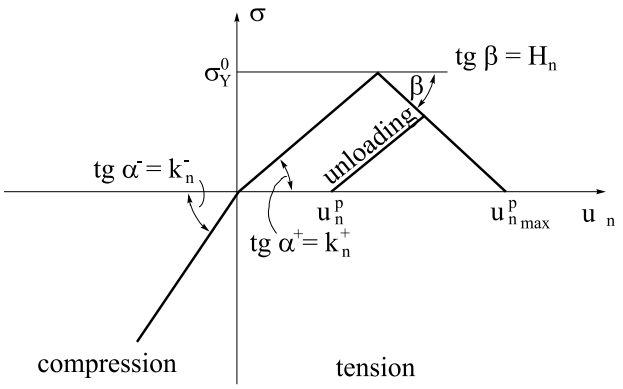

Figure 12.6: Elasto-plastic contact law with softening for the normal direction

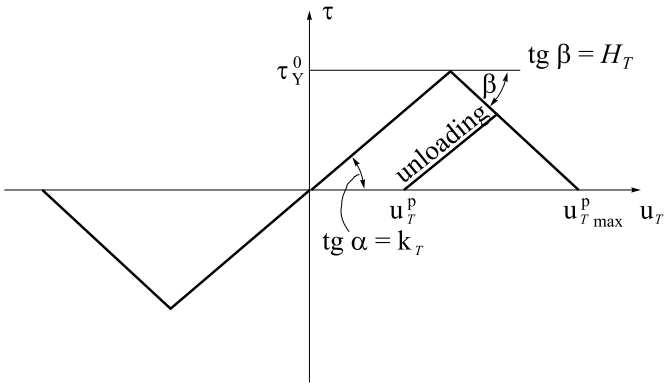

Figure 12.7: Elasto-plastic contact law with softening for the tangential direction

12.2.3 Contact model with elastic damage

The elastic perfectly brittle model can be easily extended to account for elastic damage by assuming a softening behaviour defined by a softening modulus H introduced into the force-displacement relationship (Fig. 12.8).

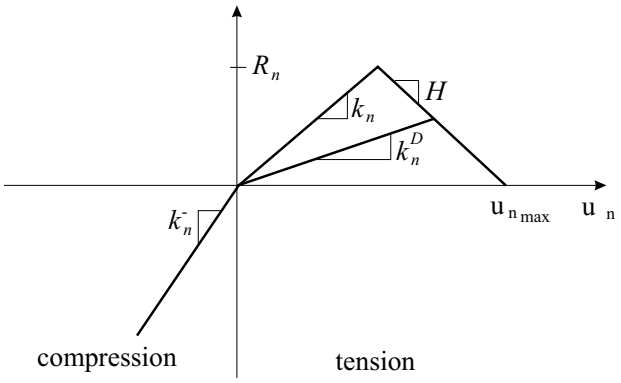

Figure 12.8: Normal contact force in the contact model with elastic damage

The constitutive relationship for 1D elastic damage is given by:

$$\sigma = k_n^D \, u_n = (1 - \omega) k_n u_n \tag{12.27}$$

where k_n^D is the elastic damaged secant modulus and ω the scalar damage variable.

The scalar damage variable ω is a measure of material damage. For the undamaged state $\omega = 0$ and for a damaged state $0 < \omega \leq 1$. The scalar damage variable ω can be written in the following form:

$$\omega = \frac{\psi(u_n) - 1}{\psi(u_n)} \tag{12.28}$$

where $\psi(u_n)$ is a function of total relative displacement. For linear strain softening $\psi(u_n)$ is defined by

$$\psi(u_n) = \begin{cases} 1 & \text{for} \quad u_n \leq \dfrac{R_n}{k_n} \\ \dfrac{k_n^2 u_n}{H R_n + k_n R_n - H k_n u_n} & \text{for} \quad \dfrac{R_n}{k_n} \leq u_n \leq \dfrac{R_n}{k_n} + \dfrac{R_n}{H} \\ \infty & \text{for} \quad u_n \geq \dfrac{R_n}{k_n} + \dfrac{R_n}{H} \end{cases} \tag{12.29}$$

where R_n is the initial tensile strength and H is the softening modulus (taken as positive).

A similar contact force–displacement law with damage (Fig. 12.9) can be introduced for the tangential direction. Then the bond decohesion can occur either due to tension

or shear. Although the interactions in the normal and tangential directions are decoupled, the damage of the contact interface due to action in one direction, results in the complete breakage of the cohesive bonds in the other direction as well.

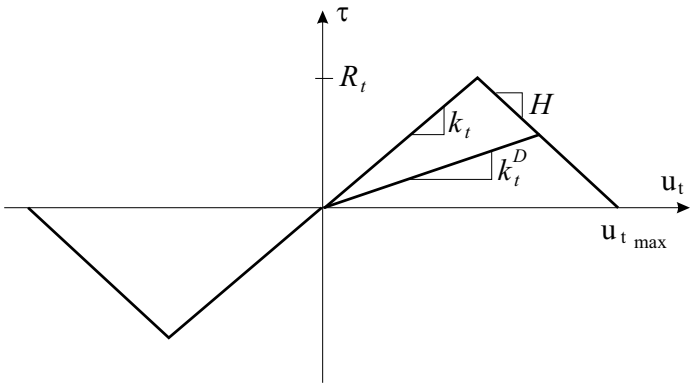

Figure 12.9: Tangential contact force in the contact model with elastic damage

An optional failure criterion has been implemented with a failure criterion based on the tensile contact force only. This criterion models better fracture of brittle materials, as the macroscopic failure is due to brittle rupture of atomic bonds in tension. This microscopic mechanism explains the macroscopic strain softening behaviour both under compression and tension states.

After the contact bonds are broken due to damage ($\omega = 0$) standard frictional contact can occur between the spherical elements.

12.3 Mixed-mode damage model of decohesion

12.3.1 Single mode decohesion

We will rewrite the elastic damage interface model presented above following the formulation presented in [53]. For pure Mode I and pure Mode II or Mode III loading the bi-linear softening constitutive behaviour represented in Fig. 12.10 is used. A high initial stiffness (penalty stiffness, K) is used to hold the two bonded surfaces together in the linear elastic range. For pure Mode I, II or III loading, after the interfacial normal or shear tractions attain their respective interlaminar tensile or shear strengths (point 2 in Figure 2), the stiffnesses are gradually reduced to zero. The onset displacements are obtained as: $\delta_3^o = N/K$, $\delta_2^o = S/K$ and $\delta_1^o = T/K$, where N is the interface tensile strength, and S and T are the interlaminar shear strengths. The area under the traction-relative displacement curves is the respective (Mode I, II or III) fracture toughness (G_{IC}, G_{IIC} and G_{IIIC} respectively) and defines the final relative displacements, δ_3^f, δ_2^f and δ_1^f, corresponding to complete decohesion:

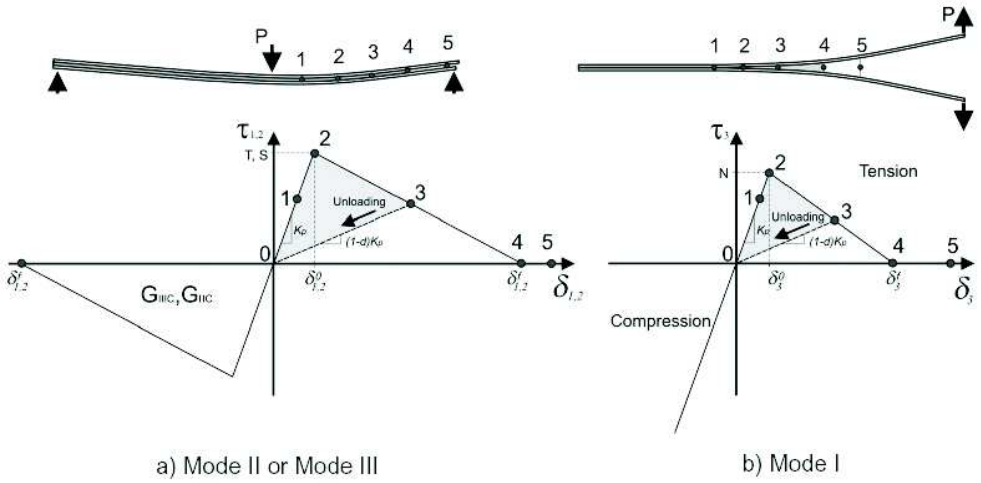

Figure 12.10: Interface constitutive relationships for pure modes, from [53]

$$\int_0^{\delta_3^f} \tau_3 \, \mathrm{d}\delta_3 = G_{IC} \tag{12.30}$$

$$\int_0^{\delta_2^f} \tau_2 \, \mathrm{d}\delta_2 = G_{IIC} \tag{12.31}$$

$$\int_0^{\delta_1^f} \tau_1 \, \mathrm{d}\delta_1 = G_{IIIC} \tag{12.32}$$

The final displacements are obtained as

$$\delta_3^f = \frac{2G_{IC}}{N}\,, \qquad \delta_2^f = \frac{2G_{IIC}}{S}\,, \qquad \delta_1^f = \frac{2G_{IIIC}}{T} \tag{12.33}$$

The loading conditions are formulated in terms of a state variable defined as the maximum relative displacement $\delta^{\max}$:

$$\delta_i^{\max} = \max\left\{\delta_i^{\max}, |\delta_i|\right\}, \quad i = 1, 2\,, \quad \text{for Mode II or III} \tag{12.34}$$

$$\delta_3^{\max} = \max\left\{\delta_3^{\max}, \delta_3\right\}, \quad \text{with } \delta_3^{\max} \geq 0\,, \quad \text{for Mode II or III} \tag{12.35}$$

A loading function F defined as

$$F(|\delta_i| - \delta_i^{\max}) = \frac{\langle |\delta_i| - \delta_i^{\max} \rangle}{|\delta_i| - \delta_i^{\max}}\,, \quad i = 1, 2 \tag{12.36}$$

for Mode II or III and

$$F(\delta_3 - \delta_3^{\max}) = \frac{\langle \delta_3 - \delta_3^{\max} \rangle}{\delta_3 - \delta_3^{\max}}\,, \quad \text{with } \delta_3^{\max} \geq 0 \tag{12.37}$$

for Mode I is introduced. The operator $\langle x \rangle$ is defined by

$$\langle x \rangle = \begin{cases} 0 \Leftarrow x \leq 0 \\ x \Leftarrow x > 0 \end{cases} \tag{12.38}$$

The irreversible, bi-linear, softening behaviour is defined as

$$\tau_i = \begin{cases} K\delta_i & \Leftarrow \delta_i^{\max} \leq \delta_i^0 \\ (1-d_i)K\delta_i & \Leftarrow \delta_i^0 < \delta_i^{\max} < \delta_i^f \\ 0 & \Leftarrow \delta_i^{\max} \geq \delta_i^f \end{cases} \tag{12.39}$$

$$d_i = \frac{\delta_i^f(\delta_i^{\max} - \delta_i^0)}{\delta_i^{\max}(\delta_i^f - \delta_i^0)}\,, i = 1,2,3; d_i \in [0,1] \tag{12.40}$$

Non-penetration condition is imposed by the following condition:

$$\tau_3 = K\delta_3 \Leftarrow \delta_3 \leq 0 \tag{12.41}$$

The properties required to define the interfacial behaviour are the penalty stiffness, K, the corresponding fracture toughness, G_{IC}, G_{IIC} and G_{IIIC}, and the corresponding interface normal tensile or shear strengths, N, S or T, respectively.

12.3.2 Mixed mode decohesion

Under mixed-mode loading damage onset and the corresponding softening behavior may occur before any of the traction components involved reach their respective allowables. A mixed-mode criterion accounting for the effect of the interaction of the traction components in the onset of delamination is proposed in [53]. It is assumed that the initiation of the softening process can be predicted using the quadratic failure criterion, considering that compressive normal tractions do not affect delamination onset

$$\left(\frac{\langle \tau_3 \rangle}{N}\right)^2 + \left(\frac{\tau_2}{S}\right)^2 + \left(\frac{\tau_1}{T}\right)^2 \tag{12.42}$$

The total mixed mode relative displacement δ_m is defined as

$$\delta_m = \sqrt{\delta_1^2 + \delta_2^2 + \langle \tau_3 \rangle^2} = \sqrt{\delta_{\text{shear}}^2 + \langle \tau_3 \rangle^2} \tag{12.43}$$

where δ_{shear} represents the norm of the vector defining the tangential relative displacements of the element.

Using the same penalty stiffness in Modes I, II and III, the traction before softening is:

$$\tau_i = K\delta_i\,, \quad i = 1,2,3 \tag{12.44}$$

Assuming $S = T$ the single mode relative displacements at softening onset are:

$$\delta_3^0 = \frac{N}{K} \tag{12.45}$$

$$\delta_1^0 = \delta_2^0 = \delta_{\text{shear}}^0 = \frac{S}{K} \tag{12.46}$$

For an opening displacement $\delta_3 > 0$ the mode mixity β is defined as

$$\beta = \frac{\delta_{\text{shear}}}{\delta_3} \tag{12.47}$$

The mixed mode relative displacement corresponding to the onset of softening, δ_m^0, is defined by substituting and solving for δ_m, which gives

$$\delta_m^0 = \begin{cases} \delta_3^0 \delta_1^0 \sqrt{\dfrac{1+\beta^2}{(\delta_1^0)^2 + (\beta \delta_3^0)^2}} & \Leftarrow \delta_3 > 0 \\ \delta_{\text{shear}}^0 & \Leftarrow \delta_3 \leq 0 \end{cases} \tag{12.48}$$

The most widely used criterion to predict delamination propagation under mixed-mode loading, the power law criterion, is established in terms of an interaction between the energy release rates [54]:

$$\left(\frac{G_I}{G_{IC}}\right)^{\alpha} + \left(\frac{G_{II}}{G_{IIC}}\right)^{\alpha} \tag{12.49}$$

In order to accurately account for the variation of fracture toughness as a function of mode ratio in epoxy composites, the mixed-mode criterion proposed by Benzeggagh and Kenane [55] is used here (B–K criterion). This criterion is expressed as a function of the Mode I and Mode II fracture toughness and a parameter η being a function of different mode ratios:

$$G_{IC} + (G_{IIC} - G_{IC}) \left(\frac{G_{II}}{G_T}\right)^{\eta} = G_C \,, \tag{12.50}$$

with $G_T = G_I + G_{II}$. If Mode III loading occurs the criterion is:

$$G_{IC} + (G_{IIC} - G_{IC}) \left(\frac{G_{\text{shear}}}{G_T}\right)^{\eta} = G_C \,, \tag{12.51}$$

with $G_T = G_I + G_{\text{shear}}$.

The energy release rates corresponding to total decohesion are obtained from:

$$G_I = \int_0^{\delta_{3f}^m} \tau_3 \, \mathrm{d}\delta_3 \tag{12.52}$$

$$G_{II} = \int_0^{\delta_{2f}^m} \tau_2 \, \mathrm{d}\delta_2 \tag{12.53}$$

$$G_{III} = \int_0^{\delta_{1f}^m} \tau_1 \, \mathrm{d}\delta_1 \tag{12.54}$$

Using (12.39), (12.43) and (12.47) in equations (12.52)–(12.54) and substituting in (12.50) or in (12.47) the criterion for total decohesion can be established in terms of δ_m and η. Solving the equation for δ_m, the mixed-mode displacements corresponding to total decohesion, δ_m^{f}, are obtained for the B-K criterion as:

$$\delta_m^f = \begin{cases} \dfrac{2}{K\delta_m^0}\left[G_{IC} + (G_{IIC} - G_{IC})\left(\dfrac{\beta^2}{1+\beta^2}\right)^{\eta}\right] & \Leftarrow \delta_3 > 0 \\ \sqrt{(\delta_1^f)^2 + (\delta_2^f)^2} & \Leftarrow \delta_3 \leq 0 \end{cases} \tag{12.55}$$

and for the power law criterion as:

$$\delta_m^f = \begin{cases} \dfrac{2(1+\beta^2)}{K\delta_m^0}\left[\left(\dfrac{1}{G_{IC}}\right)^{\alpha} + \left(\dfrac{\beta^2}{G_{IIC}}\right)^{\alpha}\right]^{-1/\alpha} & \Leftarrow \delta_3 > 0 \\ \sqrt{(\delta_1^f)^2 + (\delta_2^f)^2} & \Leftarrow \delta_3 \leq 0 \end{cases} \tag{12.56}$$

The constitutive equation for mixed-mode loading is defined by the penalty parameter K, the damage evolution function d, the mixed-mode relative displacements corresponding to damage initiation and total decohesion, δ_m^o and δ_m^f, respectively, as:

$$\tau_s = D_{sr}\delta_r \tag{12.57}$$

$$D_{sr} = \begin{cases} \bar{\delta}_{sr} K & \Leftarrow \delta_m^{\max} \leq \delta_m^0 \\ \bar{\delta}_{sr}\left[(1-d)K + Kd\bar{\delta}_{s3}\dfrac{\langle -\delta_3 \rangle}{-\delta_3}\right] & \Leftarrow \delta_m^0 < \delta_m^{\max} < \delta_m^f \\ \bar{\delta}_{s3}\bar{\delta}_{3r}\dfrac{\langle -\delta_3 \rangle}{-\delta_3} & \Leftarrow \delta_i^{\max} \geq \delta_i^f \end{cases} \tag{12.58}$$

In order to define the loading and unloading conditions the state variable maximum mixed-mode relative displacement, $\delta_m^{\max}$, and the loading function, F, are defined as:

$$\delta_m^{\max} = \max\{\delta_m^{\max}, \delta_m\} \tag{12.59}$$

$$F(\delta_m - \delta_m^{\max}) = \frac{\langle \delta_m - \delta_m^{\max} \rangle}{\delta_m - \delta_m^{\max}} \tag{12.60}$$

The mixed-mode softening law can be illustrated in a single three-dimensional map by representing Mode I on the $Y - Z$ plane, and Shear Mode in the $X - Z$ plane, as shown in Fig. 12.11.

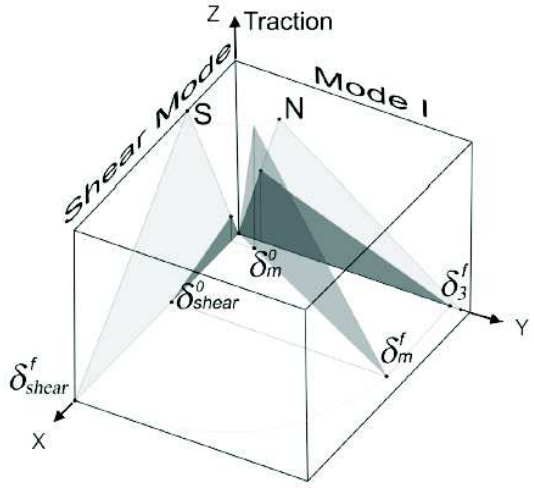

Figure 12.11: Mixed-mode softening law, from [53]

Bibliography

[1] E. Riande, R. Diaz-Calleja, M.G. Prolongo R.M. Masegosa, and C. Salomon. *Polymer Viscoelasticity. Stress and Strain in Practice*. Marcel Dekker, Inc., New York, Basel, 2000.

[2] L.E. Nielsen and R.F. Landel. *Mechanical Properties of Polymers and Composites*. Marcel Dekker, Inc., New York, Basel, 1994. Second Edition, revised and expanded.

[3] H.-G. Elias. *An Introduction to Polymer Science*. VCH, Weinheim, New York, Basel, Cambridge, Tokyo, 1997.

[4] T.A. Osswald and G. Menges. *Materials Science of Polymers for Engineers*. Hanser Publishers, Munich, Vienna, New York, 1995.

[5] A.W. Birley, B. Haworth, and J. Batchelor. *Physics of Plastics. Processing, Properties and Materials Engineering*. Hanser Publishers, Munich, Vienna, New York, Barcelona, 1992.

[6] T.A. Tervoort. *Constitutive modelling of polymer glasses: finite, nonlinear viscoelastic behaviour of polycarbonate*. PhD thesis, Technische Universiteit Eindhoven, 1996.

[7] I.M. Ward and D.W. Hadley. *Mechanical Properties of Solid Polymers*. Wiley, 1993.

[8] R. Rastogi. *Aspects of plastic deformation of PET–steel laminates*. PhD thesis, Technische Universiteit Eindhoven, 2003.

[9] D.W. Van Krevelen. *Properties of Polymers*. Elsevier, 1990.

[10] L.H. Palys and P.J. Phillips. Microkinetics of crystallization in polyethylene terphtalate. *J.Polymer Science: Polymer Physics*, 18:829–852, 1980.

[11] P.H.M. Timmermans. *Evaluation of a Constitutive Model for Solid Polymeric*. PhD thesis, Technische Universiteit Eindhoven, 1997.

[12] M.A.H. van der Aa. *Wall Ironing of Polymer Coated Sheet Metal*. PhD thesis, Technische Universiteit Eindhoven, 1999.

[13] E.T.K. Klompen. Deformation behaviour of glassy polymers; consequences of thermorheological complex behaviour. Technical report, Eindhoven University of Technology, Eindhoven, 1996.

[14] J. Mackerle. Finite-element analysis and simulation of polymers: a bibliography (1976–1996). *Modelling Simul. Mater. Sci. Eng.*, 5:615–650, 1997.

[15] J. Mackerle. Finite-element analysis and simulation of polymers – an addendum: a bibliography (1996–2002). *Modelling Simul. Mater. Sci. Eng.*, 11:195–231, 2003.

[16] P. Haupt. *Continuum Mechanics and Theory of Materials*. Springer, 2000.

[17] A. Masud. A multiplicative finite strain finite element framework for the modeling of semicrystalline polymers and polycarbonates. *Int. J. Numer. Meth. Engng.*, 47:1887–1908, 2000.

[18] A. Masud and A. Chudnovsky. A constitutive model of cold drawing in polycarbonates. *Int. J. Plasticity*, 15:1139–1157, 1999.

[19] A. Tobolsky and H. Eyring. Mechanical properties of polymeric materials. *J.Chem. Physics*, 11:125, 1943.

[20] R.N. Haward and G. Thackray. The use of mathematical model to describe isothermal stress–strain curves in glassy thermoplastics. *Proc. Roy. Soc. A*, 302:453–472, 1968.

[21] M.C. Boyce, D.M. Parks, and A.S. Argon. Large inelastic deformation of glassy polymers. Part I: Rate dependent constitutive model. *Mechanics of Materials*, 7:15–33, 1988.

[22] P.D. Wu and E. van der Giessen. On improved network models for rubber elasticity and their application to orientation hardening in glassy polymers. *J. Mech. Phys. Solids*, 41:427, 1993.

[23] H. Eyring. Viscosity, plasticity and diffusion as examples of absolute reaction rates. *J.Chem. Physics*, 4:283, 1936.

[24] A.I. Leonov. Nonequilibrium thermodynamics and rheology of viscoelastic polymer media. *Rheol. Acta*, 15:85–98, 1976.

[25] F.P.T. Baaijens. Calculation of residual stresses in injection-molded products. *Rheol. Acta*, 30:284–299, 1976.

[26] C. Bauwens-Crowet, J.C. Bauwens, and G. Homes. Tensile yield-stress behavior of glassy polymers. *J. Polym. Sci. A2*, 7:735, 1969.

[27] G.P. Marshall, L.H. Coutts, and J.G. Williams. xxxxx. *J. Mater. Sci.*, 9:1409, 1974.

[28] R.P. Kambour. xxxxx. *J. Polym. Sci. A2*, 4:349, 1966.

[29] P. Perzyna. The constitutive equations for rate sensitive plastic materials. *Quart. Appl. Math.*, 20:321–332, 1963.

[30] E.W. Hart. Constitutive relations for the nonelastic deformation of metals. *Trans. ASME J. Engng. Mat. Technol.*, 98:193–202, 1976.

[31] E. Krempl. Models of viscoplasticity. some comments on equilibrium (back) stress and drag stress. *Acta Mech.*, 69:25–42, 1987.

[32] E. Krempl, J.J. McMahon, and D. Yao. Viscoplasticity based on overstress with a differential with a differential growth law for the equilibrium stress. *Mech. Mater.*, 5:35–48, 1986.

[33] E. Krempl. Some general properties of solid polymer inelastic deformation behaviour and their application to a class of clock models. *J. Rheol.*, 42:713–725, 1998.

[34] K. Ho and E. Krempl. Extension of the viscoplasticity theory based on overstress (vbo) to capture non-standard rate dependence in solids. *Int. J. Plasticity*, 18:851–872, 2002.

[35] J.C. Simo. A framework for finite strain elastoplasticity based on maximum plastic dissipation and the multiplicative decomposition: Part I. Continuum formulation. *Comput. Meth. Appl. Mech. Eng.*, 66, 1988.

[36] M.C. Boyce, G.G. Weber, and D.M. Parks. On the kinematics of finite strain plasticity. *J. Mech. Phys. Solids*, 37:647–665, 1989.

[37] E.M. Arruda and M.C. Boyce. Evolution of plastic anisotropy in amorphous polymers during finite straining. *plast*, 9:697–720, 1993.

[38] M.C. Boyce, A.S. Argon, and D.M. Parks. Mechanical properties of compliant particles effective in toughening glassy polymers. *Polymer*, 28:1680–1694, 1987.

[39] J.S. Bergström and M.C. Boyce. Constitutive modelling of the large strain time-dependent behavior of elastomers. *J. Mech. Phys. Solids*, 46:931–954, 1998.

[40] T.A. Tervoort, R.J.M. Smit, W.A.M. Brekelmans, and L.E. Govaert. A constitutive equation for the elasto-viscoplastic deformation of glassy polymers. *Mechanics of Time-Dependent Mataerials*, 1:269–291, 1998.

[41] A.S. Argon. A theory of the low-temperature plastic deformation of glassy polymers. *Phil. Mag.*, 28:839–865, 1973.

[42] O.A. Hasan, M.C. Boyce, X.S. Li, and S. Berko. An investigation of the yield and postyield behavior and corresponding structure poly-methyl methacrylate. *J. Polymer Sci.: Part B: Polymer Phys.*, 31:185–197, 1993.

[43] M. Luege. *Resolucion numerica del problema de conformado de metales mediante la tecnica de hydroforming*. PhD thesis, Universidad de Tucuman, San Miguel de Tucuman, 2004.

[44] J.C. Simo. Algorithms for static and dynamic multiplicative plasticity that preserve the classical return mapping schemes of the infinitesimal theories. *Comput. Meth. Appl. Mech. Eng.*, 99:61–112, 1992.

[45] S. Reese and S. Govindjee. A theory of finite viscoelasticity and numerical aspects. *Int. J. Solids and Structures*, 35:3455–3482, 1998.

[46] K. Kendall. Adhesion: molecules and mechanics. *Science*, 264:1720–1725, 1994.

[47] D. Maugis. Adherence of solids. In J.M. Georges, editor, *Microscopic Aspects of Adhesion and Lubrication*, pages 221–252. Elsevier, Amsterdam, 1982.

[48] D. Maugis and M. Barquins. Fracture mechanics and adherence of viscoplastic solids. In H.-L. Lee, editor, *Adhesion and Adsorption of Polymers, Part A*, pages 203–277. Plenum Publishing Corporation, New York, 1980.

[49] M. Frémond. Adhérence des Solides. *J. Méc. Théorique Appl.*, 6:383–407, 1987.

[50] M. Frémond. Contact with Adhesion. In J.J. Moreau and P.D. Panagiotopoulos, editors, *Nonsmooth Mechanics and Applications*, pages 177–221. Springer-Verlag, Wien, 1988.

[51] M. Fremond. Contact Unilatéral Avec Adhérence: une Theorie du Premier Gradient. In G. Del Piero and F. Maceri, editors, *Unilateral Problems in Structural Analysis*, pages 117–137. Springer-Verlag, Wien–New York, 1987.

[52] N. Point. Unilateral contact with adherence. *Math. Meth. Appl. Sci.*, 10:367–381, 1988.

[53] P.P. Camanho and C.G. Davila. Mixed-mode decohesion finite elements for the simulation of delamination in composite materials. Technical report, NASA/TM-2002-211737, National Aeronautics and Space Administration, Langley Research Center, 2002.

[54] E.M. Wu and R.C. Reuter. Crack extension in fiberglass reinforced plastics. Technical report, T. & AM Report No. 275, University of Illinois, 1965.

[55] M.L. Benzeggagh and M. Kenane. Measurement of mixed-mode delamination fracture toughness of unidirectional glass/epoxy composites with mixed-mode bending apparatus. *Composites Science and Technology*, 56:439–449, 1996.